Effects of Geometry on the Wet Thermal Oxidation of Aluminum Arsenide

Thesis by

Alicia Cristina Alonzo

In Partial Fulfillment of the Requirements
for the Degree of
Doctor of Philosophy

California Institute of Technology
Pasadena, California

1999
(Submitted May 4, 1999)

In memory of my grandfather
George Eaton Simpson,
a gentleman and a scholar

List of Publications

Work related to this thesis has been or will be presented in the following papers:

Effect of cylindrical geometry on the wet thermal oxidation of AlAs, A.C. Alonzo, X.-C. Cheng, and T.C. McGill, Journal of Applied Physics **84**, pp. 6901-6905, 1998.

Strain in wet thermally oxidized square and circular mesas, A.C. Alonzo, X.-C. Cheng, and T.C. McGill, in preparation.

Work not included in this thesis is presented in the following paper:

Tunneling Spectroscopy of Resonant Interband Tunneling Structures, A.C. Alonzo, D.A. Collins, and T.C. McGill, Solid State Communications **101**, pp. 607-610, 1997.

Acknowledgements

I would like to begin by expressing gratitude to my advisor, Professor Tom McGill. Tom has been thanked numerous times for providing students with the equipment and environment to conduct their research. Although these things are important, I think Tom's group is special because of his amazing philosophy about his role as an advisor. Although his group has produced many important research results over the years, Tom seems to be most proud of the accomplishments of his students once they have graduated. McGillville is a great place to be a student in large part because of Tom's belief that his job is to train students. Tom treats each student as an individual and tailors his interactions to the personality and abilities of each of us. This enables him to be an effective advisor for a wide range of students. Along with recognizing our differences, Tom realizes that we are not all going to pursue the same path once we leave Caltech. Tom treated my non-conventional career aspirations with respect and support, and for that I am deeply grateful. I only hope that I will have the grace to treat my own students as well.

A great tribute to Tom's success as an advisor is the willingness of senior students to assist more junior students – even after they have left Caltech, Tom's former students return to help his current students. I have benefited greatly from interactions with many of Tom's students and other members of his group. In particular, I would like to thank Doug Collins and Harold Levy for helping me with my first project as a graduate student. I appreciate their willingness to teach me the basics of life in McGillville. The most valuable lesson I learned from them is the importance of thinking for myself – I believe this is the purpose of a Ph.D. As a postdoc, David Ting was a great presence in Tom's group for much of my tenure as a graduate student. Many of us were the beneficiaries of David's wisdom and support. Most of all, I would like to thank Erik Daniel. He taught me, by his great example, what it means to be a senior student in Tom's group and was an invaluable guide in acquainting me with

much of the equipment in Tom's somewhat impenetrable labs. Finally, I would like to express my appreciation to one of the newer students in Tom's group. Cory Hill knows more about computers – and how to fix them – than anyone I have ever met. I continue to be amazed by his ability to fix any problem I manage to create with the computers and his cheerful willingness to do so.

The Office of Naval Research provided financial support for the work described in this thesis, both through an ONR Graduate Fellowship and through ONR programs managed by Larry Cooper. Xiao-Chang Cheng grew the MBE samples used in the studies described in this thesis. The model presented in Chapter 4 benefited from discussions with Tom Kuech and Don Cohen. Frank Hardcastle at Namar Scientific, Inc., performed the micro-Raman spectroscopy measurements discussed in Chapter 6. I would also like to acknowledge the members of my thesis defense committee – Professors Amnon Yariv, Don Cohen, Harry Atwater, and Axel Scherer. Several of their questions and comments are reflected in this thesis.

On a personal note, I would like to recognize Rebecca Grimm, my high school science teacher, and Professor Michael Kelly, my freshman advisor at Cornell. It is not clear that I would have pursued my interest in science were it not for their encouragement. Finally, I would like to thank John O'Brien for his important role in my life.

Abstract

In recent years, the wet thermal oxidation of high aluminum-content III-V semiconductors has provided significant device improvements, most notably in vertical cavity surface emitting lasers (VCSELs). Although circles and squares are the most efficient geometries for VCSELs, most studies of the oxidation process to date have been conducted exclusively with stripes, rather than these two-dimensional mesa structures. The studies presented in this thesis examine the effect of geometry on the wet thermal oxidation process, focusing primarily on those mesa geometries with direct applicability to VCSELs. However, many of the results can be applied to more exotic mesa shapes as well.

A model is presented for the time-dependence of oxide formation in two-dimensional mesa structures. This work represents the first attempt to model the oxidation of square mesas. Although other researchers have recently proposed models for the oxidation of circular mesas, these models do not adequately account for the effect of geometry on the oxidation process. As compared to the one-dimensional oxidation of stripes, the oxidation of circular and square mesas exhibits an increased oxidation rate as the process proceeds. This is a direct effect of the geometry of the mesas. Extensive data is presented in support of our model, and a comparison is made to other models for the oxidation of circular mesas.

The two-dimensional mesa geometry, coupled with anisotropies in the oxidation process itself, is shown to produce variations in the strain induced in the overlying GaAs layer by the oxidation process. Using micro-Raman spectroscopy, this strain has been spatially mapped and shown to correspond to color variations observed in the mesas with an optical microscope. A crystallographic-dependence for the oxidation is documented and used to explain the spatial variations in the strain as well as the shape of apertures formed in circular and square mesas by the wet thermal oxidation process.

Contents

List of Figures

List of Tables

Chapter 1 Introduction

1.1 Introduction

Since the 1970's, researchers have been interested in finding an oxide for the III-V material system with properties similar to those of SiO_2. One of the main reasons for the commercial success of the silicon material system is the high quality of its native oxide [1]. However, III-V materials have two important advantages over silicon. They are better suited for high-speed operation [2, 3] due to higher electron mobilites and saturation velocities [4]. In addition, silicon, as a bulk semiconductor, is not a direct bandgap material; therefore, it is not suitable for light-emitting devices such as those readily formed in the III-V material system. Both of these properties are expected to have increased importance in the future, as the quest for faster computers continues. To achieve increased speed, silicon devices have been scaled down smaller and smaller; however, the size of silicon devices is rapidly approaching a limit past which additional scaling would be quite costly. Because they are intrinsically faster, larger III-V devices could operate at the same speed as much smaller silicon devices [2], thereby circumventing the size-limitation problem. In addition, the use of optical interconnects has been proposed as a faster alternative to electronic connections. The ability to form both electronic and optical elements on a single III-V substrate would aid the incorporation of faster optical connections. However, without a suitable oxide, the III-V material system is not in a position to compete with the well-established silicon technology, and this potential remains untapped. Despite millions of dollars of research money directed at the problem [5], attempts to create a suitable oxide for the III-V system have proved unsuccessful.

In 1990, Holonyak's group at the University of Illinois discovered a process by which high-quality oxides could be formed from high aluminum-content III-V semiconductors [6]. Dallesasse et al. observed severe degradation in samples containing high aluminum-content $Al_xGa_{1-x}As$ layers which were exposed to normal atmospheric conditions for several years [7, 8]. Attempting to speed up this degradation, similar samples were placed in a hot, humid environment. However, instead of rapidly degrading the samples, the treatment resulted in the formation of a dense, high-quality oxide [6].

It seems significant that the oxide was discovered in a group whose main research interest was semiconductor lasers. As discussed in Section 2.3.1, the wet thermal oxide does not have sufficient electrical quality for the formation of metal-oxide-semiconductor (MOS) devices. Had the oxide been discovered by researchers trying to make a III-V MOS device, interest may have quickly dissipated once its poor electrical behavior was observed. However, in accordance with the interests of Holonyak's research group, the oxide was quickly incorporated into a laser design [9]. As discussed in Section 2.2, the oxide's incorporation into lasers, particularly vertical cavity surface emitting lasers (VCSELs), has provided dramatic results.

1.2 Summary of Thesis

Despite being discovered less than a decade ago [6], the wet thermal oxide of $Al_xGa_{1-x}As$ has quickly gained technological importance due to the dramatic improvements in VCSEL performance that it has provided. However, its rapid incorporation into real devices has also impeded research to understand the more basic properties of the oxide. Because it proved to be so useful in its as-discovered form, there was relatively little work done to understand the oxide or its formation in any detail. Recently, limitations of the oxide have been noted, including its reproducibility for commercial devices and its inability to form high-quality MOS devices [10], so there has been increased interest in understanding its basic properties. A review of this work can be found in Chapter 2.

This thesis presents two studies which contribute to a basic understanding of the wet thermal oxidation process and which have an impact on devices formed with the oxide. Both of these studies are concerned with the effect of two-dimensional geometry on the oxidation process. This is important because many device applications of the oxide require two-dimensional oxidation rather than the one-dimensional oxidation of stripes which is typically studied. In order to conduct this work, an oxidation set-up was designed and built. This set-up and the experimental procedures used in this thesis are discussed in Chapter 3.

Chapters 4 and 5 present theoretical and experimental support for a model developed to explain the time-dependence of oxidation in two-dimensional mesa structures, such as circular and square mesas. Although circles and squares are the most efficient geometries for VCSELs, until recently, studies of the oxidation process were conducted exclusively with stripes. As will be shown in Chapter 5, the oxidation of stripes has a much different time-dependence than that of circular or square mesas, particularly as the oxidation proceeds. Thus, a full account of the geometry of the oxidizing structure, such as that provided by our model, is necessary for a more thorough understanding of the oxidation process in two dimensions.

In Chapter 6, we explore another consequence of the two-dimensional oxidation geometry. Drumhead patterns are observed in circular and square mesas which have been oxidized almost to completion. Using micro-Raman spectroscopy, these patterns can be shown to correspond to variations in the strain induced in the GaAs cap layer by the oxidation of an underlying AlAs layer. In addition, the crystallographic-dependence of the drumhead patterns, as well as the apertures formed in partially oxidized mesas, is correlated with a crystallographic-dependence of the oxidation process itself.

Bibliography

[1] R. Muller and T. Kamins, in *Device Electronics for Integrated Circuits*, 2nd ed. (John Wiley & Sons, New York, 1986), p. 58.

[2] S. Wang, in *Fundamentals of Semiconductor Theory and Device Physics* (Prentice Hall, Englewood Cliffs, New Jersey, 1989), p. 721.

[3] M. Shur, in *Physics of Semiconductor Devices* (Prentice Hall, Englewood Cliffs, New Jersey, 1990), p. 406.

[4] M. Shur, in *Physics of Semiconductor Devices* (Prentice Hall, Englewood Cliffs, New Jersey, 1990), p. 580.

[5] T. McGill, discussion, 1996.

[6] J. Dallesasse, N. Holonyak, Jr., A. Sugg, T. Richard, and N. El-Zein, Appl. Phys Lett. **57**, 2844 (1990).

[7] J. Dallesasse, P. Gavrilovic, N. Holonyak, Jr., R. Kaliski, D. Nam, and E. Vesely, Appl. Phys. Lett. **56**, 2436 (1990).

[8] J. Dallesasse, N. El-Zein, N. Holonyak, Jr., and K. Hsieh, J. Appl. Phys. **68**, 2235 (1990).

[9] J. Dallesasse and N. Holonyak, Jr., Appl. Phys. Lett. **58**, 394 (1991).

[10] C. Ashby, J. Sullivan, P. Newcomer, N. Missert, H. Hou, B. Hammons, M. Hafich, and A. Baca, Appl. Phys. Lett. **70**, 2443 (1997).

Chapter 2 Background and Literature Review

2.1 Introduction and Chapter Outline

This chapter is divided into two parts. Section 2.2 provides an overview of the impact of the wet thermal oxidation process on semiconductor devices. Section 2.3 summarizes the current state of knowledge about the wet thermal oxidation process and the oxide formed from $Al_xGa_{1-x}As$ using this technique.

2.2 Device Applications of the Wet Thermal Oxide of $Al_xGa_{1-x}As$

This section is intended to provide the reader with a sense of the technological importance of the wet thermal oxidation process by discussing its application to semiconductor devices. MOS devices are an obvious application for the oxide. There have been several attempts to fabricate MOSFETs using the wet thermal oxide of various III-V semiconductors [1, 2, 3]. However, Ashby et al. have shown that the oxide, in its present form, cannot form a MOS device with sufficiently low interface state density [4]. Therefore, MOS applications of the oxide will not be discussed further in this section.

The big success story of the wet thermal oxide is its incorporation into VCSELs. Section 2.2.1 describes the impact that the wet thermal oxidation process has had upon VCSEL performance. Recently, creative uses of the oxide have been proposed for novel device applications, some of which are discussed in Section 2.2.2.

2.2.1 Impact of the Wet Thermal Oxide on VCSEL Performance

The wet thermal oxide has been incorporated into VCSEL structures in two ways. The most dramatic is the use of the oxide to form an aperture, guiding current and light into a small device volume. In addition, the oxide has been incorporated in distributed Bragg reflectors (DBRs), the highly reflective mirrors on either end of a VCSEL cavity. Both of these VCSEL applications are discussed below.

Oxide Apertures in VCSELs

Lateral oxidation from the edge of a mesa can be used to produce an oxide aperture surrounding unoxidized semiconductor. Because the oxide has a significantly lower conductivity and index of refraction, as compared to unoxidized $\mathrm{Al}_x\mathrm{Ga}_{1-x}\mathrm{As}$, it provides both current and optical confinement [5]. The oxide was first used as an aperture in edge-emitting lasers [6], followed shortly by the first oxide aperture in a VCSEL structure [7].

Prior to the introduction of oxide apertures, current confinement in VCSEL structures was provided by proton implantation. However, this process damages the semiconductor crystal and does not provide significant optical confinement [8]. The small amount of index guiding present in proton-implanted structures is provided by thermal lensing, which results in nonlinear light-current characteristics and a beam profile dependent upon the operating current [9]. Compared to proton-implanted VCSELs fabricated from the same epitaxial material, VCSELs with oxide apertures have substantially lower threshold voltages and currents [10]. Specifically, an order-of-magnitude reduction in threshold current has been obtained for oxide-apertured VCSELs, as compared to proton-implanted VCSELs from the same wafer [11].

Prior to the introduction of the oxide aperture, a typical high-performing VCSEL had 21% power efficiency and a 5.1 mA threshold current [12]. Within a year, an oxide-apertured VCSEL with 50% power efficiency [8] and one with a threshold current of 8.7 μA [13] had been demonstrated. Although this ultralow threshold current has not been measured for other lasers of the same design [14], threshold currents below 100 μA have been reported for several different oxide-apertured VCSEL structures [15, 16, 17, 18]. These low threshold currents have all been realized in VCSELs with output at 980 nm; similar reductions in threshold current have made shorter wavelength VCSELs possible as well. The lowest threshold current (660 μA) and voltage (150 mV above photon energy) for visible VCSELs allowed room-temperature continuous wave (CW) operation at a record-low 640 nm, using an oxide aperture [19].

Oxide Distributed Bragg Reflectors

Distributed Bragg reflectors (DBRs) are a standard component in most VCSEL designs, forming the high reflectivity mirrors on either side of the laser cavity. These mirrors are formed with alternating layers of materials with different indices of refraction. The reflectivity of a DBR increases with the number of layer pairs and the ratio of the refractive indices of the two materials [20]. By using the wet thermal oxide of AlAs, instead of unoxidized AlAs, in a DBR with GaAs, the refractive index ratio is increased from 1.2 in the GaAs/AlAs DBR to 2.3 in the GaAs/AlAs-oxide DBR [21]. Therefore, DBRs incorporating the wet thermal oxide can achieve greater reflectivity with fewer pairs [21]. This greatly reduces the growth time required to form the epitaxial material for the laser structure [22]. In addition, the stringent growth requirements of all-semiconductor DBRs are relaxed in oxide DBRs, which have less sensitivity to thickness variations in the epitaxial layers [20, 21, 22]. Oxide DBRs have also been shown to reduce diffraction losses in VCSELs due to a decreased optical penetration length in the mirror [22].

2.2.2 Additional Uses of the Wet Thermal Oxide for Novel Device Applications

Recently, creative uses of the wet thermal oxide have been proposed and demonstrated for additional semiconductor device applications. Blum et al. have formed an embedded semiconductor lens by vertically tailoring the aluminum content of the

$Al_xGa_{1-x}As$ layers forming the lens. Since the wet thermal oxidation rate is highly dependent upon aluminum content, these layers oxidize to different extents, leaving a lens of desired shape [23]. The low refractive index of the wet thermal oxide has been used to enhance birefringence in GaAs/AlAs waveguides, with the potential for nonlinear frequency conversion [24].

In addition, two research groups have investigated the use of the wet thermal oxidation process for integrating optical components on a single substrate. Bond et al. have used the oxide to fabricate surface- and substrate-emitting VCSELs on a single wafer. As grown, all VCSELs on the wafer are symmetric, with both DBRs having equal reflectivity. Selective oxidation is used to adjust the relative reflectivies of the DBRs, thus determining the direction of light output. Using this technique, VCSELs emitting in both directions were fabricated with threshold currents of 65 - 70 μA [25]. Sjölund et al. report using the wet thermal oxide to integrate VCSELs and photodetectors. VCSELs require a higher reflectivity of the output mirror than the input mirror of a photodetector with the same active region; to achieve different reflectivities with the same epitaxial material, AlGaAs layers in the bottom DBR of the VCSEL are selectively oxidized to increase its reflectivity [26]. The same research group has used wet thermal oxidation to achieve VCSELs with a 48-nm wavelength span on a single wafer, with applications to wavelength division multiplexing systems [27].

There has even been interest in using the wet thermal oxidation process to form templates for semiconductor growth [28, 29]. Chavarkar et al. have proposed the following scheme for creating substrates with larger lattice constants than are currently available. First, an Al-containing layer is grown lattice-matched to a pre-existing substrate, followed by a compressively strained layer. Upon oxidation of the Al-containing layer, the strained layer relaxes and can be used as a template for further semiconductor growth. Using this technique, $In_{0.2}Ga_{0.8}As$, $In_{0.7}Ga_{0.3}As$, and InAsSb can be used as growth templates [28]. More impressively, Kobayashi et al. have used an intermediate wet thermal oxide layer to epitaxially grow GaN on a Si(111) substrate [29].

2.3 Summary of Current Knowledge About the Wet Thermal Oxide of $Al_xGa_{1-x}As$ and Its Formation

This section attempts to provide the reader with an overview of what is currently known about the wet thermal oxidation process and the oxide formed from $Al_xGa_{1-x}As$ using this technique. Section 2.3.1 provides a basic description of the oxidation recipe, including typical parameters for the oxidation process. The effects of these parameters and other factors influencing the rate at which the oxidation proceeds are discussed in Section 2.3.2. In Section 2.3.3, properties of the oxide formed by wet thermal oxidation are discussed. This is followed by Section 2.3.4, in which the interfaces between the oxide and surrounding semiconductor are described. Proposed reactions for the oxidation are detailed in Section 2.3.5.

2.3.1 Oxidation Recipe

The wet thermal oxidation process has been used to oxidize both surface and buried layers. Surface layers are oxidized vertically, usually after a protective cap layer has been removed since layers with reasonable oxidation rates also readily degrade in the atmosphere. Buried layers are exposed by etching mesas in the semiconductor material, either by wet or dry etching processes. In this case, oxidation proceeds laterally through the mesa, creating either fully oxidized layers or oxide apertures surrounding unoxidized material. As will be discussed in Section 2.3.2, the oxidation process is highly dependent upon aluminum content, so that high aluminum-content layers can be selectively oxidized, while low aluminum-content layers are relatively unaffected.

The set-up used in our experiments, shown in Figure 3.1, is fairly typical of those used by other researchers for the wet thermal oxidation of $Al_xGa_{1-x}As$ layers. Furnace temperatures ranging from 320 to 570°C [30] have been reported. Typical furnace temperatures are 400 - 450°C, and most researchers use three-zone furnaces for better temperature control. Water vapor is supplied to the furnace by bubbling a carrier gas, typically N_2, through heated water. Water bubbler temperatures from 50°C [31] to 95°C [32] have been reported, although the range from 85 to 95°C is most common. Carrier gas flow rates range from 0.075 liter/min [33] to 3 liter/min [34]. The line between the water bubbler and the furnace is sometimes heated to prevent condensation of water vapor in the line [30, 35]. In addition, since the lowest temperature encountered by the water vapor should control its partial pressure in the furnace, heating the line above the temperature of the water bubbler ensures that the water vapor pressure in the furnace is not influenced by fluctuations in the ambient room temperature [36].

Due to dramatic improvements in VCSEL performance offered by wet thermal oxidation, there has been increased interest in precise control of this process so that it can be used to produce commercial devices. Some researchers isolate the water bubbler from ambient room temperature fluctuations by placing it in a constant temperature bath [35]. Others use a capillary at the bottom of the furnace's quartz tube to preheat the incoming water vapor to the furnace temperature [37]. In addition to these equipment improvements, there has been some focus upon the procedures used to initiate and terminate the oxidation process. An observed delay in the onset of oxidation has been attributed to the time required for the sample [30] or the quartz sample insertion rod [38] to reach the furnace temperature. One way to control this delay is to insert the sample into a dry furnace, initiating the oxidation by redirecting the carrier gas flow through the water bubbler [4]. After oxidation, the sample is allowed to cool in the furnace under nitrogen flow [39]. In other experiments, including the ones described in this thesis, the furnace is allowed to come to equilibrium with flowing water vapor, and the sample is placed on a preheated plate before inserting it into the furnace to commence oxidation [35]. In order to minimize condensation of water vapor onto the sample, Burton and Schlesinger turn off the carrier gas temporarily just prior to loading samples onto a preheated slider [38].

2.3.2 Factors Known to Affect the Rate of Wet Thermal Oxidation

This section details the factors that are known to affect the rate at which wet thermal oxidation proceeds in one dimension. Unless otherwise noted, all results in this section were obtained with stripes. The first part of this section discusses the effects of variations in the oxidation parameters described in Section 2.3.1, including furnace and water bubbler temperatures, as well as carrier gas flow rate and composition. Control and understanding of these parameters is crucial to the commercialization of devices incorporating the wet thermal oxide. The second part of this section discusses how the rate of oxidation is affected by the semiconductor sample itself. The aluminum content, growth temperature, and thickness of the oxidizing layer are all shown to affect the oxidation rate. In addition, the effects of the surrounding layers on the oxidation rate are considered. The doping and crystallographic orientation of the sample may also affect the oxidation rate and are discussed below.

Furnace Temperature

The temperature of the furnace affects both the diffusion of reactant molecules through the already-existing oxide and the reaction of those molecules at the oxide-semiconductor interface. Each of these processes can be described by a temperature-dependent constant which directly influences the rate at which it takes place. For oxidation in one dimension, the rate at which the oxidation front is advanced by the reaction is just the reaction constant k_R:

$$\frac{dx_R}{dt} = k_R. \tag{2.1}$$

Diffusion through the existing oxide slows as more oxide is formed, so the rate at which one-dimensional diffusion advances the oxidation front decreases as the oxidation proceeds:

$$\frac{dx_D}{dt} = \frac{k_D}{2x_D}. \tag{2.2}$$

However, for a given oxide extent, the rate is directly proportional to the diffusion constant k_D. Both processes will be discussed in more detail in Chapter 4.

The temperature-dependence of both k_R and k_D can be expressed with an Arrhenius relationship:

$$k = k_0 exp\left[\frac{-E_a}{K_B T}\right], \tag{2.3}$$

where E_a is the activation energy, K_B is Boltzmann's constant, and T is the temperature (in Kelvin). Therefore, the oxidation rate in one dimension has an approximately exponential dependence on the furnace temperature. As will be shown in Chapters 4 and 5, the reaction and diffusion components are more complicated for two-dimensional oxidation. However, the constants governing these processes have the same temperature-dependence as for one-dimensional oxidation, as given in Equation 2.3.

Water Bubbler Temperature

Increasing the water bubbler temperature has also been found to increase the oxidation rate [40]. This has been attributed to the direct relationship between the temperature of the water bubbler and the partial pressure of water vapor in the furnace [35]. As discussed below, the water bubbler temperature also influences the effect that the carrier gas flow rate has upon the oxidation.

Carrier Gas Flow Rate

The influence of carrier gas flow rate must be considered in two separate regimes. For low gas flow, the oxidation rate has been found to be approximately linear with gas flow rate [35]. Above a minimum gas flow, the system is considered to be in a water vapor saturated regime [35], where the oxidation rate is independent of gas flow rate [41]. In this regime, the oxidation reaction is not limited by the supply of reactant molecules. The transition between these two regimes depends upon the temperature of the water bubbler. As the water bubbler temperature increases, the transition is reached at lower flow rates. For example, the water vapor saturated regime is reached at approximately 1.5 liter/min for a 90°C bubbler but not until about 3 liter/min for a 60°C bubbler [35].

In addition to directly affecting the oxidation rate, the carrier gas flow rate can influence other oxidation parameters. The temperature of water in the bubbler has been found to vary with carrier gas flow rate [35]. Other researchers have reported using lower carrier gas flow rates to avoid affecting the ambient furnace temperature [31]. In addition, the water level in the bubbler falls at a rate that depends on the carrier gas flow, and the amount of water vapor transferred to the furnace was found to be affected by this water level [41].

Carrier Gas

Although nitrogen is typically used as a carrier gas for wet thermal oxidation, other researchers have reported using an argon carrier gas [42], and several studies have been conducted to explore the influence of carrier gas composition on the oxidation process. Oxidation rates have been reported to vary only slightly with nitrogen, argon, or forming gas (3% H_2/N_2) as the carrier [35]. Adding 10% H_2 to N_2 also has little effect on the oxidation rate [38].

Oxygen has been reported to completely inhibit wet thermal oxidation [35]. This has been used as evidence to support the proposed crucial role of hydrogen in the oxidation process [39], as discussed in Section 2.3.5. Since hydrogen will be rapidly consumed by oxygen to form water, it will no longer be available to contribute to the oxidation process [39]. Other researchers have reported that oxidation with oxygen carrier gas is possible at higher temperatures, although the process apparently self-terminates after only about 80 nm of oxide has been formed [38]. These researchers also report that the activation energy for the wet thermal oxidation of $Al_{0.6}Ga_{0.4}As$ is reduced from 1.87 to 0.99 eV by the addition of only 0.1% O_2 to N_2 but that a similar decrease is not observed for $Al_{0.77}Ga_{0.23}As$. Using air (20% O_2 in N_2) results in poor quality samples due to nonuniform oxide growth [38].

Aluminum Content of the Oxidizing Layer

As first noted by Kish et al., higher aluminum-content $Al_xGa_{1-x}As$ oxidizes more rapidly than lower aluminum-content $Al_xGa_{1-x}As$ for all oxidation temperatures [43]. The difference in oxidation rates for varying aluminum content is quite dramatic. The oxidation rate increases by more than two orders of magnitude when the aluminum content of $Al_xGa_{1-x}As$ is changed from x = 0.84 to x = 1.0 [44], and the oxidation of $Al_{0.8}Ga_{0.2}As$ is 20 times faster than that of $Al_{0.6}Ga_{0.4}As$ [38]. The selectivity of the oxidation process between AlAs and $Al_{0.3}Ga_{0.7}As$ is reported to be at least 1000 [45]. Evans and Holonyak have proposed a relationship between the oxidation "velocity," V, and $Al_xGa_{1-x}As$ composition ($0.86 < x < 0.92$), which only slightly underestimates the increasing slope of the true V(x) curve. This expression is given as

$$V(x) = V_0 exp[\gamma(x - 0.86)], \tag{2.4}$$

where $V_0 = 0.441$ μm/h and $\gamma = 19.662$ [46].

As stated in Section 2.3.1, the selectivity of the wet thermal oxidation process allows the formation of buried oxide layers, which are crucial for the fabrication of VCSELs. However, the strong dependence of the oxidation rate on aluminum concentration also means that extremely tight composition control is necessary to obtain reliable oxidation across a wafer. This restriction could limit the use of $Al_xGa_{1-x}As$ oxide layers in the production of commercial devices. Nominally identical wafers have been found to have oxidation rates that differ by approximately 10%, and oxidation rates have been found to be consistently lower near the edge of a wafer, presumably due to a slight increase in gallium concentration [47]. For example, the oxidation rate of an $Al_{0.98}Ga_{0.02}As$ layer was found to vary by ±2% across one-quarter of a 3" wafer. This variation can be attributed to a fluctuation in the mole fraction of aluminum of only ±0.001 [35].

Aluminum appears to be the key to the wet thermal oxidation process. This has been attributed to the high oxidation potential of aluminum compared to other group III elements, such as gallium [43]. However, its importance decreases with increasing temperature [35]. Because the activation energy for the oxidation reaction increases with decreasing aluminum-composition [30, 35, 43], the difference in oxidation rates for layers with different aluminum contents is significantly decreased at higher temperatures so that even GaAs can be oxidized at a high enough temperature [48].

Growth Temperature of the Original AlGaAs Layer

Recently, there has been interest in oxidizing low-temperature-grown (LTG) AlGaAs layers [49] due to the possibility of reducing the polycrystalline nature of the resulting oxide [50] and the amount of elemental arsenic remaining in the layer after oxidation [50, 51]. These LTG layers are non-stoichiometric, containing an increased amount of As relative to standard $Al_xGa_{1-x}As$. Polycrystalline AlGaAs results from growth at 350°C, and amorphous AlGaAs is obtained from growth at 250°C [52]. Both polycrystalline and amorphous LTG layers oxidize at significantly higher rates than their crystalline counterparts [52, 53]. These results are consistent with an earlier report by Burton and Schlesinger, indicating that the oxidation rate is decreased in layers grown with a reduced AsH_4 flow [38]. As expected, the opposite trend is observed in this case, where a decreased amount of As is incorporated, as compared with the low temperature growth during which excess As is incorporated into the AlGaAs layer.

Thickness of the Oxidizing Layer

Evidence of a thickness-dependence for wet thermal oxidation rates was reported in the first paper describing the oxidation process [54]. Little attention was paid to this relationship, however, until a recent explosion of papers and theories on this topic. Oxidation rates are independent of thickness for thick oxidizing layers; however, for thin layers, oxidation rates decrease rapidly with decreasing thickness. Reports of the thickness at which this transition occurs range between 50 nm [55] and 80 nm [56]. The dramatic dependence of the oxidation rate upon the thickness of thin oxidizing layers can be illustrated with several examples. Kim et al. demonstrate that an 80-nm AlAs layer oxidizes over two times faster than a 25-nm layer and show that a

160-nm AlAs layer oxidizes over 50 times faster than a 15-nm layer [56]. A two-orders-of-magnitude reduction in the oxidation rate is reported for 10-nm AlAs layers compared to 100-nm layers [35]. At thicknesses below 15 nm, the oxidation practically stops [40, 56, 57].

The first mathematical description of the thickness-dependence was proposed by Ochiai et al [58]. Assuming that the reaction rate, W, is sensitive to the layer thickness, θ, due to strain, the following relationship was proposed:

$$W(\theta) = W_0 e^{-(\theta_0/\theta)^2} \approx W_0 \left(1 - \frac{\theta_0^2}{\theta^2}\right) \tag{2.5}$$

where θ_0 is the minimum thickness for oxidation.

Shortly thereafter, Naone et al. proposed a model for the thickness-dependence which was based upon thermodynamical considerations [55]. Experimental results were reported which show that the activation energy for the oxidation reaction increases with decreasing layer thickness and that the curvature of the oxidation front is significantly more blunt for thick layers than for thin layers. This curvature was taken as an indication that the interface exerts pressure opposing the formation of additional oxide, through the Gibbs-Thomson effect. By considering the surface energy of each interface and the geometry of the oxide layer, an expression was derived for the activation energy of the oxidation reaction in a thin layer. This can be written as

$$E_a(\theta) = E_\infty + \frac{2\left(\gamma_{ox/GaAs} - \gamma_{AlAs/GaAs}\right) V_{ox}}{\theta} = E_\infty + \frac{2\Delta\gamma_{GaAs} V_{ox}}{\theta}, \tag{2.6}$$

where θ is the thickness of the AlAs layer, E_∞ is the activation energy associated with a planar oxidation front (an infinitely thick AlAs layer), $\gamma_{ox/GaAs}$ is the surface energy of the oxide-GaAs interface, $\gamma_{AlAs/GaAs}$ is the surface energy of the AlAs-GaAs interface, and V_{ox} is the molar volume of the oxide at the interface. This model shows good agreement with experimental results.

While the surface energy model focuses on the effect of layer thickness on the reaction component of the oxidation, Yoshikawa et al. have concentrated on the diffusion component [57]. The diffusion process is modeled as CASE II diffusion, in which there is an additional term in the diffusion equation due to inner stress opposing the diffusion. Thus, the modified diffusion equation can be written as

$$\frac{\partial C}{\partial t} = \left(D \frac{\partial^2 C}{\partial^2 x} - B S_{xx} C \right), \tag{2.7}$$

where C is concentration of diffusing material, B is mobility of the diffusing material, and S_{xx} is the inner stress tensor. In the case of lateral oxidation, this stress comes from the semiconductor layers above and below the oxidizing layer. When the oxidizing layer is thin enough, the inner stress is too strong to allow diffusion to occur, and the oxidation stops.

Later, Koley et al. proposed a thickness-dependent relationship between the oxidation time, t, and the resulting oxidation extent, x, based upon the Grove and Deal model for the oxidation of silicon [59]. This model considers the effect of thickness on both the reaction and diffusion components of the oxidation. The resulting expression can be written as [40]

$$t(x) = \int_0^x dx_o \left[\frac{A \cdot \frac{2\pi}{a} \cdot cosh\left(\frac{\pi}{a} x_o\right) + \left(1 + \frac{4\pi^2}{a^2} A^2 \beta^2 \alpha\right) sinh\left(\frac{\pi}{a} x_o\right)}{B \cdot \frac{2\pi}{a}} \right], \tag{2.8}$$

where

$$a = \theta \sqrt{\eta}, \tag{2.9}$$

$$A = 2D \left(\frac{1}{h} + \frac{1}{k} \right), \tag{2.10}$$

$$B = \frac{2D \cdot \tilde{C}}{N_0}, \tag{2.11}$$

$$\beta = \frac{k}{k+h} \tag{2.12}$$

and

$$\alpha = \frac{1-\beta}{\beta}. \tag{2.13}$$

In Equation 2.9, θ is the thickness of the oxidizing layer and η relates the (x,x) and (y,y) components of the diffusion tensor: $D_x = \eta D_y = D$. In Equations 2.10 and 2.11, h is a gas phase transport coefficient and k is the oxidation reaction rate constant. In Equation 2.11, $\tilde{C}$ is equal to $\frac{\pi}{2}$ times the concentration of oxidant in the oxidizing gas near the outer surface of the mesa, and N_0 represents the concentration of oxidant in a fully oxidized layer. Equation 2.8 also shows good agreement with experimental results.

As illustrated by the preceding examples, the thickness of the oxidizing layer is thought by different researchers to affect the oxidation rate through the diffusion component, the reaction component, or both processes. However, reaction-rate-limited oxidation is still observed for thin layers [20, 35], which seems to indicate that decreased diffusion is not responsible for the observed decrease in oxidation rates for thin layers [35]. Therefore, theories such as those advanced by Naone et al. [55] and Ochiai et al. [58] seem most plausible for explaining the thickness-dependence of the oxidation rates.

The dependence of oxidation rate on the thickness of the layer may compensate for the dependence on the aluminum content such that thin layers of AlAs may oxidize slower than thick layers of $Al_xGa_{1-x}As$ [35]. As discussed earlier, tight control of aluminum content is required for uniform oxidation rates; the requirements for thickness control are less stringent [20]. Therefore, thickness variations, instead of $Al_xGa_{1-x}As$ composition, may provide a more reproducible method for controlling oxidation rates. For example, a single processing step can be used to completely oxidize AlAs in a VCSEL mirror and partially oxidize an AlAs current aperture; this is accomplished with thick (150-nm) mirror layers and a thin (30-nm) current aperture layer [25] due to the thickness-dependence discussed in this section. Another example of using layer thickness to control oxidation rates involves inserting very thin layers of GaAs into an AlAs layer. MacDougal et al. have reduced the oxidation rate of 645 Å of AlAs from 1.164 μm/min to 0.432 μm/min by inserting 20-Å GaAs layers between 161-Å AlAs layers [20].

A novel application of the complete suppression of oxidation for ultra-thin layers has recently been proposed [57]. Because of difficulty in controlling the extent of oxidation and the desirability of doing so for commericial device production, variations in AlAs layer thickness may be used to stop oxidation at a pre-defined extent. Using *in situ* selective growth with the masked MBE method, the thickness of AlAs was decreased from 30 to 15 nm in selected areas, and oxidation was shown to stop at these boundaries.

Surrounding Layers

The oxidation rate of an $Al_xGa_{1-x}As$ layer is enhanced by proximity to an oxidizing layer of higher aluminum content. For example, Blum et al. have found that $Al_{0.94}Ga_{0.06}As$ layers oxidize faster when separated from oxidizing layers of $Al_{0.98}Ga_{0.02}As$ by only thin barriers of GaAs [60]. This effect is reduced as the GaAs layers become thicker, thus impeding transport between the two $Al_xGa_{1-x}As$ layers. A model has been proposed to describe the total oxidized length, ℓ, as the sum of the length for non-interacting layers and a length increase resulting from transport through a thin barrier. This can be written as

$$\ell = \int [k_{lateral}C_{lateral} + k_{barrier}C_r(w,t)]dt, \tag{2.14}$$

where $C_{lateral}$ is the concentration of oxidant responsible for oxidation in isolated layers and C_r(w,t) is the additional concentration of oxidant resulting from transport through a barrier of thickness w. C_r(w,t) is proportional to C_b(w,t), the oxidant concentration inside the barrier at the interface between the GaAs and the lower aluminum-content film. C_b(w,t) can be written as

$$C_b(w,t) = C(0)\left\{1 - erf\left[\frac{w}{(Dt)^{1/2}}\right]\right\}, \tag{2.15}$$

where D is the diffusion constant of the oxidant in the GaAs barrier. Although the model is described in terms of transport of the oxidant, it has not yet been established whether reactants or products are actually moving through the barrier.

Most notably, this effect has been used to create semiconductor microlenses [23]. By adjusting the composition of $Al_xGa_{1-x}As$ layers, it is possible to create an oxide-semiconductor interface with a desired shape. Continuously grading the aluminum content results in a concave profile, while discrete Al-grading ($Al_xGa_{1-x}As$ layers with increasing aluminum composition separated by thin GaAs barriers) produces a convex profile, suitable for the formation of a lens. In the discrete case, vertical contributions to the oxidation rate are reduced relative to those in the case of continuous grading, resulting in the desired shape.

Naone's surface energy model can be used to predict the effect of having low aluminum-content $Al_xGa_{1-x}As$, instead of GaAs, cladding layers on either side of an oxidizing AlAs layer [55]. This can be accomplished by substituting $\Delta\gamma_{AlGaAs}(\mathrm{x})$ for $\Delta\gamma_{GaAs}$ in Equation 2.6, where $\Delta\gamma_{AlGaAs}(\mathrm{x})$ can be written as:

$$\Delta\gamma_{AlGaAs}(x) = (1-x)\Delta\gamma_{GaAs} + x\gamma_{ox/AlAs}. \tag{2.16}$$

With experimentally determined values of 46.6 and 49.6 eV/nm^2 for $\Delta\gamma_{GaAs}$ and $\gamma_{ox/AlAs}$, respectively, Equation 2.16 becomes

$$\Delta\gamma_{AlGaAs}(x) = \Delta\gamma_{GaAs} + x(3.0eV/nm^2). \tag{2.17}$$

Therefore, the model predicts that the barrier-related surface energy, and thus the activation energy of the oxidation reaction, will increase with increasing aluminum concentration.

One of the most intriguing recent results indicates that oxidation rates can be significantly enhanced by the incorporation of a LTG layer below the oxidizing layer. It is not even necessary for the LTG layer to be exposed to the oxidizing atmosphere [51]. Samples containing the LTG layer oxidized faster than standard samples for temperatures ranging from 360 to 450°C, with the greatest difference in oxidation rates observed at 450°C. After ruling out enhanced in-diffusion of reactants and changes in the structure of the oxidizing layer due to the LTG layer, the increased oxidation rate has been attributed to increased out-diffusion of oxidation products through the LTG layer. Champlain et al. report that oxidation rates increase with increasing aluminum content in the LTG layer [61]. This has been cited as evidence that vacancies in the LTG layer are responsible for the increased oxidation rate since higher aluminum-content LTG layers have fewer As antisite defects but more Ga and As vacancies.

Doping of Semiconductor Crystal

The influence of the doping of the semiconductor crystal on oxidation rates has not yet been definitively resolved. Kish et al. first reported that p-type $Al_{0.6}Ga_{0.4}As$ oxidizes more rapidly than n-type $Al_{0.6}Ga_{0.4}As$ and attributed this to the different position of the Fermi level in the two layers since the Fermi level affects the diffusion of ions (such as those involved in the oxidation process) via crystal defects [62]. A later report by the same research group stated that the doping-dependence is substantial only in layers with lower aluminum-content, such as $Al_{0.6}Ga_{0.4}As$ [63], which casts doubt on the wider applicability of their earlier work. However, Ochiai et al. report that p-type AlAs oxidizes faster than n-type AlAs [30], in direct contradiction of the conclusion that doping affects oxidation rates only in low aluminum-content layers.

Although Kish et al. state that the Fermi level, and not the dopant, influences oxidation rates in $Al_{0.6}Ga_{0.4}As$, another report finds that Be- and C-doped AlAs exhibit different oxidation behavior, even though both are p-type [64]. Be-doped AlAs oxidizes at a rate of 1.2 μm/min, independent of doping concentration, while C-doped AlAs oxidizes at 1.75 μm/min. In addition, the C-doped layers show a slight increase in oxidation rate with increasing doping level.

Choquette et al. have proposed an explanation which may account for these observations [65]. No difference in oxidation rate is observed for widely separated n- and p-type layers. However, when the layers are adjacent, they oxidize at different rates, which can be attributed to the built-in field across the p-n junction, rather than the doping of the layers. Therefore, the position of the layers in the crystal, rather than the doping of those layers, may account for the observations reported by other researchers.

Crystallographic Orientation

Most reports of a crystallographic-dependence for the oxidation process are based on the observation of oxide apertures with a shape different from that of the mesas from which they are formed. While square mesas produce square apertures [11, 16, 35, 44, 66, 67], independent of aluminum concentration and orientation of the squares relative to crystal axes [35, 66], several researchers have reported obtaining square or diamond apertures from circular mesas [7, 67, 68, 69]. A more detailed study of this phenomena shows that it is dependent on the aluminum content of the layer being oxidized; for high aluminum-content layers ($\geq$ 94%), circular mesas oxidize to squares, but for low aluminum-content layers ($\leq$ 92%), these mesas produce circular apertures [35, 66]. The composition-dependence can be explained by differences in the local bond configuration of the Al atoms in $\mathrm{Al}_x\mathrm{Ga}_{1-x}\mathrm{As}$; for $x \leq 0.92$, each atom will, on average, have one Ga atom as its second nearest neighbor [35, 66]. Gebretsadik et al. have also noted that the addition of a small amount of Ga causes the oxidation to proceed more isotropically [33].

Based on the observation that the square apertures formed from circular mesas are aligned along the <100> crystal axes, Choquette et al. conclude that the oxidation rate along the <100> axes is faster than that along the <110> axes. This is consistent with the lower surface reactivity of the {110} planes as compared to the {100} planes in GaAs [35, 66]. Li et al. also note that there must be a different oxidation profile along the [011] and $[01\bar{1}]$ directions because of the excellent polarization selection and control observed in oxide-confined VCSELs [69]. Our studies of the relative oxidation rates in different crystallographic directions are presented in Chapter 6.

In addition to these comparisons of oxidation in planes parallel to the semiconductor layers, there have been two additional reports involving oxidation rates along additional crystal directions. Lateral oxidation has been observed to occur approximately 1.5 times faster than vertical oxidation [41]. Kish et al. have noted that oxidation occurs most rapidly along a (111) plane, which can be explained by the higher density of lattice points (and thus more atoms available for oxidation) in the {111} planes as compared to the {100} or {110} planes [70].

2.3.3 Properties of the Oxide Formed by Wet Thermal Oxidation

This section discusses the properties of the oxide formed by wet thermal oxidation of $Al_xGa_{1-x}As$. The oxide's chemical composition, crystal structure, and porosity are discussed first. Next, the thickness contraction of the oxide relative to the original $Al_xGa_{1-x}As$ layer and the resulting mechanical properties of the oxide are considered. Finally, several properties with significant device implications are detailed: passivating, optical, electrical, and thermal characteristics of the oxide.

Chemical Composition

The oxide formed by wet thermal oxidation of $Al_xGa_{1-x}As$ is generally identified as Al_2O_3. However, in addition to aluminum and oxygen, the oxide has also been reported to include hydrogen, gallium, and arsenic. One study even found that the oxides of $Al_{0.5}Ga_{0.5}As$ and $Al_{0.8}Ga_{0.2}As$ contain more hydrogen than oxygen [43]. There is evidence that all of the gallium contained in the original $Al_xGa_{1-x}As$ is incorporated into the oxide [71]. Although most researchers agree that at least some gallium remains in the oxide, a consensus has not yet been reached about its form. While Auger electron spectroscopy (AES) has indicated that the Ga remains unoxidized [72], other researchers have failed to see evidence of Ga precipitates and therefore conclude that the solid solution $(Al_xGa_{1-x})_2O_3$ has been formed [71]. The oxide exhibits a depletion of As relative to the unoxidized $Al_xGa_{1-x}As$, which has been attributed to the escape of As [4, 35, 39], As_2O_3 [4, 72], or AsH_3 [35, 39, 73, 74] from the oxide. While there seems to be very little (less than 2%) As remaining in the oxide [71], the presence of even undetectable amounts of As can have serious consequences for electrical devices incorporating the oxide [4]. Arsenic is thought to be present both as elemental As and in As_2O_3 [39].

Crystal Structure

As stated above, a potentially significant amount of Ga is incorporated into the wet thermal oxide of $Al_xGa_{1-x}As$. However, this is not believed to affect the oxide structure since the oxides of Al and Ga are structural isomorphs [43, 75]. This is further evidenced by the lack of discernible difference in the microstructure of oxides formed from $Al_xGa_{1-x}As$ for $0.8 \leq x \leq 1$ [35] and between oxides formed from $Al_{0.8}Ga_{0.2}As$ and $Al_{0.5}Ga_{0.5}As$ [43].

Identifications of the crystal structure of the wet thermal oxide range from amorphous [29, 35, 42, 43, 76] to polycrystalline γ-Al_2O_3 [4, 71, 74]. Transmission electron spectroscopy (TEM) [42, 43, 76], x-ray diffraction [29], and electron diffraction patterns [35] have all been used to identify the oxide as amorphous. However, other researchers observe rings in selected area electron diffraction patterns which correspond to polycrystalline γ-Al_2O_3 [4, 71, 74]. Using selected area electron diffraction, the lattice constant of the oxide has been measured to be 7.87 Å [74] and 7.95±0.10 Å [71], in favorable agreement with 7.9 Å, the lattice constant of γ- Al_2O_3.

There are several possible explanations for the discrepancy in these identifications. First, those researchers who cite evidence of a polycrystalline structure for the oxide all show that the Al_2O_3 crystallites are small. Electron diffraction patterns are described as faint and diffuse, an indication of small grain sizes [74]. In agreement with evidence cited as proof of an amorphous oxide [29], Ashby et al. note that x-ray data does not show evidence of crystalline phases, putting a limit of approximately 10 nm on the size of the crystallites [4]. Using dark field images, Guha et al. have measured a typical grain size of approximately 8 nm [74], and Twesten et al. find that most grains are approximately 4 nm, with some as small as 1 nm, in diameter [71]. In addition, the dark field images show that any Al_2O_3 crystallites in the oxide are surrounded by an amorphous matrix [71]. Second, there is evidence that the thickness of the oxide layer may affect its microstructure [52]. Some researchers have conjectured that the polycrystalline microstructure of the oxide is the result of mismatch between the oxide and the semiconductor layers above and below [37]. Thin layers should be more affected by this mismatch than thick layers, thus supporting a thickness-dependence for the oxide microstructure. However, other researchers have stated that the microstructure of the oxide formed from $Al_xGa_{1-x}As$ for $0.8 \leq x \leq 1$ is independent of thickness [35]. Perhaps the most convincing explanation is that the electron beam used to measure the structure may induce the transformation from amorphous oxide to the polycrystalline γ-phase [35, 43].

Porosity

There is even less agreement about the porosity of the oxide. Since the oxide masks impurity diffusion [75] and protects AlAs-GaAs heterostructures from atmospheric hydrolysis [73], it has been identified as nonporous [62]. In addition, Kish et al. report that the oxide obeys a parabolic growth law, which is indicative of a nonporous film since the oxidation rate is inversely proportional to the amount of oxide already formed [62]. Guha et al. postulate that even linear oxidation rates, typically indicative of a porous oxide, could result from interfacial porosity, not necessarily porosity of the oxide layer itself [74]. However, researchers who observe a linear growth rate cite this as evidence of a porous oxide since the oxidation rate is independent of the amount of oxide already formed [41]. And, as discussed below, the oxide exhibits less contraction than would be expected for the conversion of a layer from AlAs to dense γ-Al_2O_3, possibly indicating that it is porous [71].

Thickness Contraction

One difference between the wet thermal oxide and compounds formed by low temperature ($< 300°C$) oxidation and atmospheric hydrolysis is the thickness of the resulting film relative to the original layer. While the low temperature processes result in volume expansion [77], layers formed by wet thermal oxidation have been measured to contract by amounts ranging from 2% [52] to 30% [73]. Most researchers have reported a wet thermal oxide thickness of approximately 90% that of the original $Al_xGa_{1-x}As$ layer [21, 37, 42, 66, 71, 78], primarily from TEM measurements. However, recent ellipsometry data indicates that the thickness contraction is only 2-3% [52, 79]. Heremans et al. suggest that the difference between TEM and ellipsometry measurements may be caused by the special sample preparation and resulting ultra-thin samples required for TEM [79].

There is some evidence that oxidation may result in slightly less thickness contraction in $Al_xGa_{1-x}As$ layers as compared to AlAs layers [35, 66], although the largest contraction was measured for an AlGaAs layer [73]. A difference between the thickness of AlGaAs and AlAs oxides could be partially explained by the longer bond length of Ga-O relative to Al-O [35].

The first explanation for the thickness contraction of oxidized AlAs and AlGaAs layers was the 27% smaller molar volume of AlO(OH) as compared to that of AlAs. As a result, Sugg et al. concluded that AlO(OH) must be involved in the oxidation, possibly as an intermediate product [73]. Recently, researchers have focused on the different density of Al atoms in AlAs and in γ-Al_2O_3. The volume per Al atom in AlAs is $(3.57 \text{ Å})^3$, while in γ-Al_2O_3 it is $(2.85 \text{ Å})^3$, thus predicting a 20% thickness contraction in γ- Al_2O_3 layers [71]. As mentioned above, arsenic is thought to escape from AlGaAs layers as they are oxidized; arsenic depletion is also believed to contribute to the volume contraction [73].

Mechanical Properties

The thickness contraction discussed in the preceding section is at least partially responsible for another property of the oxide: its lack of mechanical stability. Strain induced in the semiconductor crystal as the result of the thickness difference between oxidized and unoxidized $Al_xGa_{1-x}As$ is believed to be responsible for mechanical problems [80] such as delamination of the oxide films from other layers after oxidation [4].

There is some evidence that the addition of even small amounts of Ga to AlAs layers may improve the mechanical stability of the resulting oxide. Choquette et al. report that oxides of $Al_xGa_{1-x}As$ with $x \leq 0.98$ show no evidence of the strain and defects that are induced in the surrounding crystal by the oxidation of AlAs [35, 66]. However, micro-Raman measurements show that the tensile deformation of an overlying GaAs layer is the same for AlAs and $Al_{0.98}Ga_{0.02}As$ oxide samples [81].

Mechanical stress may be reduced by oxidizing thin ($\approx$ 20 nm) AlAs layers [35, 64, 82], which eliminates compositional control issues discussed above, while maintaining the mechanical integrity of oxidized crystals. The mechanical stability of oxide-containing structures may also be improved by isolating oxide layers from contact with GaAs, thus preventing the formation of weak Ga-O bonds which could be responsible for the delamination of oxide films [83]. In addition, Dapkus notes that completely oxidized structures induce less strain in the surrounding crystal than partially oxidized layers [80], such as oxide apertures.

Passivating Properties

The passivating properties of the oxide have been recognized since its discovery [54]. Wet thermally oxidized crystals with high Al-content layers do not degrade in atmosphere like their unoxidized counterparts [54] and oxidize slowly [38], if at all [84], when returned to the oxidation furnace. Perhaps more important for device applications, the oxide has been shown to reduce processing damage by sealing cracks and fissures, thus preventing current injection from damaged parts of the semiconductor crystal [85, 86]. As a result, oxidized LEDs show no degradation after 2500 hours at 85°C and 85% relative humidity, while unoxidized LEDs degrade to less than 50% of their original output powers after 1500 hours under the same conditions [86]. In addition, the oxide can be used to reduce surface and shunt junction leakage currents in semiconductor crystals which have been damaged by impurity-induced layer disordering [87].

Optical Properties

As discussed in Section 2.2, the low refractive index of the oxide, relative to that of the semiconductor from which it is formed, is essential to several devices formed with the oxide. The excellent performance of oxide-confined VCSELs is partially due to the optical confinement provided by the index difference between the oxide aperture and adjacent $Al_xGa_{1-x}As$. Distributed Bragg reflectors with increased bandwidth, decreased sensitivity to the thickness and composition of the layers, and reduced growth times are possible because of the large ratio of refractive indices created in the AlGaAs system with the oxidation of high aluminum-content layers.

The refractive index of the oxide is most commonly measured with ellipsometry. Measurements range from 1.50 [5] to approximately 1.7 [88]. For those reports identifying the aluminum content of the $\mathrm{Al}_x\mathrm{Ga}_{1-x}\mathrm{As}$, there doesn't seem to be any correlation between the measured index and the aluminum content of the layer prior to oxidation [5, 41, 72, 88]. However, it is difficult to compare the various measurements since refractive index is a function of wavelength, and most measurements of the index were reported without the corresponding wavelength [21, 38, 78, 79]. Knopp et al. have investigated the wavelength-dependence of the refractive index of the oxide, fitting to a Cauchy dispersion relationship

$$n(\lambda) = A + \frac{B}{\lambda^2} + \frac{C}{\lambda^4} \tag{2.18}$$

for λ in microns, with A = 1.5713, B = 4.83 x 10^{-3} $\mu\mathrm{m}^2$, and C = 9.67 x 10^{-5} $\mu\mathrm{m}^4$ [52]. Further complicating the comparison of various measurements, similar samples with different thicknesses display variations in the refractive index of up to 0.015, with increasing thickness corresponding to decreasing refractive index [52].

Electrical Properties

The excellent electrical properties of oxide-confined VCSELs have been attributed to current confinement provided by the oxide aperture [8]. Because the oxide is electrically insulating [20], the aperture funnels current through the unoxidized region; this reduces the active volume of the device, which results in lower threshold currents. The downside of the electrically insulating nature of the oxide is that VCSELs incorporating oxide-DBRs require careful design to prevent current flow through the insulating oxide layers [20].

There was initial hope that the wet thermal oxidation of $\mathrm{Al}_x\mathrm{Ga}_{1-x}\mathrm{As}$ could be used to form an oxide of sufficient quality for use in III-V MOS devices. Chen et al.

used an oxide formed from AlGaAs to demonstrate the modulation of a depletion-mode metal-oxide-semiconductor field effect transistor (MOSFET) [1]. The oxide was shown to withstand fields greater than 10^7 V/cm. However, Ashby et al. have shown that successful MOS device fabrication schemes will have to address the issue of As precipitates at the oxide-semiconductor interface, which cause Fermi-level pinning [4]. This residual arsenic, the formation of which is thermodynamically favorable [4, 89], has a severe negative impact on MOS device performance; levels as low as 10^{-4} monolayer can degrade MOS device performance. Even devices with As levels below the Raman spectroscopy detection limit exhibit partial Fermi-level pinning and weak modulation.

Thermal Properties

Although the oxide has been reported to have good thermal conductivity [22, 70], its behavior under thermal cycling is less-than-desirable. The volume contraction of the oxide layer and resulting mechanical instability are compounded by the difference in thermal expansion coefficients between the oxide and the surrounding semiconductor [80]. This results in thermal instability, manifested as the delamination [20, 35, 41, 83, 90] and cracking [83, 90, 91] of oxide layers upon thermal annealing.

Some of the same techniques used to improve the mechanical stability of oxide-containing structures may also be used to achieve better thermal behavior. Thin oxide layers show a greater resistance to delamination than thick layers [41, 90]. Structures containing a single oxide layer are more stable under thermal stresses than those containing multiple oxide layers [90]. Thermal stability may also be improved by the use of $Al_xGa_{1-x}As$ oxide layers instead of those formed from AlAs [35, 66]. Several researchers have employed graded AlGaAs layers in DBR structures to reduce the incidence of delamination [20, 83, 90] by preventing the oxide from reaching GaAs layers [83]. The oxide-GaAs interface, which will be discussed further in Section 2.3.4, is believed to support delamination because the contracting Al_2O_3 is much stronger than the GaAs oxide formed at the interface [90]. In addition, there is evidence that the completeness of oxidation may affect the stability of a structure. Samples kept in the oxidation furnace longer than the time required to completely oxidize the mesas showed improved thermal stability [91].

2.3.4 Properties of Oxide-Semiconductor Interfaces

The wet thermal oxide forms interfaces with the unoxidized part of the $Al_xGa_{1-x}As$ layer being oxidized as well as with the surrounding lower aluminum-content $Al_xGa_{1-x}As$ layers. Both types of interfaces are evaluated below.

Interfaces Between Oxidized and Unoxidized $Al_xGa_{1-x}As$

When AlGaAs layers are oxidized vertically from the surface of the semiconductor, both TEM and secondary ion mass spectroscopy (SIMS) show a sharp interface between oxidized and unoxidized parts of the layer [43, 72]. However, a transition region, ranging in width from 2 nm [4] to 17 nm [71], has been observed at the oxidation front in laterally oxidized mesas. Choquette et al. attribute this to a region rich in As_2O_3 [35]. EDX measurements show that the transition region has a reduced Al signal, relative to both oxidized and unoxidized AlAs, and a reduced As signal, as compared to the original AlAs [76]. Twesten et al. report dark-field images showing low atomic-number density cavities within 1 μm of the oxidation front of oxidizing $Al_{0.98}Ga_{0.02}As$ layers but not in oxidizing $Al_{0.92}Ga_{0.08}As$ layers. These cavities are not voids, but rather contain an amorphous material, possibly $Al(OH)_3$ before it is transformed to γ- Al_2O_3 [71].

Interfaces Between Oxide and Surrounding Low Aluminum-Content Layers

The interface between the oxide and surrounding low aluminum-content layers is thought to be quite abrupt. Ellipsometry [52], high-resolution cross-sectional TEM (HRXTEM) [42], and energy-dispersive x-ray micro-analysis (micro-EDX) measurements [76] show a transition or interfacial layer between the oxide and surrounding

GaAs layers of approximately 2 nm. Comparison between chemical (micro-EDX) and visual (HRXTEM) analysis shows that the abruptness of the interface corresponds to the profile of oxygen in the semiconductor [76]. In contrast, there is a small amount of interdiffusion of gallium and aluminum, on the order of 15 nm, in the vicinity of the oxide-GaAs interface [76]. This is consistent with another report that the oxidation process "disorders" the semiconductor crystal within 15 nm of the oxide-semiconductor interface [92]. However, Sugg et al. report that the difference between AlAs and AlGaAs oxides is clearly visible in TEM images, showing that the lateral oxidation does not mix layers [93].

The oxide is found to have a significant negative impact on both interface recombination [33, 45] and photoluminescence [92, 94], as a result of the relatively poor quality of the interface between the oxide and low aluminum-content cladding layers. Interface recombination increases greatly after oxidation [33, 45]; however, this effect is highly dependent upon the compositions of the oxidizing layer and the $Al_xGa_{1-x}As$ cladding layers. Kash et al. have shown that surrounding the oxide layer with $Al_{0.3}Ga_{0.7}As$ instead of GaAs allows interface recombination to remain low after oxidation [45], and oxides of $Al_xGa_{1-x}As$ have much lower interface recombination velocities than those formed from AlAs [33]. In addition, Chou et al. have shown that a thin GaP barrier may be useful in protecting the interface, maintaining both photoluminescence and interface smoothness [50].

The increased interface recombination has been attributed to an increased interface trap density, possibly arising from porosity at the interface [33]. Photoluminescence from quantum wells in close proximity to an oxidized AlAs layer is significantly reduced by the oxidation process. This is believed to be the result of non-radiative recombination centers at the oxide-semiconductor interface [92, 94]. Excess arsenic, forming As_{Ga} antisite defects, has been proposed as a source of traps which could serve as non-radiative recombination centers [92]. Pratt et al. note that the reduction in photoluminescence can be completely eliminated by separating the quantum well from the oxide layer by only 20 nm [94]. Other researchers report that if the oxidized layer is far enough from the quantum well, hydrogen ion treatment can be used to partially restore the luminescence [92], presumably due to the removal of some of the excess arsenic at the interface.

As mentioned in Section 2.3.3, residual arsenic is thought to remain at the oxide-semiconductor interface after oxidation. High-resolution TEM reveals Moire fringes, attributed to 2- to 4-nm As crystallites at the interface [4]. Instead of arsenic, Guha et al. have observed voids at the oxide-semiconductor interface. These are believed to be caused by high stress at the interface due to the oxidation process, consistent with the formation of defects extending to a few hundred angstroms on either side of the interface [74]. However, this contradicts reports that no defects are introduced by the oxidation [35, 47, 80], as well as another report that there is no evidence for interfacial voiding [71]. Other researchers have noted that the interface is readily damaged by electron beam irradiation [42], perhaps causing the formation of voids [35, 95].

2.3.5 Oxidation Reaction

As discussed in Section 2.3.3, the wet thermal oxide of AlAs is believed to be Al_2O_3. In addition, AlO(OH) is thought to be involved in the oxidation reaction. At the temperatures used for oxidation, AlO(OH) is converted to γ- Al_2O_3 [74]. The high quality of the wet thermal oxide has been attributed to the formation of AlO(OH) and Al_2O_3 compounds, in contrast to $Al(OH)_3$ believed to be formed by the destructive atmospheric hydrolysis process [73]. Twesten et al. propose that the wet thermal oxidation proceeds from amorphous $Al(OH)_3$ to γ-Al_2O_3 [71]. However, all other researchers describe the reaction chemistry without this destructive compound.

For simplicity, this section describes the reactions believed to be responsible for the wet thermal oxidation of AlAs. The oxidation of $Al_xGa_{1-x}As$ is believed to follow a similar reaction chemistry since the oxides of Al and Ga form an extended series of solid solutions $Al_xGa_{1-x}O(OH)$ and $(Al_xGa_{1-x})_2O_3$ [43].

Initial descriptions of the oxidation chemistry emphasized the role of arsine in the removal of As from the oxide film. The following reactions were proposed for the wet thermal oxidation:

$$AlAs + 2H_2O \rightarrow AlO(OH) + AsH_3 \tag{2.19}$$

and

$$2AlAs + 3H_2O \rightarrow Al_2O_3 + 2AsH_3. \tag{2.20}$$

In addition, another reaction was proposed for additional As removal:

$$AlO(OH) + AlAs + H_2O \rightarrow Al_2O_3 + AsH_3. \tag{2.21}$$

Reactions involving As_2O_3 were excluded from consideration because of the significant As depletion observed in SIMS data [73].

Recent analysis of the oxidation reaction has resulted in the proposal of a significant role for As_2O_3, supported by Raman spectroscopy, which reveals a constant signal from both As and amorphous As_2O_3 as the oxidation proceeds [4]. Therefore, both As and As_2O_3 are thought to be present as intermediate products of the oxidation [39]. Reactions which produce As and As_2O_3, in addition to Al_2O_3, and are thermodynamically favorable at oxidation temperatures are [35, 39]:

$$2AlAs + 6H_2O \rightarrow Al_2O_3 + As_2O_3 + 6H_2, \tag{2.22}$$

$$As_2O_3 + 3H_2 \rightarrow 2As + 3H_2O, \tag{2.23}$$

and

$$As_2O_3 + 6H \rightarrow 2As + 3H_2O. \tag{2.24}$$

The role of these reactions is supported by the importance of hydrogen in the oxidation process, as evidenced by the inability of the oxidation to proceed under oxygen carrier gas, which would be expected to consume the available hydrogen [35, 39]. Because both As and As_2O_3 can serve as volatile products for the removal of As from the oxide, the formation of arsine is not necessary to account for the observed As depletion [4]. However, it is not possible to exclude the role of AsH_3 in removing As because its formation using atomic hydrogen is favorable at typical oxidation temperatures [35, 39].

At the interface between the oxide and GaAs cladding layers, another reaction must be considered. As_2O_3 is believed to be thermodynamically unstable in the presence of GaAs, reacting to form arsenic [4, 89]:

$$As_2O_3 + 2GaAs \rightarrow 4As + Ga_2O_3. \tag{2.25}$$

This reaction is supported by Raman spectroscopy data near the oxide-semiconductor interface, which shows that the As_2O_3 signal drops below the detection limit while the As signal persists [4]. The conversion of As_2O_3 to As may explain the Fermi-level pinning observed in MOS devices, as discussed in Section 2.3.3.

Bibliography

[1] E. Chen, N. Holonyak, Jr., and S. Maranowski, Appl. Phys. Lett. **66**, 2688 (1995).

[2] P. Parikh, S. Shi, J. Ibettson, E. Hu, and U. Mishra, Electron. Lett. **32**, 1724 (1996).

[3] P. Grudowski, R. Chelakara, and R. Dupuis, Appl. Phys. Lett. **69**, 388 (1996).

[4] C. Ashby, J. Sullivan, P. Newcomer, N. Missert, H. Hou, B. Hammons, M. Hafich, and A. Baca, Appl. Phys. Lett. **70**, 2443 (1997).

[5] F. Kish, S. Caracci, N. Holonyak, Jr., J. Dallesasse, K. Hsieh, M. Ries, S. Smith, and R. Burnham, Appl. Phys Lett. **59**, 1755 (1991).

[6] S. A. Maranowski, A. R. Sugg, E. I. Chen, and N. Holonyak, Jr., Appl. Phys. Lett. **63**, 1660 (1993).

[7] D. Huffaker, D. Deppe, and K. Kumar, Appl. Phys. Lett. **65**, 97 (1994).

[8] K. Lear, K. Choquette, R. Schneider, Jr., S. Kilcoyne, and K. Geib, Electron. Lett. **31**, 208 (1995).

[9] K. Lear, R. Schneider, Jr., K. Choquette, and S. Kilcoyne, IEEE Photon. Technol. Lett. **8**, 740 (1996).

[10] K. Choquette, K. Lear, R. Schneider, Jr., and K. Geib, Appl. Phys. Lett. **66**, 3413 (1995).

[11] K. Lear, K. Choquette, R. Schneider, Jr., and S. Kilcoyne, Appl. Phys. Lett. **66**, 2616 (1995).

[12] K. Lear, R. Schneider, Jr., K. Choquette, S. Kilcoyne, J. Figiel, and J. Zolper, IEEE Photon. Technol. Lett. **6**, 1053 (1994).

[13] G. Yang, M. MacDougal, and P. Dapkus, Electron. Lett. **31**, 886 (1995).

[14] P. Dapkus, discussion, 1996.

[15] D. Huffaker, J. Shin, and D. Deppe, Electron. Lett. **30**, 1946 (1994).

[16] G. Yang, M. MacDougal, and P. Dapkus, J. Appl. Phys. **80**, 4837 (1996).

[17] H. Deng and D. Deppe, Electron. Lett. **32**, 900 (1996).

[18] T.-H. Oh, D. Huffaker, and D. Deppe, Appl. Phys Lett. **69**, 3152 (1996).

[19] K. Choquette, R. Schneider, Jr., M. Crawford, K. Geib, and J. Figiel, Electron. Lett. **31**, 1145 (1995).

[20] M. MacDougal, P. Dapkus, A. Bond, C.-K. Lin, and J. Geske, IEEE J. Select. Topics Quantum Electron. **3**, 905 (1997).

[21] M. MacDougal, H. Zhao, P. Dapkus, M. Ziari, and W. Steier, Electron. Lett. **30**, 1147 (1994).

[22] M. MacDougal, G. Yang, A. Bond, C.-K. Lin, D. Tishinin, and P. Dapkus, IEEE Photon. Technol. Lett. **8**, 310 (1996).

[23] O. Blum, K. Lear, H. Hou, and M. Warren, Electron. Lett. **32**, 1406 (1996).

[24] A. Fiore, V. Berger, E. Rosencher, N. Laurent, S. Theilmann, N. Vodjdani, and J. Nagle, Appl. Phys. Lett. **68**, 1320 (1996).

[25] A. Bond and P. Dapkus, Appl. Phys. Lett. **73**, 19 (1998).

[26] O. Sjölund, D. Louderback, E. Hegblom, J. Ko, and L. Coldren, Appl. Phys. Lett. **73**, 1 (1998).

[27] A. Fiore, Y. Akulova, J. Ko, E. Hegblom, and L. Coldren, Appl. Phys. Lett. **73**, 282 (1998).

[28] P. Chavarkar, L.-J. Zhao, S. Keller, S. Mathis, A. Black, E. Hu, J. Speck, and U. Mishra, Electronic Materials Conference **AA8**, (1998).

[29] N. Kobayashi, J. Kobayashi, P. Dapkus, W.-J. Choi, A. Bond, X. Zhang, and D. Rich, Appl. Phys. Lett. **71**, 3569 (1997).

[30] M. Ochiai, G. Giudice, H. Temkin, J. Scott, and T. Cockerill, Appl. Phys. Lett. **68**, 1898 (1996).

[31] R. Naone, E. Hegblom, B. Thibeault, and L. Coldren, Electron. Lett. **33**, 300 (1997).

[32] This is a typical water bubbler temperature, used by many researchers.

[33] H. Gebretsadik, K. Zhang, K. Kamath, X. Zhang, and P. Bhattacharya, Appl. Phys. Lett. **71**, 3865 (1997).

[34] This is a typical nitrogen flow rate, used by many researchers.

[35] K. Choquette, K. Geib, C. Ashby, R. Twesten, O. Blum, H. Hou, D. Follstaedt, B. Hammons, D. Mathes, and R. Hull, IEEE J. Select. Topics Quantum Electron. **3**, 916 (1997).

[36] T. Kuech, discussion, 1997.

[37] T. Langenfelder, S. Schröder, and H. Grothe, J. Appl. Phys. **82**, 3548 (1997).

[38] R. Burton and T. Schlesinger, J. Appl. Phys. **76**, 5503 (1994).

[39] C. Ashby, J. Sullivan, K. Choquette, K. Geib, and H. Hou, J. Appl. Phys. **82**, 3134 (1997).

[40] B. Koley, M. Dagenais, R. Jin, G. Simonis, J. Pham, G. McLane, F. Johnson, and R. Whaley, Jr., J. Appl. Phys. **84**, 600 (1998).

[41] H. Nickel, J. Appl. Phys. **78**, 5201 (1995).

[42] T. Takamori, K. Takemasa, and T. Kamijoh, Appl. Phys. Lett. **69**, 659 (1996).

[43] F. Kish, S. Caracci, N. Holonyak, Jr., K. Hsieh, J. Baker, S. Maranowski, A. Sugg, and J. Dallesasse, J. Electron. Mater. **21**, 1133 (1992).

[44] K. Choquette, R. Schneider, Jr., K. Lear, and K. Geib, Electron. Lett. **30**, 2043 (1994).

[45] J. Kash, B. Pezeshki, F. Agahi, and N. Bojarczuk, Appl. Phys. Lett. **67**, 2022 (1995).

[46] P. Evans and N. Holonyak, Jr., Appl. Phys. Lett. **71**, 261 (1997).

[47] K. Choquette, K. Lear, R. Schneider, Jr., K. Geib, J. Figiel, and R. Hull, IEEE Photon. Technol. Lett. **7**, 1237 (1995).

[48] T.-H. Oh, D. Huffaker, L. Graham, H. Deng, and D. Deppe, Electron. Lett. **33**, 2024 (1996).

[49] L. Chou, K. Hsieh, D. Wohlert, K. Cheng, and N. Finnegan, J. Appl. Phys. **84**, 6932 (1998).

[50] L. Chou, K. Hsieh, A. Moy, D. Wohlert, G. Pickrell, and K. Cheng, Appl. Phys. Lett. **72**, 2722 (1998).

[51] H. Reese, Y. Chiu, and E. Hu, Appl. Phys. Lett. **73**, 2624 (1998).

[52] K. Knopp, R. Mirin, D. Christensen, K. Bertness, A. Roshko, and R. Synowicki, Appl. Phys. Lett. **73**, 3512 (1998).

[53] H. Reese, Y. Chiu, A. Shakouri, E. Hu, and J. Bowers, Electronic Materials Conference **R7**, (1997).

[54] J. Dallesasse, N. Holonyak, Jr., A. Sugg, T. Richard, and N. El-Zein, Appl. Phys Lett. **57**, 2844 (1990).

[55] R. Naone and L. Coldren, J. Appl. Phys. **82**, 2277 (1997).

[56] J.-H. Kim, D. Lim, K. Kim, G. Yang, K. Lim, and H. Lee, Appl. Phys. Lett. **69**, 3357 (1996).

[57] T. Yoshikawa, H. Saito, H. Kosaka, Y. Sugimoto, and K. Kasahara, Appl. Phys. Lett. **72**, 2310 (1998).

[58] M. Ochiai, G. Guidice, and H. Temkin, Workshop on Native Oxides of Compound Semiconductors (1997).

[59] B. Deal and A. Grove, J. Appl. Phys. **36**, 3770 (1965).

[60] O. Blum, C. Ashby, and H. Hou, Appl. Phys. Lett. **70**, 2870 (1997).

[61] J. Champlain, P. Parikh, J. Ibbetson, and U. Mishra, Electronic Materials Conference **BB6**, (1998).

[62] F. Kish, S. Maranowski, G. Höfler, N. Holonyak, Jr., S. Caracci, J. Dallesasse, and K. Hsieh, Appl. Phys. Lett. **60**, 3165 (1992).

[63] S. Maranowski, N. Holonyak, Jr., T. Richard, and F. Kish, Appl. Phys Lett. **62**, 2087 (1993).

[64] B. Weigel, M. Grabherr, C. Jung, R. Jäger, G. Reiner, R. Michalzik, D. Sowasa, and K. J. Ebeling, IEEE J. Select. Topics Quantum Electron. **3**, 409 (1997).

[65] K. Choquette, K. Geib, H. Hou, and B. Hammons, Workshop on Native Oxides of Compound Semiconductors (1997).

[66] K. Choquette, K. Geib, H. Chui, B. Hammons, H. Hou, T. Drummond, and R. Hull, Appl. Phys. Lett. **69**, 1385 (1996).

[67] H.-E. Shin, Y.-G. Ju, J.-H. Shin, J.-H. Ser, T. Kim, E.-K. Kee, I. Kim, and Y.-H. Lee, Electron. Lett. **32**, 1287 (1996).

[68] P. Floyd, B. Thibeault, L. Coldren, and J. Merz, Electron. Lett. **32**, 114 (1996).

[69] G. Li, S. Lim, W. Yuen, and C. Chang-Hasnain, Electron. Lett. **31**, 2014 (1995).

[70] F. Kish, S. Caracci, S. Maranowski, N. Holonyak, Jr., C. Kuo, R. Fletcher, T. Osentowski, and M. Crawford, J. Appl. Phys. **71**, 2521 (1992).

[71] R. Twesten, D. Follstaedt, K. Choquette, and R. Schneider, Jr., Appl. Phys. Lett. **69**, 19 (1996).

[72] A. Sugg, E. Chen, N. Holonyak, Jr., K. Hsieh, J. Baker, and N. Finnegan, J. Appl. Phys. **74**, 3880 (1993).

[73] A. Sugg, N. Holonyak, Jr., J. Baker, F. Kish, and J. Dallesasse, Appl. Phys Lett. **58**, 1199 (1991).

[74] S. Guha, F. Agahi, B. Pezeshki, J. Kash, D. Kasker, and N. Bojarczuk, Appl. Phys. Lett. **68**, 906 (1996).

[75] J. Dallesasse, N. Holonyak, Jr., N. El-Zein, T. Richard, F. Kish, A. Sugg, R. Burnham, and S. Smith, Appl. Phys Lett. **58**, 974 (1991).

[76] T. Takamori, K. Takemasa, and T. Kamijoh, Appl. Surf. Sci. **117/118**, 705 (1997).

[77] W. Tsang, Appl. Phys. Lett. **33**, 426 (1978).

[78] M. MacDougal, S. Hummel, P. Dapkus, H. Zhao, and Y. Cheng, IEEE Photon. Technol. Lett. **7**, 385 (1995).

[79] P. Heremans, M. Kuijk, R. Windisch, J. Vanderhaegen, H. De Neve, R. Vounckx, and G. Borghs, J. Appl. Phys. **82**, 5265 (1997).

[80] D. Deppe, D. Huffaker, T.-H. Oh, H. Deng, and Q. Deng, IEEE J. Select. Topics Quantum Electron. **3**, 893 (1997).

[81] J. Landesman, A. Fiore, J. Nagle, V. Berger, E. Rosencher, and P. Puech, Appl. Phys. Lett. **71**, 2520 (1997).

[82] D. Huffaker and D. Deppe, Appl. Phys Lett. **70**, 1781 (1997).

[83] M. MacDougal and P. Dapkus, IEEE Photon. Technol. Lett. **9**, 884 (1997).

[84] D. Lim, G. Yang, J.-H. Kim, K. Lim, and H. Lee, Appl. Phys. Lett. **71**, 1915 (1997).

[85] S. Maranowski, E. Chen, N. Holonyak, Jr., and T. Richard, Appl. Phys. Lett. **64**, 2151 (1994).

[86] T. Richard, N. Holonyak, Jr., F. Kish, M. Keever, and C. Lei, Appl. Phys. Lett. **66**, 2972 (1995).

[87] F. Kish, S. Caracci, N. Holonyak, Jr., J. Dallesasse, G. Höfler, R. Burnham, and S. Smith, Appl. Phys Lett. **58**, 1765 (1991).

[88] A. Holmes, M. Islam, R. Chelakara, F. Ciuba, R. Dupuis, M. Ries, E. Chen, S. Maranowski, and N. Holonyak, Jr., Appl. Phys. Lett. **66**, 2831 (1995).

[89] Y.-L. Chang, S. Yi, S. Shi, E. Hu, W. Weinberg, and J. Merz, J. Vac. Sci. Technol. B **13**, 1801 (1995).

[90] P. Evans, J. Wierer, and N. Holonyak, Jr., J. Appl. Phys. **84**, 5436 (1998).

[91] A. Bond, C.-K. Lin, M. MacDougal, P. Dapkus, K. Kaviani, O. Adamczyk, and R. Nottenburg, Electron. Lett. **32**, 2271 (1996).

[92] S. Shi, E. Hu, J.-P. Zhang, Y.-I. Chang, P. Parikh, and U. Mishra, Appl. Phys. Lett. **70**, 1293 (1997).

[93] A. Sugg, E. Chen, T. Richard, N. Holonyak, Jr., and K. Hsieh, J. Appl. Phys. **74**, 797 (1993).

[94] A. Pratt, T. Takamori, and T. Kamijoh, Appl. Phys. Lett. **71**, 1394 (1997).

[95] K. Choquette, Workshop on Native Oxides of Compound Semiconductors (1997).

Chapter 3 Experimental Set-Up and Procedures

3.1 Introduction and Chapter Outline

In this chapter, detailed information is provided about the set-up and procedures used in our experiments. The equipment in our oxidation set-up is described in Section 3.2. Section 3.3 details the wet thermal oxidation procedure as well as techniques used for data collection.

3.2 Details of the Oxidation Set-Up

The basic set-up used in our experiments is shown in Figure 3.1. This set-up was specifically designed and assembled to perform the wet thermal oxidation experiments described in this thesis. The furnace is a three-zone tube furnace (Blue M model #IHTF55347C with temperature controller Blue M model #CC58434C). Inside the furnace is a 2"-diameter quartz tube which tapers at one end for connection to vinyl tubing from the water bubbler. The other end of the tube is loosely covered with a quartz cap through which the sample insertion rod is free to slide. The sample insertion rod consists of a quartz rod with a flat quartz plate at one end. The rod bends slightly before reaching the quartz plate to ensure that the plate is at the same level as the center of the rod and thus that samples on the plate will be in the center of the furnace. To avoid putting too much pressure on the quartz cap, the end of the sample insertion rod is supported by a metal plate attached to the lab bench. This plate has a hole drilled through it which is slightly larger than the diameter of the rod and at the same level as the hole through the quartz cap. During oxidation the sample insertion rod is pushed into the furnace just far enough to center samples horizontally.

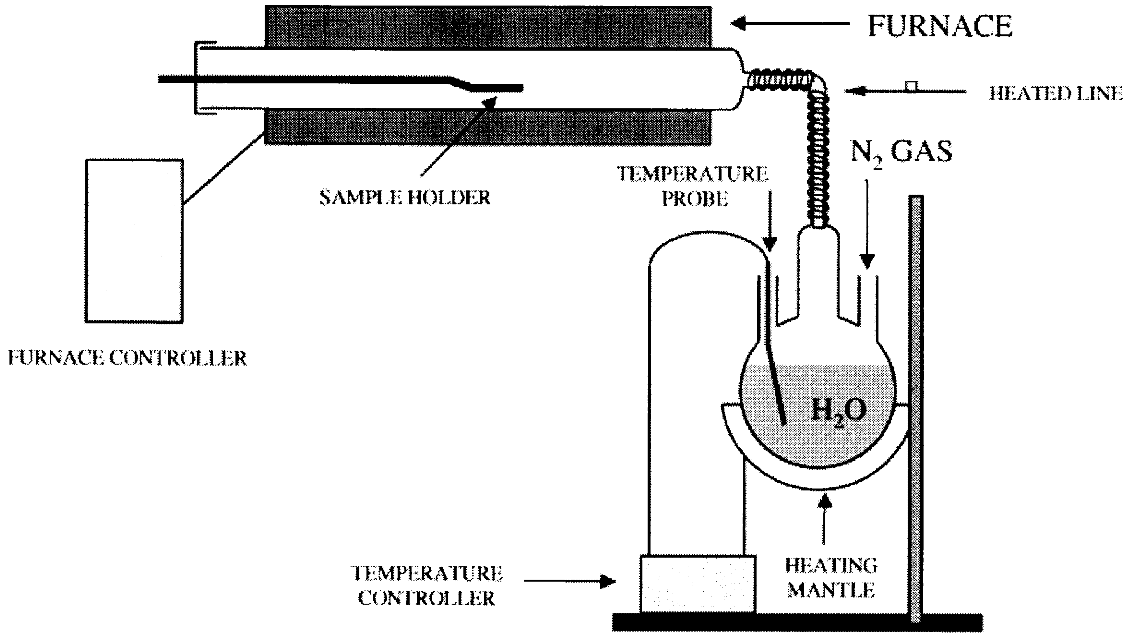

Figure 3.1: Illustration of the set-up used in the wet thermal oxidation experiments described in this thesis.

The nitrogen used in our experiments is at least 99.9999% pure (Matheson ULSI purity). A two-stage regulator (Matheson model #3810-580) is used to control gas flow from the cylinder. The nitrogen travels through 316 stainless steel tubing from the gas cylinder to a 0.01-μm particle filter (Matheson model #6190) attached to a gas flow meter (Cole-Parmer model #E-32641-50). The output from the flow meter is attached (with vinyl tubing) to a Teflon® 3-way diaphragm valve (Cole-Parmer model #E-06482-00). The 3-way valve directs nitrogen either straight towards the furnace or through the water bubbler, which will be discussed in more detail shortly. All tubing is connected to the valve with Teflon® PFA fittings (Cole Parmer model #E-06373-92). The output tube from the water bubbler passes through a check valve into a T-connector, where it meets the tube straight from the flow meter, which has also passed through a check valve. These neoprene check valves (Cole-Parmer model #E-06304-10) prevent the backwards flow of water vapor in the system. The third outlet of the T-connector is connected with vinyl tubing to the end of the furnace tube. The flow of nitrogen through the system is shown in Figure 3.2.

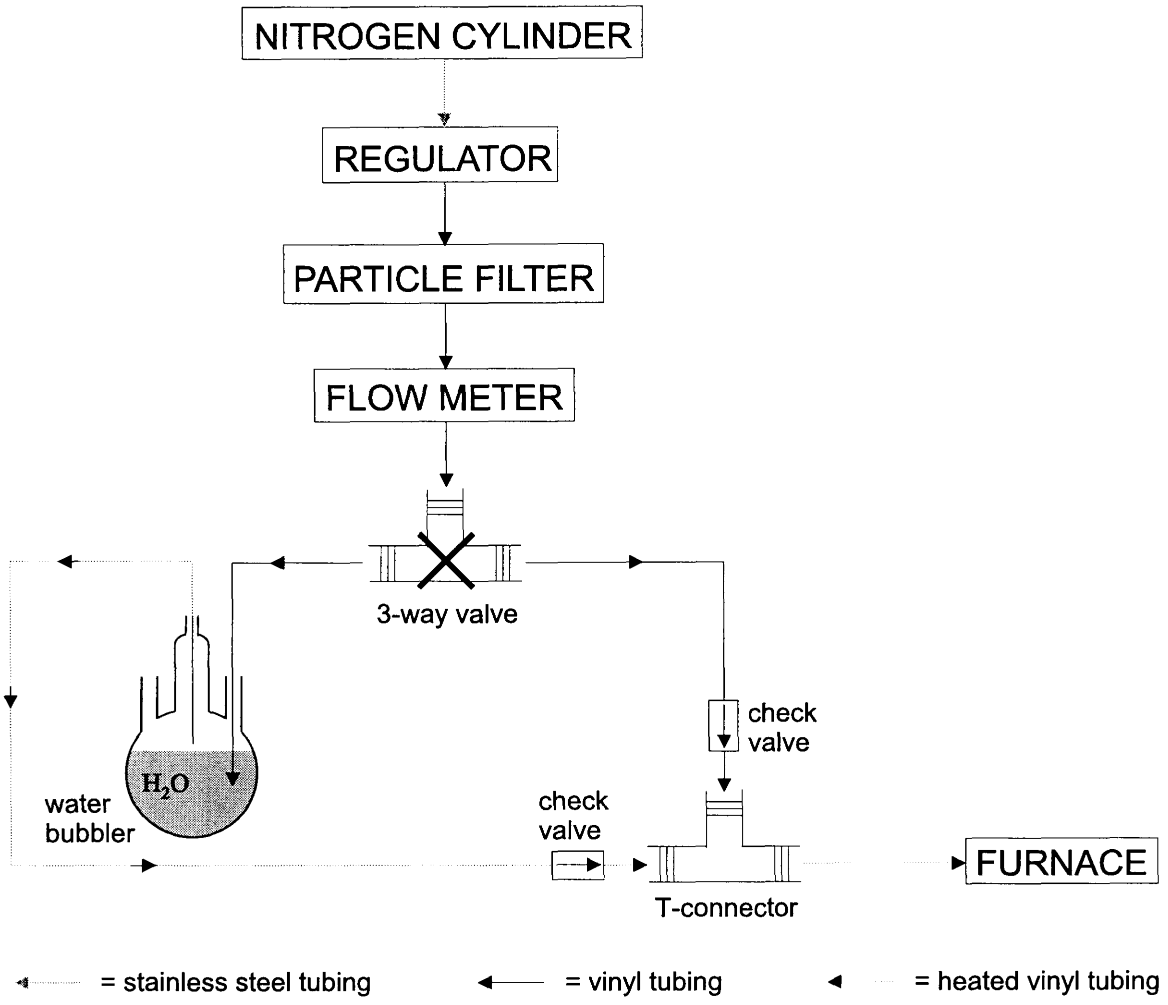

Figure 3.2: Diagram of nitrogen flow through the wet thermal oxidation system.

As explained in Chapter 2, tubing between the water bubbler and the furnace (before and after the T-connector) is heated. In order to do this, the vinyl tubing is wrapped with a 120 V rope heater (Omega model #FGR-030) and covered with aluminum foil to provide uniform heating. Power to the rope heater is supplied by a variable voltage source (Powerstat model #3PN126). The temperature is controlled with an Omega universal temperature controller (Omega model #CN8501-TC-R1:G1) and a J type thermocouple (Omega model #TIN-116J). The thermocouple is held in contact with the tubing by placing it under the aluminum foil. The connections to the temperature controller are shown in Figure 3.3. When the setpoint of the temperature controller is set to 110°C and the variable voltage source outputs 55 volts, the temperature measured by the thermocouple is approximately 105°C.

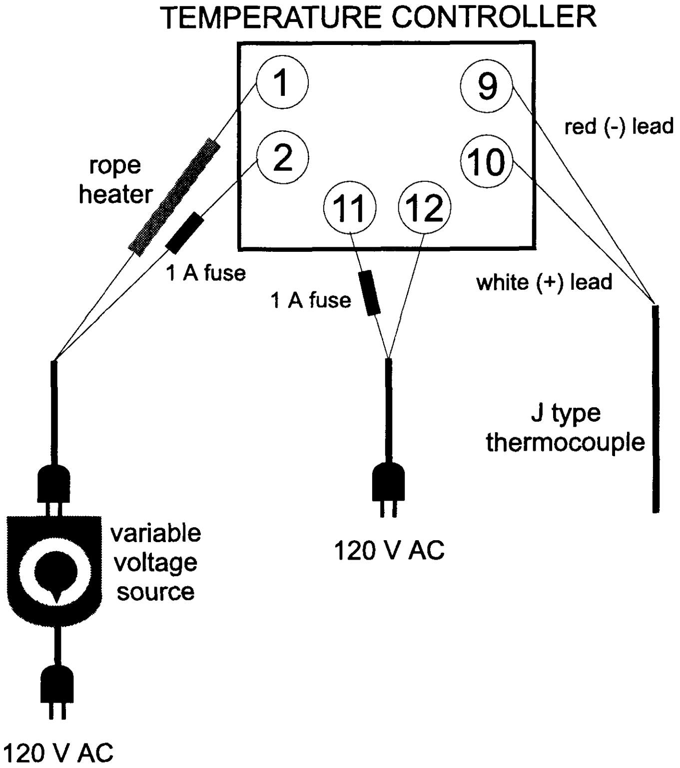

Figure 3.3: Diagram of connections to the rope heater temperature controller. This system controls the heating of the tubing between the water bubbler and the furnace.

The main part of the water bubbler is a 3000 mL Pyrex distilling flask with three necks (VWR model #29280-420). The center neck of the flask has a §45/50 joint, while the two side necks have §24/40 joints. The vinyl tubing from the flow meter passes into one of the side necks through a §24/40 connector with a hole through the middle (Kimble-Kontes model #182900-2440) so that a portion of the tubing is under the level of the water in the flask. The other side neck has a bevel seal, allowing the insertion of a thermocouple into the flask while maintaining a tight seal. The center neck holds a specially-made glass piece which has a §45/50 connector on one end and tapers to the inner diameter of the vinyl tubing at the other end. It is attached to the vinyl tubing which leads to the furnace through the check valve and T-connector. The water in the flask is heated with a Glass-Col heating mantle (Cole-Parmer models #E-36225-60 and E-36225-86), controlled by a Glass-Col temperature controller (Cole-Parmer model #E-36225-90) with temperature feedback provided by a type J thermocouple probe.

3.3 Procedures for Wet Thermal Oxidation Experiments

This section details the procedures used in our wet thermal oxidation experiments. Section 3.3.1 describes the sample and system preparation as well as the exact steps used to oxidize samples in our experiments. Section 3.3.2 explains the procedures used to measure oxidation lengths.

3.3.1 Oxidation Procedures

Before starting the wet thermal oxidation process, the system, as described in Section 3.2, was turned on and allowed to reach equilibrium. First, the water bubbler was filled with deionized water. The initial level of water in the flask was just below the bottom of the necks so that the flow of nitrogen into the flask would not cause water to bubble up into the necks. With the 3-way valve turned to bypass the water bubbler, the flow of nitrogen was turned on using the regulator on the gas cylinder. The flow meter was used to set the nitrogen flow to 1 liter/min. Next, the temperature controller for the water bubbler heating mantle was turned on, allowing the water bubbler to begin heating up. The temperature on the controller was set to a value determined by calibration to result in a water bubbler temperature of 95°C and was not changed between oxidation runs. Then, the furnace was turned on and set to the desired temperature. Finally, the heating rope temperature controller (with a setpoint of 110°C) was plugged in, and the variable voltage source was set to 55 V. The nitrogen flow was not directed through the water bubbler until both the water bubbler and the tubing connecting it to the furnace had reached their final temperatures. After nitrogen began flowing through the water bubbler, the system was allowed to equilibriate for 2 hours before any samples were oxidized.

The samples used in the experiments described in this thesis were grown on (100) GaAs substrates in a Perkin Elmer molecular beam epitaxy (MBE) machine. Our standard sample contained a 100-nm AlAs oxide layer, surrounded on either side by 15 nm of $Al_{0.3}Ga_{0.7}As$. The structure was capped with 150 nm of GaAs. Standard photolithography procedures were used to define mesas (150 μm-wide stripes, 150 μm-diameter circles, or 150 μm x 150 μm squares). Hardened photoresist served as an etch mask when the samples were placed in 1:8:80 H_2SO_4:H_2O_2:H_2O for 90 seconds to remove the material around the mesas, exposing the AlAs layer. Each sample was etched immediately before being inserted into the furnace; the delay between etching and the start of oxidation was less than 5 minutes.

The quartz rod was heated in the furnace during the system preparation described above; it was removed from the furnace briefly to place a sample on the quartz plate for oxidation. Although the plate was designed and fabricated with grooves to hold the samples vertically, in all of the oxidation experiments described in this thesis, the samples were placed flat on the plate. There are three reasons for this: (1) the samples used in our experiments were small enough that a significant fraction would have been inside the groove if placed vertically; (2) heat conduction between the sample and the quartz plate is improved by putting a larger surface area of the sample in contact with the plate, thus decreasing the time required for the sample to reach the temperature of the furnace [1]; and (3) the gas flow around the sample is expected to be more uniform when the sample is flat against the plate [1]. The oxidation time was started when the sample reached the edge of the furnace (although it continued to be pushed to the center of the furnace). Just prior to the end of oxidation, the sample rod was pulled out so that the time was stopped when the sample again reached the edge of the furnace. Because of the high temperature of the quartz rod, metal (instead of fluoroware) tweezers were used to move samples onto and off of the quartz plate. For long oxidation runs, the water level in the bubbler was monitored, and the bubbler was refilled if necessary, keeping at least 1500 mL of water in the bubbler at all times.

To turn off the oxidation system, first the nitrogen flow was switched to bypass the water bubbler. Next, the water bubbler heater was turned off. Then, the variable voltage source was turned off, and the rope heater was unplugged. If desired, condensation in the furnace could be removed by leaving the furnace and nitrogen flow on for a few hours. Finally, the furnace was turned off, and the nitrogen flow was terminated, first with the flow meter and then with the regulator on the gas cylinder.

3.3.2 Data Collection Procedures

An optical microscope and CCD camera were used to obtain JPG images of the mesas. Those with obvious deformities were excluded from further analysis. The remaining images were then inserted into a drawing program (CorelDraw) to measure the size of both the original mesa and the portion that remained unoxidized. This was accomplished by overlaying a stripe, square, or circle on top of the image of the mesa and adjusting the size of the shape until it matched that of the mesa or aperture being measured. The oxidation length $x_\circ$ was obtained by subtracting the length or diameter of the unoxidized portion from the length or diameter of the original mesa and dividing the result by two. The measurement was converted from pixels to μm with a multiplication factor obtained by taking pictures of an optical standard (Newport Optics model #USAF-1951-RES-2).

Bibliography

[1] T. Kuech, discussion, 1997.

Chapter 4 Model for the Time-Dependence of the Wet Thermal Oxidation Process

4.1 Introduction and Chapter Outline

This chapter presents a new model for the time-dependence of wet thermal oxidation in two-dimensional mesa structures. Recently, other researchers have proposed models for the oxidation of circular mesas, but we believe that our model most accurately accounts for the influence of geometry on the oxidation process. Although our model contains approximations, we consider it to be the best mathematical description available at this time for the wet thermal oxidation process in circular mesas. In addition, it represents, to our knowledge, the first and only attempt to model this process in square mesas.

Both circular and square mesas are used in VCSELs because they create an active region more closely aligned with the desired shape of the output laser beam. With increasingly complicated VSCEL structures being proposed, it becomes more important to understand how the oxidation process proceeds in both circular and square mesas. Despite this important application and the fact that a model for the oxidation of stripes does not accurately describe oxidation in circular or square mesas, there have been few studies which explore oxidation in these geometries. In fact, when this research was started, the only studies of wet thermal oxidation rates had been conducted with stripes.

Section 4.2 describes the one-dimensional model which is widely accepted for the wet thermal oxidation process. Our model is presented in Section 4.3. It can be applied to mesas of practically any shape. However, in this study, we have focused on circles and squares, since they are the most relevant to real devices. Application of our model to oxidation in circular and square mesas is demonstrated in Sections 4.4 and 4.5, respectively. A critique of other models for wet thermal oxidation in cylindrical geometry and comparison to our model are presented in Section 4.6.

4.2 Accepted Model for the Oxidation of Stripes

The model generally used to describe the wet thermal oxidation of $\mathrm{Al}_x\mathrm{Ga}_{1-x}\mathrm{As}$ in stripes is based upon the Grove and Deal model for the oxidation of silicon [1]. Ochiai et al. were first to apply this model to the problem of wet thermal oxidation [2]. The Grove and Deal model assumes a steady-state process so that the flux of oxidant molecules is constant in three components of the oxidation:

1. transport of oxidant molecules to the edge of the mesa
2. diffusion of oxidant molecules through the already-formed oxide
3. reaction at the oxide-semiconductor interface.

Once these fluxes have been equated, the growth rate of the oxide layer is described as

$$\frac{dx_\circ}{dt} = \frac{F}{N_0}, \tag{4.1}$$

where $x_\circ$ represents the position of the oxidation front (the oxide-semiconductor interface), F is the constant flux of oxidant molecules, and N_0 is the number of oxidant molecules incorporated into a unit volume of oxide. Assuming there is no oxide present at time $t = 0$, Equation 4.1 can be integrated to yield

$$t = \frac{x_\circ^2}{B} + \frac{x_\circ}{B/A}, \tag{4.2}$$

where

$$A = 2D\left(\frac{1}{k} + \frac{1}{h}\right) \tag{4.3}$$

and

$$B = \frac{2DC^*}{N_0}. \tag{4.4}$$

In Equation 4.3, k is a constant governing the oxidation reaction and h is a gas-phase transport coefficient. In Equations 4.3 and 4.4, D is the effective diffusion coefficient for transport of oxidant molecules through the oxide; in Equation 4.4, C* is the equilibrium concentration of oxidant molecules in the oxide.

Equation 4.2 can be rewritten as

$$x_\circ(t) = \frac{A}{2}\left(\sqrt{1 + \frac{t}{A^2/4B}} - 1\right) \tag{4.5}$$

and considered in two limiting cases. In the first regime, valid for t $\ll \frac{A^2}{4B}$, Equation 4.2 reduces to a linear growth law:

$$x_\circ \approx \frac{B}{A}t. \tag{4.6}$$

For t $\gg \frac{A^2}{4B}$, a parabolic growth law is obtained:

$$x_\circ^2 \approx Bt. \tag{4.7}$$

Thus, the oxidation of stripes is expected to exhibit an initially linear growth, followed by a slowing of the oxidation rate in the parabolic growth regime.

4.3 Presentation of Our Model

This section describes our model for the wet thermal oxidation process. Section 4.3.1 contains a basic description of the assumptions and calculations which comprise this model. One unique aspect of our model is that it can be applied to a variety of mesa geometries. For comparison to the Grove and Deal model, Section 4.3.2 demonstrates the application of our model to the oxidation of stripes.

4.3.1 Description of Our Model

For two-dimensional oxidation, such as the case of circular and square mesas, the surface area of the oxide-semiconductor interface changes as the oxidation proceeds, effectively changing the geometry of the oxidation. Therefore, we do not believe that the steady-state assumption of the Grove and Deal model is valid in these cases. As noted by Ochiai et al., the functional form for the oxidation of stripes in Equation 4.2 is composed of a diffusion and a reaction component [2], $\frac{x_\circ^2}{B}$ and $\frac{x_\circ}{B/A}$, respectively. Therefore, our model treats the movement of the oxidation front in terms of diffusion of the reactant to the oxide-semiconductor interface and reaction at that interface. Although the reaction term in Equation 4.2 also depends upon the transport of oxidant molecules in the gas phase, this is not generally considered to be a rate-limiting factor in the oxidation and is not included in our model. This is equivalent to assuming that there is an adequate supply of reactant at the edge of the mesa. In addition, we assume that the removal of As-containing products is not the rate-limiting process. Although not explicitly stated, Ochiai et al. also make this assumption because the Grove and Deal model does not include the out-diffusion of products.

Following the general form of the Grove and Deal model, Equation 4.2, our model takes the oxidation time to be the sum of the time required for reactant atoms to diffuse to the oxide-semiconductor interface and the time required for the atoms to react at that interface:

$$t_{oxidation}(x_\circ) = t_{diffusion}(x_\circ) + t_{reaction}(x_\circ). \tag{4.8}$$

To obtain an expression for the diffusion time, we start with the diffusion equation

$$\frac{\partial C}{\partial t_{diffusion}} = D\nabla^2 C \tag{4.9}$$

in appropriate coordinates – rectangular for stripes and square mesas, cylindrical for circular mesas. The following boundary conditions apply to the diffusion equation:

1. There are no oxidant molecules inside the mesa when the oxidation begins (i.e., at $t_{diffusion} = 0$).
2. There is a constant concentration, $C_\circ$, of oxidant molecules at the edge of the mesa at all times.

With these boundary conditions, we obtain a solution to Equation 4.9, expressing oxidant concentration inside the mesa as a function of both position and diffusion time. Next, we assume that the oxidation front, as seen in Figure 4.1, occurs where the oxidant concentration is half that at the edge of the mesa. Choosing some other fraction does not change the functional form of the solution [3] but does affect the absolute value of the diffusion constant obtained for the oxidation. The diffusion time is obtained by setting the concentration at the interface equal to half that at the edge of the mesa:

$$C_{interface} = 0.5C_\circ. \tag{4.10}$$

An expression for the reaction time is obtained by writing equivalent representations of the number of atoms reacted in a time $dt_{reaction}$:

$$Rdt_{reaction} = \rho dV, \tag{4.11}$$

where R is the reaction rate (in units of atoms per unit time), ρ is the concentration of oxidant molecules in the oxide, and dV is the volume of oxide which must react to move the oxide front by a differential unit of length.

This model is not specific to any one mesa geometry, and thus can be applied to the oxidation of stripes as well as circular and square mesas. In fact, oxidation in any mesa geometry can be considered provided that

1. The diffusion equation can be solved with the boundary conditions enumerated above.
2. The volume of oxide required to move the oxidation front by a differential unit of length can be specified.

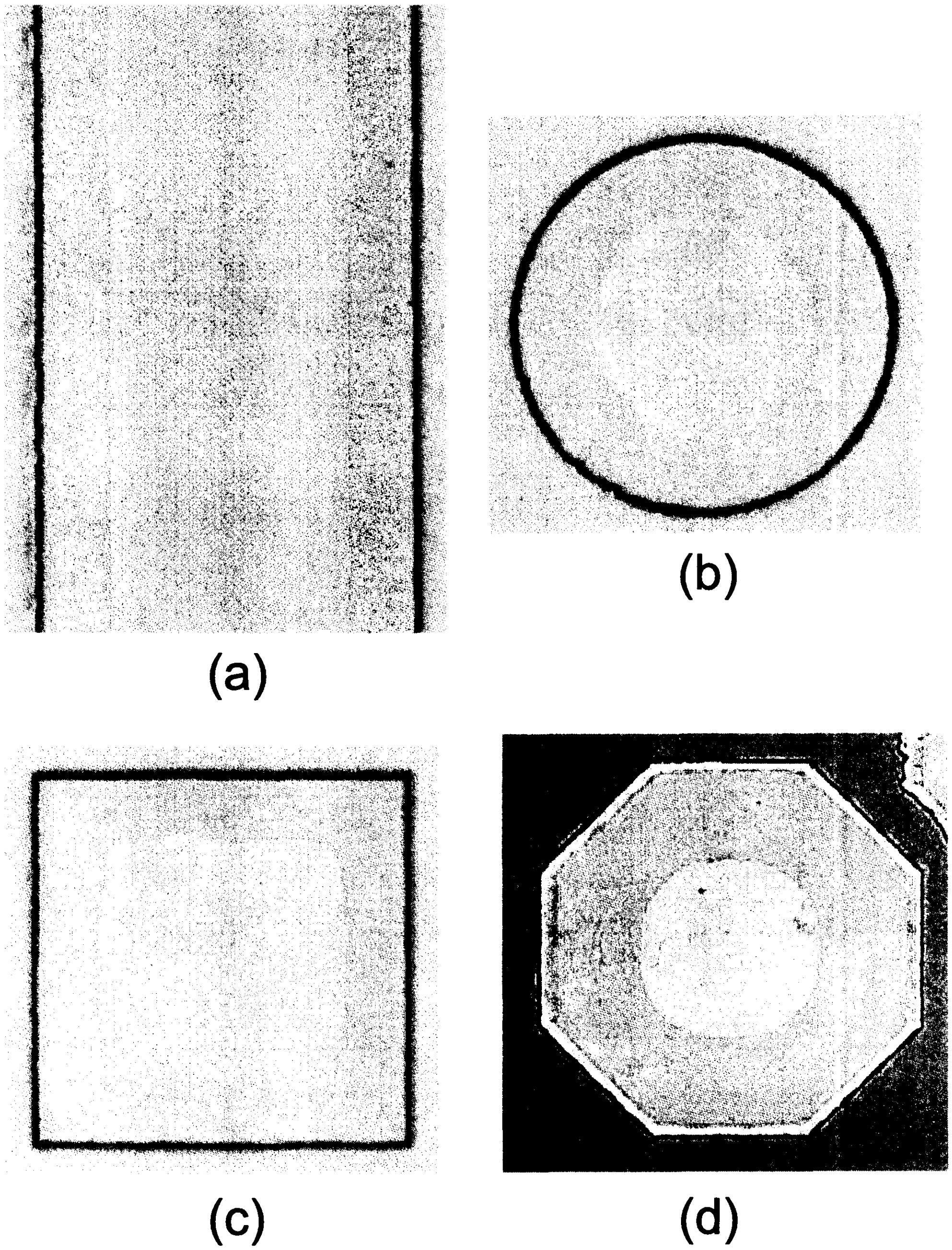

Figure 4.1: Images of oxidized mesas, as seen through an optical microscope. The oxidized AlAs layer is viewed through 150 nm GaAs and 15 nm $Al_{0.3}Ga_{0.7}As$. Figures (a) - (c) show mesas from the same sample which was oxidized for 40 minutes at 375°C. (a) Portion of partially oxidized 150 μm-wide stripe. (b) Partially oxidized 150 μm-diameter circular mesa. (c) Partially oxidized 150 μm x 150 μm square mesa. (d) Octagon, 200 μm across, which was partially oxidized for one hour at 425°C.

4.3.2 Application of Our Model to the Oxidation of Stripes

Applying our model to the oxidation of stripes yields the same functional form as that of the Grove and Deal model. First considering the diffusion component of the oxidation, we write a solution for the diffusion equation in rectangular coordinates with the boundary conditions described in Section 4.3.1:

$$C(x_\circ, t) = C_\circ \left[1 - Erf\left(\frac{x_\circ}{2\sqrt{Dt_{diffusion}}}\right)\right]. \tag{4.12}$$

To obtain $t_{diffusion}$, we set Equation 4.12 equal to 0.5C$_\circ$, which yields:

$$t_{diffusion} = \frac{x_\circ^2}{k_D}, \tag{4.13}$$

where

$$k_D = 4D\left[Erf^{-1}(0.5)\right]^2. \tag{4.14}$$

Figure 4.2(a) shows the relationship between the diffusion time and the position of the oxide-semiconductor interface.

Returning to Equation 4.11, we write dV for stripes as

$$dV = LHdx, \tag{4.15}$$

where L is the length of the stripe and H is the thickness of the oxidizing layer. We define a rate

$$k_R = \frac{R}{\rho\sigma}, \tag{4.16}$$

where σ is the outside surface area of the mesa. For stripes, σ = LH so that Equation 4.11 can be written as

$$k_R dt_{reaction} = dx. \tag{4.17}$$

Equation 4.17 is subject to the boundary condition that no oxide has been formed at

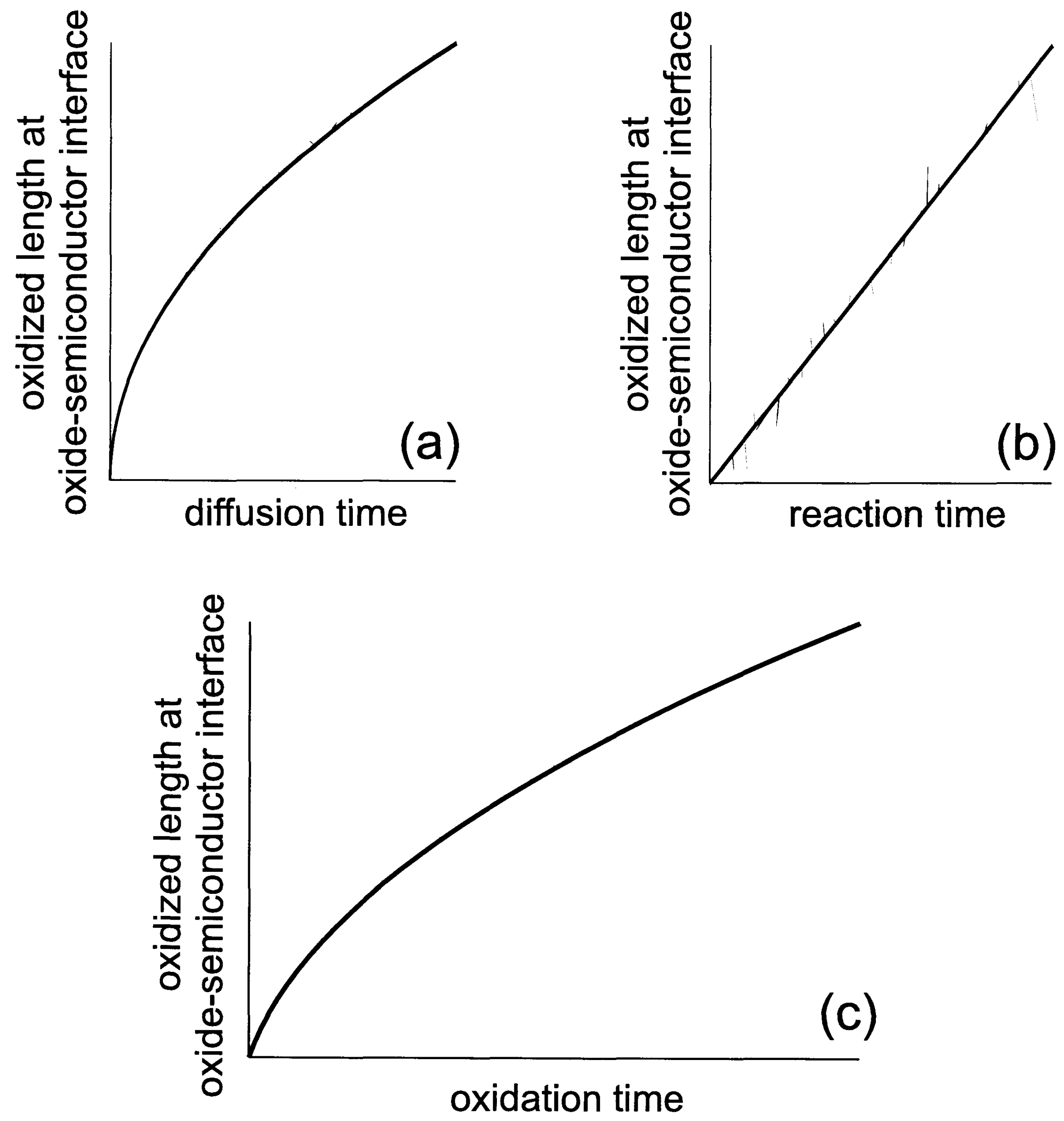

Figure 4.2: This figure illustrates the functional forms of the processes involved in the oxidation of stripes. (a) Functional form for the diffusion of oxidant molecules to the oxide-semiconductor interface in stripes. (b) Functional form for the reaction of oxidant molecules to move the oxide-semiconductor interface in stripes. (c) Functional form for the wet thermal oxidation of stripes.

time t = 0, i.e., $x_\circ(t_{reaction} = 0) = 0$, yielding

$$t_{reaction} = \frac{x_\circ}{k_R}. \tag{4.18}$$

This relationship is shown in Figure 4.2(b).

Substituting Equations 4.13 and 4.18 into Equation 4.8 yields a relationship between the oxidation time and oxidation length in stripes:

$$t = \frac{x_\circ^2}{k_D} + \frac{x_\circ}{k_R}, \tag{4.19}$$

which is shown in Figure 4.2(c) and has the same functional form as Grove and Deal's expression in Equation 4.2.

4.4 Application of Our Model to the Oxidation of Circular Mesas

For the oxidation of circular mesas, we start by writing the diffusion equation in cylindrical coordinates [4]:

$$\frac{\partial C}{\partial t_{diffusion}} = \frac{1}{r}\frac{\partial}{\partial r}\left(rD\frac{\partial C}{\partial r}\right). \tag{4.20}$$

For a mesa of radius a, the boundary conditions can be written as:

1. C(t=0,r<a) = 0
2. C(r=a) = $C_\circ$.

Carslaw and Jaeger give a solution to this problem [5]:

$$C(r, t_{diffusion}) = C_\circ \left[1 - \frac{2}{a}\sum_{n=1}^{\infty} e^{-D\alpha_n^2 t_{diffusion}} \frac{J_0(r\alpha_n)}{\alpha_n J_1(a\alpha_n)}\right], \tag{4.21}$$

where J_n represents the nth-order Bessel function and the $\{\alpha_n\}$s are solutions to $J_0(a\alpha_n) = 0$. We numerically solve the equation $C(r,t_{diffusion}) = 0.5C_\circ$ to obtain an expression for the radius of the oxidation front (and thus the oxidized length $x_\circ = a - r$) as a function of the diffusion time. The resulting curve is plotted in Figure 4.3(a).

Now considering the reaction component, we return to Equation 4.11, writing dV as

$$dV = -2\pi Hrdr, \tag{4.22}$$

where, as in Equation 4.15 for stripes, H is the thickness of the oxidizing layer. With the rate k_R defined as in Equation 4.16 and $\sigma = 2\pi Ha$, Equation 4.11 can be written as

$$k_R dt_{reaction} = -\frac{r}{a}dr. \tag{4.23}$$

Equation 4.23 is subject to the boundary condition that no oxide has been formed at time $t = 0$, i.e., $r(t_{reaction} = 0) = a$, yielding

$$t_{reaction} = \frac{2ax_\circ - x_\circ^2}{2ak_R}. \tag{4.24}$$

Solving Equation 4.24 for $x_\circ(t_{reaction})$ yields

$$x_\circ = a - \sqrt{a^2 - 2ak_R t_{reaction}}. \tag{4.25}$$

This curve is shown in Figure 4.3(b).

Following Equation 4.8, our oxidation model for circular mesas is completed by adding the diffusion and reaction times for a given oxidation length $x_\circ$. The resulting curve is plotted in Figure 4.3(c). It is clear from this curve that the oxidation of circular mesas is predicted to proceed in a much different manner from that of stripes.

4.5 Application of Our Model to the Oxidation of Square Mesas

For stripes and circular mesas, the shape of the oxide-semiconductor interface remains constant throughout the oxidation. However, in squares, the shape of the interface

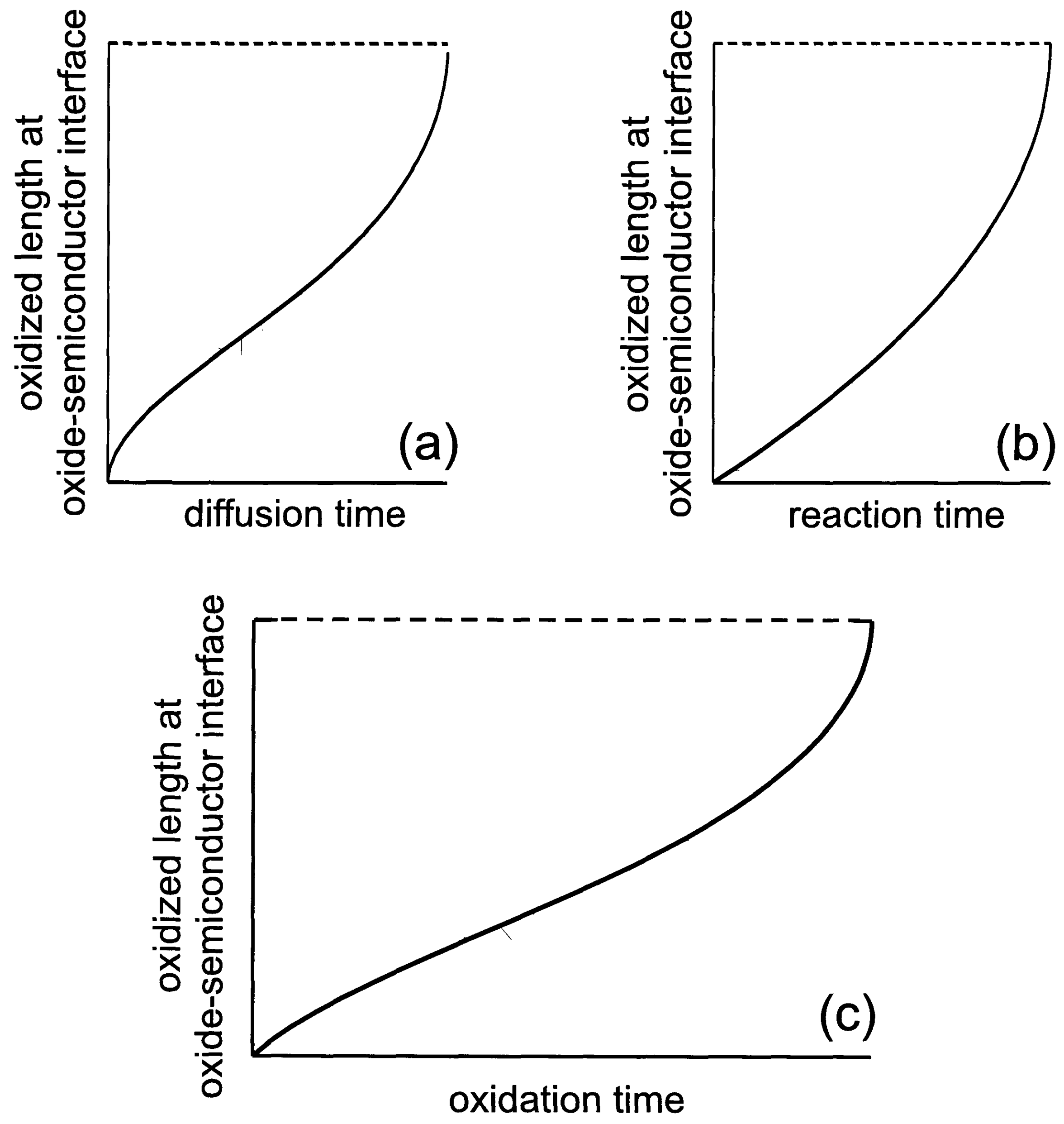

Figure 4.3: This figure illustrates the functional forms of the processes involved in the oxidation of circular mesas. (a) Functional form for the diffusion of oxidant molecules to the oxide-semiconductor interface in circular mesas. (b) Functional form for the reaction of oxidant molecules to move the oxide-semiconductor interface in circular mesas. (c) Functional form for the wet thermal oxidation of circular mesas.

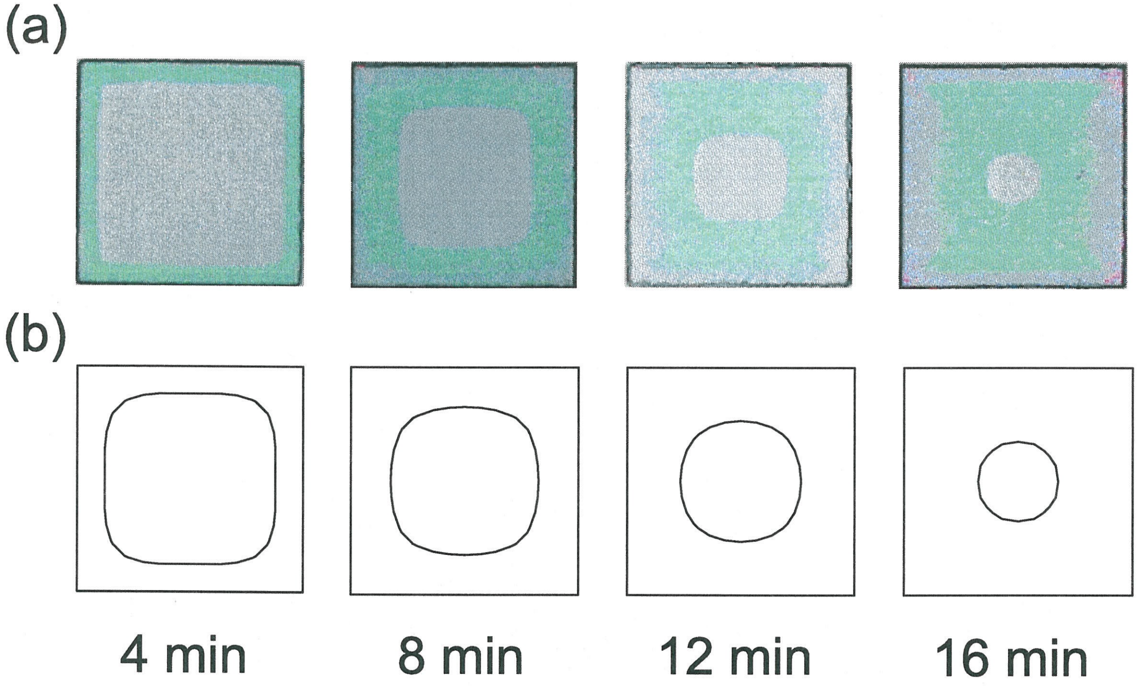

Figure 4.4: This figure shows how the shape of the oxide-semiconductor interface changes as a square mesa is oxidized. (a) Optical microscope pictures of 150 μm x 150 μm square mesas, oxidized at 425°C for 4, 8, 12, and 16 minutes. (b) Mathematica plots showing the shape of the $C = 0.5C_o$ contours for $t_{diffusion} = 4$, 8, 12, and 16 minutes with a diffusion constant of 71.25 $\mu m^2/min$.

changes as the oxidation proceeds, as seen in Figure 4.4(a). Since we have defined the location of the oxidation front as the locus of points at which the concentration of oxidant molecules is $0.5C_o$, the shape of the oxidation front is defined by the diffusion part of the oxidation. For a square with sides of length 2a, the boundary conditions placed on the diffusion equation are:

1. $C(-a<x<a,-a<y<a,t=0) = 0$
2. $C(x=a) = C(x=-a) = C(y=a) = C(y=-a) = C_o$.

Following the formalism discussed by Carslaw and Jaeger [5], we can write the solution to the diffusion equation, subject to the above boundary conditions, as:

$$C(x, y, t_{diffusion}) = \tag{4.26}$$
$$C_\circ - \frac{16C_\circ}{\pi^2}\sum_{l}^{\infty}\sum_{m}^{\infty}\frac{(-1)^{l+m}}{(2l+1)(2m+1)}\cos\left[\frac{(2l+1)\pi x}{2a}\right]\cos\left[\frac{(2m+1)\pi y}{2a}\right] exp^{-D\alpha_{lm}t_{diffusion}},$$

where α_{lm} is defined as:

$$\alpha_{lm} = \left[\frac{(2l+1)\pi}{2a}\right]^2 + \left[\frac{(2m+1)\pi}{2a}\right]^2. \tag{4.27}$$

Setting $C(x_{interface}, y_{interface}, t_{diffusion})$ equal to $0.5C_\circ$, we can obtain a set of $(x_{interface}, y_{interface})$ values which satisfy the equality for a given $t_{diffusion}$. As shown in Figure 4.4(b), the shape of the oxidation front defined by these values changes with time, as expected from experimental observations.

Before proceeding with our analysis of the oxidation in square mesas, we need to consider what is meant by the oxidation length in a partially oxidized square mesa. We have chosen to define the oxidation length as the extent of oxidation in the x-direction at y = 0:

$$x_\circ(t) = a - x_{interface}(y_{interface} = 0, t), \tag{4.28}$$

as illustrated in Figure 4.5. Thus, to obtain an expression for $t_{diffusion}$ as a function of $x_\circ$, we solve

$$C(x = a - x_\circ, y = 0, t = t_{diffusion}) = 0.5C_\circ, \tag{4.29}$$

with C(x,y,t) given in Equation 4.26. Equation 4.29 must be solved numerically and yields the relationship shown in Figure 4.6(a).

Now considering the reaction component, we need an expression for the volume of oxide reacted to move the oxidation front by a differential unit of length. This volume depends upon the shape of the oxidation front for a given oxidation length as well as its shape after an additional increment of oxide has been formed. Most generally, this can be expressed as

$$dV = H\left[\int_0^{2\pi} r_{interface}(\theta, x_\circ)d\theta\right]dx_\circ, \tag{4.30}$$

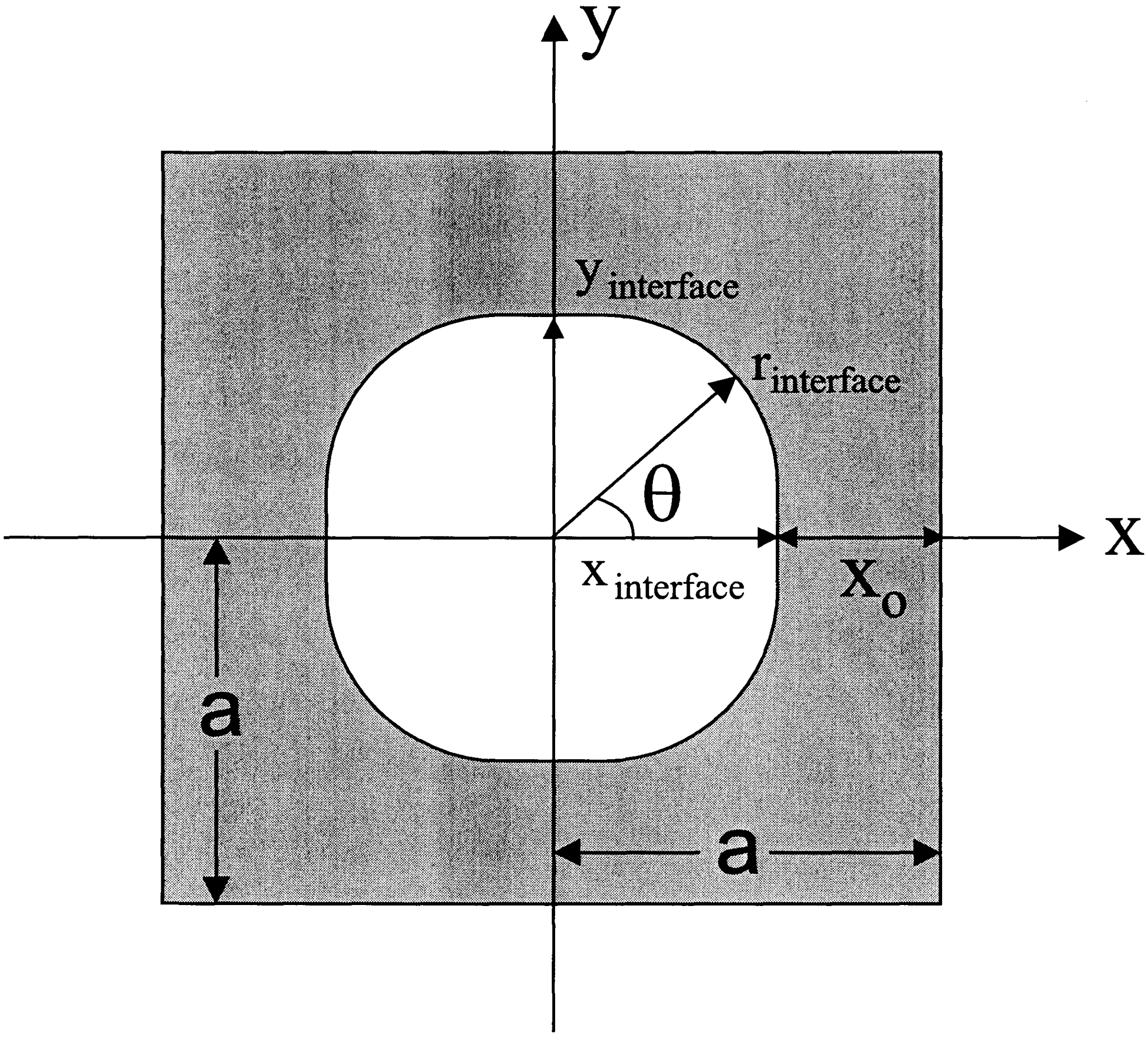

Figure 4.5: This figure illustrates the variables involved in our model for the oxidation of square mesas.

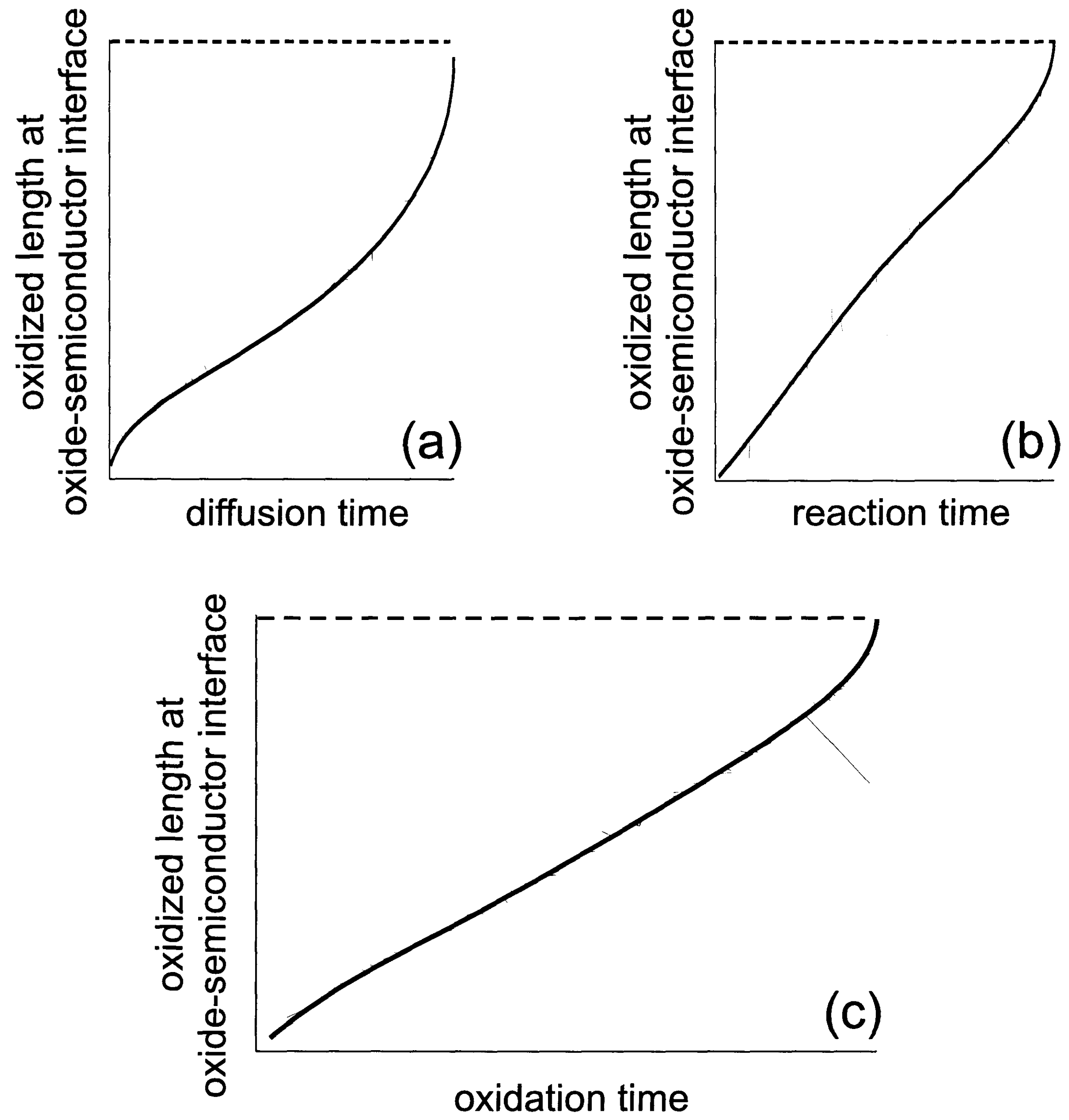

Figure 4.6: This figure illustrates the functional forms of the processes involved in the oxidation of square mesas. (a) Functional form for the diffusion of oxidant molecules to the oxide-semiconductor interface in square mesas. (b) Functional form for the reaction of oxidant molecules to move the oxide-semiconductor interface in square mesas. (c) Functional form for the wet thermal oxidation of square mesas.

where $r_{interface}(\theta, x_\circ)$ describes the shape of the aperture and is determined by the diffusion equation. Unfortunately, an analytical expression cannot be obtained for $r_{interface}(\theta, x_\circ)$, so an approximation is required. We start by describing the shape of the aperture as

$$x_{interface}^2 + y_{interface}^2 - \frac{f(a - x_\circ)x_{interface}^2 y_{interface}^2}{(a - x_\circ)^2} = (a - x_\circ)^2. \qquad (4.31)$$

To obtain an expression for $f(a - x_\circ)$, we first solve Equation 4.31 for $y_{interface}$ as a function of $x_{interface}$ for a given oxidation extent:

$$y_{interface} = (a - x_\circ)\sqrt{\frac{(a - x_\circ)^2 - x_{interface}^2}{(a - x_\circ)^2 - f(a - x_\circ)x_{interface}^2}}. \qquad (4.32)$$

Next we generate a set of $(x_{interface}, y_{interface})$ pairs for a given value of $x_\circ$ by solving

$$C(x = x_{interface}, y = y_{interface}, t = t_\circ) = 0.5C_\circ, \qquad (4.33)$$

where $C(x,y,t)$ is given in Equation 4.26 and $t_\circ$, the value of $t_{diffusion}$ corresponding to $x_\circ$, is obtained from Equation 4.29. By fitting Equation 4.32 to the values generated with Equation 4.33, we can calculate a value of $f(a - x_\circ)$ for a given oxide extent. Repeating this procedure for a number of $x_\circ$ values results in a set of $(x_\circ, f)$ pairs. Finally, we take a function which approximates the curve formed by the $(x_\circ, f)$ points:

$$f(a - x_\circ) = A + B\tanh\left[\frac{a - x_\circ}{C} - D\right], \qquad (4.34)$$

and fit this form to our generated values of f and $x_\circ$ to obtain A = 0.55202, B = 0.52647, C = 16.90952, and D = 2.90555. The $(x_\circ, f)$ points and the curve generated from Equation 4.34 to approximate $f(a - x_\circ)$ are plotted in Figure 4.7.

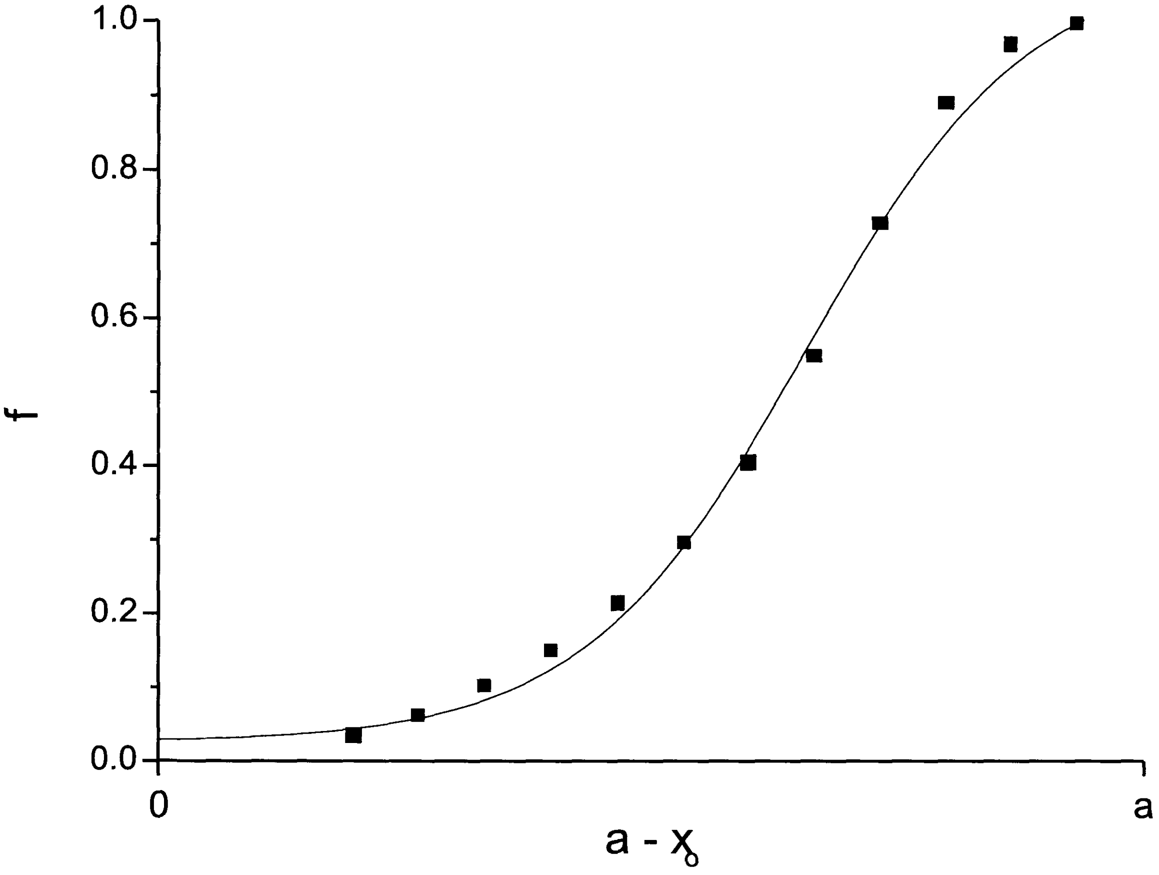

Figure 4.7: This figure shows the function f(a - x_o), used in Equation 4.35 to approximate the shape of the oxide-semiconductor interface in square mesas. The data points were obtained by fitting Equation 4.32 to ($x_{interface}$,$y_{interface}$) pairs generated from the diffusion equation, using Equation 4.33. The curve, whose mathematical representation is given in Equation 4.34, is an approximation to the function represented by the data points.

Relating rectangular to cylindrical coordinates ($r^2 = x^2 + y^2$, $x = r\cos\theta$, and $y = r\sin\theta$), we can solve Equation 4.31 for $r_{interface}$, yielding

$$r_{interface}(\theta, x_o) = \sqrt{\frac{(a-x_o)^2}{2f(a-x_o)sin^2\theta cos^2\theta}\left[1+\sqrt{1-4f(a-x_o)sin^2\theta cos^2\theta}\right]}. \quad (4.35)$$

Returning to Equation 4.11 with dV as given in Equation 4.30 we can write

$$Rdt_{reaction} = \quad (4.36)$$
$$\rho H \left[\int_0^{2\pi} \sqrt{\frac{(a-x_o)^2}{2f(a-x_o)sin^2\theta cos^2\theta}\left[1+\sqrt{1-4f(a-x_o)sin^2\theta cos^2\theta}\right]}\right] dx_o.,$$

Defining q = a - x_o and applying the boundary condition $x_o(t{=}0) = 0$, the reaction time becomes:

$$t_{reaction} = \frac{1}{8k_R a}\int_{a-x_o}^{a}\int_0^{2\pi}\sqrt{\frac{q^2}{2f(q)sin^2\theta cos^2\theta}\left[1+\sqrt{1-4f(q)sin^2\theta cos^2\theta}\right]}d\theta dq, \quad (4.37)$$

where k_R is defined as in Equation 4.16 with σ = 8Ha. The relationship between $t_{reaction}$ and x_o, as given in Equation 4.37, is shown in Figure 4.6(b).

Finally, we sum the diffusion and reaction times for a given oxidation length x_o. The resulting curve is plotted in Figure 4.6(c).

4.6 Comparison Between Our Model and Those Proposed by Other Researchers for the Oxidation of Circular Mesas

This section compares our model for the oxidation of circular mesas, as presented in Section 4.4, to those recently proposed by other researchers. These models are reviewed in Section 4.6.1 and critiqued in Section 4.6.2.

4.6.1 Other Models for the Oxidation of Circular Mesas

Koley et al. have proposed a model for the oxidation of circular mesas [6] which is based upon the Grove and Deal model. Fluxes due to transport, diffusion, and reaction are considered in cylindrical geometry. While expressions for the fluxes corresponding to transport and reaction are unchanged in this model, the diffusion flux is rewritten to reflect the different solution to the diffusion equation in cylindrical geometry. Koley et al. equate $\int F \cdot dA$ at each of the interfaces, which is equivalent to equating the fluxes in the one-dimensional case. Similar to the case for stripes (Equation 4.1), the growth rate of the oxide layer can be written as

$$\frac{dR_1}{dt} = \frac{F}{N_0}, \tag{4.38}$$

where R_1 is the radius of the oxide-semiconductor interface. For a circular mesa of radius R_0, integration yields an expression relating the oxidized length $x = R_0 - R_1$ and the time:

$$Bt = \frac{x^2}{2} + (A + R_0)x + A\beta x\left(1 - \frac{x}{R_0}\right) + (R_0 - x)^2 ln\left(1 - \frac{x}{R_0}\right). \tag{4.39}$$

In the above equation, A and B are defined as in Equations 4.3 and 4.4, and β is defined as

$$\beta = \frac{k}{k + h}, \tag{4.40}$$

where k and h are Grove and Deal's reaction and gas phase transport coefficients, respectively.

Another model has been proposed by Langenfelder et al. which starts from an entirely different theoretical conception of the oxidation process [7]. The oxidation length in this model is written as

$$x(t) = x_\infty\left[1 - exp\left(-\frac{g_0}{x_\infty}t\right)\right], \tag{4.41}$$

where $g_0 = \frac{\partial x}{\partial t}\mid_{t=0}$ is the initial growth rate. This model assumes that the oxidized area of a circular mesa of radius R_o should be the same as the oxidized area of a rectangle with length $2\pi R_o$. Therefore, the oxidized length in the circular mesa, x_c, can be expressed as a function of the oxidized length in the rectangle, x_r:

$$x_c = R_o\left(1 - \sqrt{1 - \frac{2x_r}{R_o}}\right). \tag{4.42}$$

Therefore, the oxidized length in a circular mesa of radius R_o, as a function of time, can be written as

$$\begin{aligned} x_c(t) &= x_\infty\left[1 - exp\left(-\frac{g_0(R_0)}{x_\infty}t\right)\right] \\ &= R_o\left(1 - \sqrt{1 - \frac{2x_\infty\left[1 - exp\left(-\frac{g_0(R_0\rightarrow\infty)}{x_\infty}t\right)\right]}{R_o}}\right). \end{aligned} \tag{4.43}$$

In addition, Langenfelder et al. assert that the ratio between x_c and x_r is equal to the ratio between $g_0(R_o)$ and $g_0(R_o \rightarrow \infty)$. However, since the ratio $\frac{x_c}{x_r}$ is a function of time (since it is a function of x_r) and the g_0 values should be independent of time, there appears to be a flaw in this model.

4.6.2 Critique of Models for the Oxidation of Circular Mesas

As discussed earlier in this chapter (see Section 4.3.1), we do not believe that the steady-state assumption made by Koley et al. is valid for two-dimensional oxidation. The steady-state model for the oxidation of circular mesas predicts that the oxidation rate will decrease with increasing oxidation time [6], the same as for stripes. In fact, the model proposed by Koley et al. predicts an even faster decrease in the oxidation rate for circular mesas, as compared to that for stripes [8]. This is in direct opposition to both our model and the experimental results presented in Chapter 5

As the oxidation proceeds, fewer oxidant molecules are necessary to advance the oxidation front by a differential unit of length, so we would expect an increased oxidation rate. This is a direct effect of the changing size of the oxide-semiconductor interface. The steady-state model fails to account for this effect, having a reaction component identical to that for stripes. This can be shown by rewriting the relationship in Equation 4.39 to separate the three components of the oxidation (transport, reaction, and diffusion):

$$t = \frac{f_{transport}}{h} + \frac{f_{diffusion}}{2D} + \frac{f_{reaction}}{k}, \tag{4.44}$$

where

$$f_{transport} = x\left(2 - \frac{x}{R_0}\right), \tag{4.45}$$

$$f_{diffusion} = \frac{x^2}{2} + R_0 x + (R_0 - x)^2 ln\left(1 - \frac{x}{R_0}\right), \tag{4.46}$$

and

$$f_{reaction} = x. \tag{4.47}$$

In addition, we would expect the expression for the oxidation of a circular mesa of radius a to reduce to that of stripes in the limit $x_o \ll a$. While the steady-state model advanced by Koley et al. does not reduce to the Grove and Deal equation in this limit, we can show that our model for the oxidation of circular mesas does behave as expected. Starting with the reaction component (Equation 4.24) as $\frac{x_o}{a} \rightarrow 0$,

$$t_{reaction} \rightarrow \frac{x_o}{k_R}. \tag{4.48}$$

In order to consider the diffusion component, we rewrite Equation 4.21 as [5]:

$$\begin{aligned} &C(r, t_{diffusion}) = \\ &\quad \frac{C_o a^{1/2}}{r^{1/2}} erfc\left[\frac{a-r}{2(Dt)^{1/2}}\right] + \\ &\quad \frac{C_o(a-r)(Dta)^{1/2}}{4ar^{3/2}} ierfc\left[\frac{a-r}{2(Dt)^{1/2}}\right] + \\ &\quad \frac{C_o(9a^2 - 7r^2 - 2ar)Dt}{32a^{3/2}r^{5/2}} i^2 erfc\left[\frac{a-r}{2(Dt)^{1/2}}\right] + \ldots \end{aligned} \tag{4.49}$$

This expression is valid for $\frac{r}{a}$ not small [5]. The condition $x_o \ll a$ is equivalent to r ≈ a, so this condition is satisfied. In addition, because only the first few terms are listed, $\frac{Dt}{a^2}$ must be less than 0.02 [5]; the limit $x_\circ \ll a$ should be satisfied only for small times, so this condition is also satisfied. As $r \rightarrow a$,

$$C(r, t_{diffusion}) \rightarrow C_\circ erfc\left(\frac{a-r}{2\sqrt{Dt}}\right) = C_\circ\left[1 - erf\left(\frac{x_\circ}{2\sqrt{Dt}}\right)\right]. \tag{4.50}$$

Therefore, both the reaction and diffusion components of our model for circular mesas reduces to the corresponding components of the model for stripes in the limit $x_\circ \ll a$. Althought Langerfeld's model exhibits the expected behavior for $x_\circ \ll a$, it appears to be fundamentally flawed, as discussed in Section 4.6.1.

Perhaps most importantly, our model shows good agreement with the data, as demonstrated in Chapter 5. In contrast, a plot of oxidation length versus oxidation time (Figure 2 of Reference [6]) shows increasing deviation between theory and experiment as the oxidation length increases. This is consistent with our expectation that difference in oxidation rate between stripes and circular mesas should increase as the oxidation proceeds. Both Koley et al. and Langenfelder et al. show plots which cast doubt upon the validity of their models due to the poor agreement between theory and experiment.

Despite the preceeding indications that our model provides a good approximation, there are several improvements that could enhance its ability to describe the oxidation process. The most obvious is inclusion of the gas-phase transfer process. All of the models discussed in this chapter could be improved by including the out-diffusion of reactants, which has yet to be considered, despite experimental evidence that this process may play a role in the oxidation [9]. Also, as mentioned in Chapter 2 and discussed further in Chapter 6, the oxidation process induces strain in the surrounding semiconductor layers, due to the volume contraction of the oxide relative to the original semiconductor layer. This strain may affect the rate at which the oxidation proceeds [7, 10, 11, 12, 13] and should be included in a complete model of the process. In addition, there is evidence that the phase of the oxide changes from the outer edge of the mesa to the oxide-semiconductor interface [14, 15, 16]. Therefore, the diffusion constant may not be constant throughout the oxide, as is assumed in all of the models discussed in this chapter. A full treatment of the oxidation process would involve solving this problem as a boundary value problem, which is complicated even for the case of stripes.

Bibliography

[1] B. Deal and A. Grove, J. Appl. Phys. **36**, 3770 (1965).

[2] M. Ochiai, G. Giudice, H. Temkin, J. Scott, and T. Cockerill, Appl. Phys. Lett. **68**, 1898 (1996).

[3] D. Cohen, discussion, 1997.

[4] J. Crank, *The Mathematics of Diffusion*, 2nd ed. (Oxford University Press, New York, 1975).

[5] H. Carslaw and J. Jaeger, *Conduction of Heat in Solids*, 2nd ed. (Oxford University Press, New York, 1959).

[6] B. Koley, M. Dagenais, R. Jin, J. Pham, G. Simonis, G. McLane, and D. Stone, J. Appl. Phys. **82**, 4586 (1997).

[7] T. Langenfelder, S. Schröder, and H. Grothe, J. Appl. Phys. **82**, 3548 (1997).

[8] B. Koley, M. Dagenais, R. Jin, G. Simonis, J. Pham, G. McLane, F. Johnson, and R. Whaley, Jr., J. Appl. Phys. **84**, 600 (1998).

[9] H. Reese, Y. Chiu, and E. Hu, Appl. Phys. Lett. **73**, 2624 (1998).

[10] S. Guha, F. Agahi, B. Pezeshki, J. Kash, D. Kasker, and N. Bojarczuk, Appl. Phys. Lett. **68**, 906 (1996).

[11] J.-H. Kim, D. Lim, K. Kim, G. Yang, K. Lim, and H. Lee, Appl. Phys. Lett. **69**, 3357 (1996).

[12] T. Yoshikawa, H. Saito, H. Kosaka, Y. Sugimoto, and K. Kasahara, Appl. Phys. Lett. **72**, 2310 (1998).

[13] P. Evans, J. Wierer, and N. Holonyak, Jr., J. Appl. Phys. **84**, 5436 (1998).

[14] R. Twesten, D. Follstaedt, K. Choquette, and R. Schneider, Jr., Appl. Phys. Lett. **69**, 19 (1996).

[15] C. Ashby, J. Sullivan, P. Newcomer, N. Missert, H. Hou, B. Hammons, M. Hafich, and A. Baca, Appl. Phys. Lett. **70**, 2443 (1997).

[16] C. Ashby, J. Sullivan, K. Choquette, K. Geib, and H. Hou, J. Appl. Phys. **82**, 3134 (1997).

Chapter 5 Experimental Results for the Time-Dependence of the Wet Thermal Oxidation Process

5.1 Introduction and Chapter Outline

As stated at the end of Chapter 4, one of the strongest pieces of evidence in support of our model is its agreement with experimental results. In this chapter, data is presented which demonstrates the correspondence between the model, as described in Chapter 4, and our experiments. Section 5.2 contains details of the procedures used to analyze the data presented in the rest of this chapter. Section 5.3 shows experimental results for the oxidation of stripes. Data for the oxidation of circular and square mesas is contained in Sections 5.4 and 5.5, respectively. Conclusions are presented in Section 5.6.

5.2 Data Analysis Procedures

For each oxidation time and temperature, an average of two samples were oxidized in different runs. Each sample contained approximately 30 circles, 30 squares, and 3 stripes; every mesa was measured, although, as discussed in Chapter 3, those with obvious deformities were excluded from further analysis. For circular and square mesas, the oxidation extent for a given mesa shape, oxidation time, and oxidation temperature was obtained by averaging measurements from each sample and combining the sample averages using a weighted average. The Mathematica code in Appendix A.1 was used to generate the weighted averages. Data for stripes was obtained from approximately 10 pictures taken at equal intervals along each mesa. For each stripe, measurements from the corresponding pictures were averaged, and the average oxidation extent for the sample was obtained through a weighted average of the single-stripe averages. As in the case of circular and square mesas, data from different samples with the same oxidation time and temperature was combined using a weighted average.

In order to obtain the constants D and k_R, used in our model and explained in Chapter 4, the data was plotted in Origin. A different set of D and k_R values was obtained for each temperature and mesa shape. Section 5.2.1 describes the fitting procedure for stripes. The fitting procedures for circular and square mesas are contained in Sections 5.2.2 and 5.2.3, respectively. Section 5.2.4 details the procedure used to fit D(T) and k_R(T) to an Arrhenius relationship to obtain activation energies.

5.2.1 Fitting Procedure for Stripes

For stripes, the entire fitting procedure can be performed in Origin, using the nonlinear curve fit tool with

$$y(x) = \frac{x}{P1} + \frac{x^2}{P2}, \tag{5.1}$$

where y represents the oxidation time data, x represents the oxidation length data, P1 is equal to k_R, and P2 is equal to k_D. The fit tool yields values for k_R, k_D, and their respective uncertainties. Equation 4.14 can then be used to obtain the diffusion constant D from the fitted value of k_D.

5.2.2 Fitting Procedure for Circles

The procedure for calculating D and k_R for circular mesas is complicated by our inability to express $t_{diffusion}$ analytically. Therefore, an iterative process is used.

1. Given the experimental oxidation lengths and a chosen diffusion constant D, values of $t_{diffusion}$ are calculated for each length using the Mathematica program in Appendix A.2.

2. The values of $t_{diffusion}$ for each experimental oxidation length are entered into

Origin and used in the following non-linear curve fit equation to generate the best-fit value of k$_R$:

$$z(x) = y + \frac{2ax - x^2}{2aP1}, \tag{5.2}$$

where z represents the oxidation time data, y represents the generated values of t$_{diffusion}$, and x represents the oxidation length data. P1 is equal to k$_R$ and a is the average radius of mesas on the sample. The non-linear curve fit program also generates χ^2 as an indication of the quality of the fit.

3. Steps 1 and 2 are repeated until a diffusion constant is found which generates a minimum χ^2 value.

4. Using the program in Appendix A.3, values for the uncertainties in the calculated values of D and k$_R$ are generated [1].

5.2.3 Fitting Procedure for Squares

We must also use an iterative process to calculate D and k$_R$ for square mesas. Since t$_{reaction}$ can be expressed as

$$t_{reaction}(x_\circ) = \frac{l(x_\circ)}{8ak_R}, \tag{5.3}$$

values of l(x$_\circ$) are calculated once for each set of data (with the program in Appendix A.4) prior to the commencement of the iterative steps below.

1. Given the experimental oxidation lengths and a chosen diffusion constant D, values of t$_{diffusion}$ are calculated for each length using the Mathematica program in Appendix A.5.

2. The values of t$_{diffusion}$ and l(x$_\circ$) for each experimental oxidation length are entered into Origin and used in the following non-linear curve fit equation to generate the best-fit value of k$_R$:

$$z(x) = y + \frac{x}{8aP1}, \tag{5.4}$$

where z represents the oxidation time data, y represents the generated values of $t_{diffusion}$, and x represents the values of $l(x_{\circ})$ generated for each experimental oxidation length. P1 is equal to k_R, and 2a is the average side-length for mesas on the sample. The non-linear curve fit program also generates χ^2 as an indication of the quality of the fit.

3. Steps 1 and 2 are repeated until a diffusion constant is found which generates the minimum χ^2 value.

4. Using the program in Appendix A.6, uncertainties in the calculated values of D and k_R are generated [1].

5.2.4 Procedure for Obtaining Activation Energies

In order to obtain the activation energies of D and k_R for each mesa shape, the calculated values of these constants at each temperature are fit to an Arrhenius relationship, as given in Equation 2.3. A linear fit is used:

$$y(x) = P1 + x(P2), \tag{5.5}$$

where y is equal to the natural logarithm (ln) of D or k_R, x is the inverse of the oxidation temperature (in K^{-1}), and P2 is equal to the activation energy divided by Boltzmann's constant (8.62 x 10^{-5} eV·K^{-1}).

5.3 Data for the Oxidation of Stripes

Data obtained for the oxidation of stripes at 375, 425, and 475°C is shown in Figures 5.1 - 5.3. Values for the diffusion constant D and the reaction constant k_R used to obtain the fits to our model are shown in Table 5.1. Figures 5.1 - 5.3 also show the contributions of the reaction and diffusion components to the oxidation of stripes. It can be seen that, for all three temperatures, the oxidation is reaction-rate-limited; however, the stripes are not completely oxidized. Assuming that the constants will

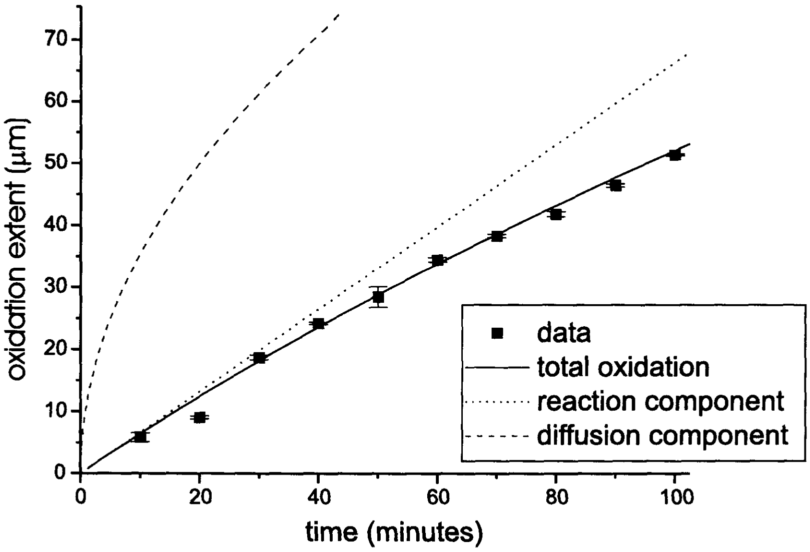

Figure 5.1: This plot shows data obtained for the oxidation of stripes at 375°C. The black (solid) curve shows the fit obtained for our model with $k_R = 0.6644$ μm/min and D = 125.739 μm^2/min. The magenta (dotted) and blue (dashed) curves show the reaction and diffusion components of the oxidation.

not change for additional oxidation, we can calculate x_t, the oxidation length at which the reaction and diffusion curves will cross:

$$x_t = \frac{k_D}{k_R}. \tag{5.6}$$

Using the experimentally-determined values of k_D and k_R for 375°C and 475°C, we predict that the transition between reaction-rate- and diffusion-limited oxidation will occur after approximately 100 μm of oxide has been formed at 375°C and after approximately 200 μm of oxide has been formed at 475°C. In both cases, this is farther than the 75 μm required to completely oxidize our 150 μm-wide stripes. Although it is difficult to draw a meaningful conclusion with only these two data points, it would appear that the transition occurs at decreasing oxide extent with increasing temperature.

Using the values of k_R and D in Table 5.1, we can create an Arrhenius plot for each constant to determine its temperature-dependence. These plots are shown in

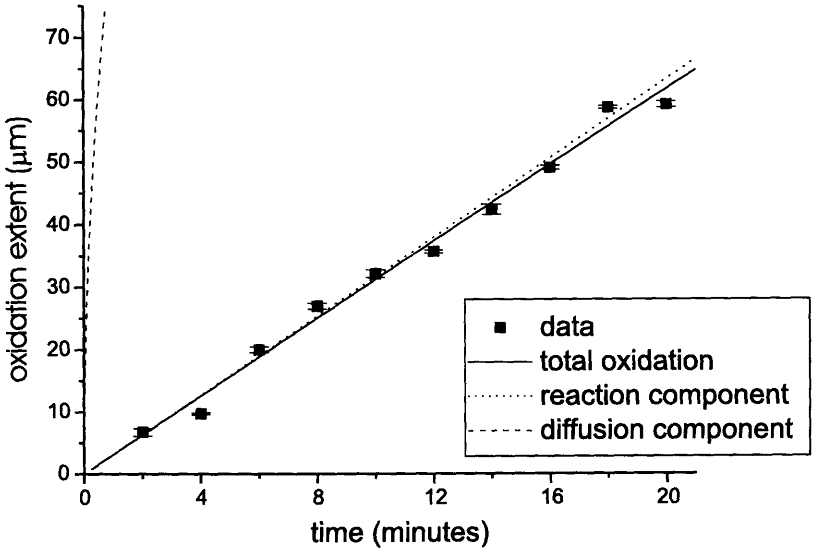

Figure 5.2: This plot shows data obtained for the oxidation of stripes at 425°C. The black (solid) curve shows the fit obtained for our model with $k_R = 3.15971$ μm/min and $D = 7431.98$ μm^2/min. The magenta (dotted) and blue (dashed) curves show the reaction and diffusion components of the oxidation.

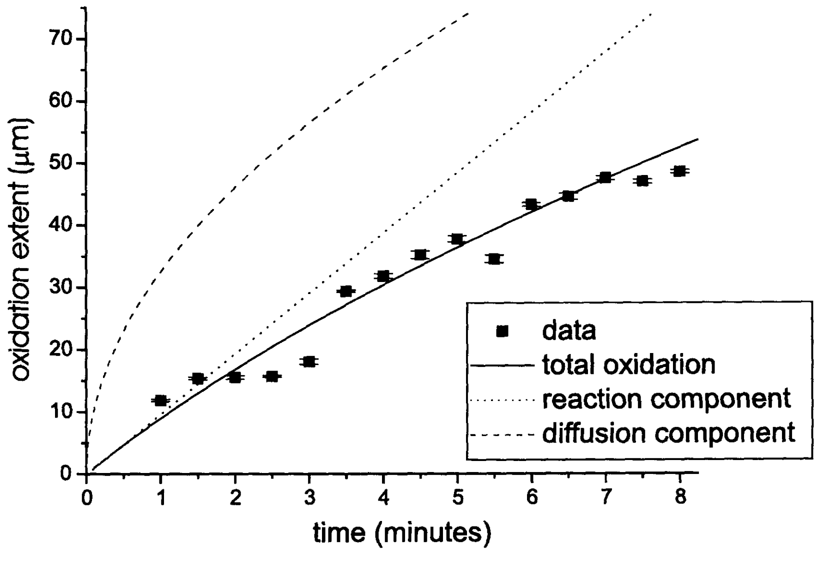

Figure 5.3: This plot shows data obtained for the oxidation of stripes at 475°C. The black (solid) curve shows the fit obtained for our model with $k_R = 9.68588$ μm/min and $D = 1064$ μm^2/min. The magenta (dotted) and blue (dashed) curves show the reaction and diffusion components of the oxidation.

Table 5.1: Fitted values of k_R and D for the oxidation of stripes.

temperature (°C)	k_R (μm/min)	D (μm^2/min)
375	0.66 ± 0.04	130 ± 30
425	3.2 ± 0.2	7000 ± 20000
475	10 ± 2	1100 ± 400

Table 5.2: Fitted values of k_R and D for the oxidation of circular mesas.

temperature (°C)	k_R (μm/min)	D (μm^2/min)
375	1.27 ± 0.02	16.41 ± 0.06
425	6.7 ± 0.5	85 ± 3
475	20000 ± 800000	143 ± 7

Figure 5.4. From these plots we obtain activation energies of 1.16 ± 0.09 eV and 0.9 ± 0.2 eV for k_R and D, respectively.

5.4 Data for the Oxidation of Circular Mesas

Data obtained for the oxidation of circular mesas at 375, 425, and 475°C is shown in Figures 5.5 - 5.7. Values for the diffusion constant D and the reaction constant k_R used to obtain the fits to our model are shown in Table 5.2. Figures 5.5 - 5.7 also show the contributions of the reaction and diffusion components to the oxidation of circular mesas. It can be seen that the oxidation length corresponding to the transition from a reaction-rate- to a diffusion-limited process decreases as the temperature increases. This is in agreement with the results obtained for stripes, although the transition occurs much earlier for the oxidation of circular mesas – tens of microns for circular mesas compared to hundreds of microns for stripes.

Using the values of D and k_R in Table 5.2, we can create an Arrhenius plot for each constant to determine its temperature-dependence. These plots are shown in Figure 5.8. From these plots we obtain activation energies of 1.30 ± 0.01 eV and 1.0 ± 0.2 eV for k_R and D, respectively.

As stated in Chapter 3, measurements for mesas with obvious deformities were removed from our calculations. Therefore, Figures 5.5 - 5.7 contain data only for

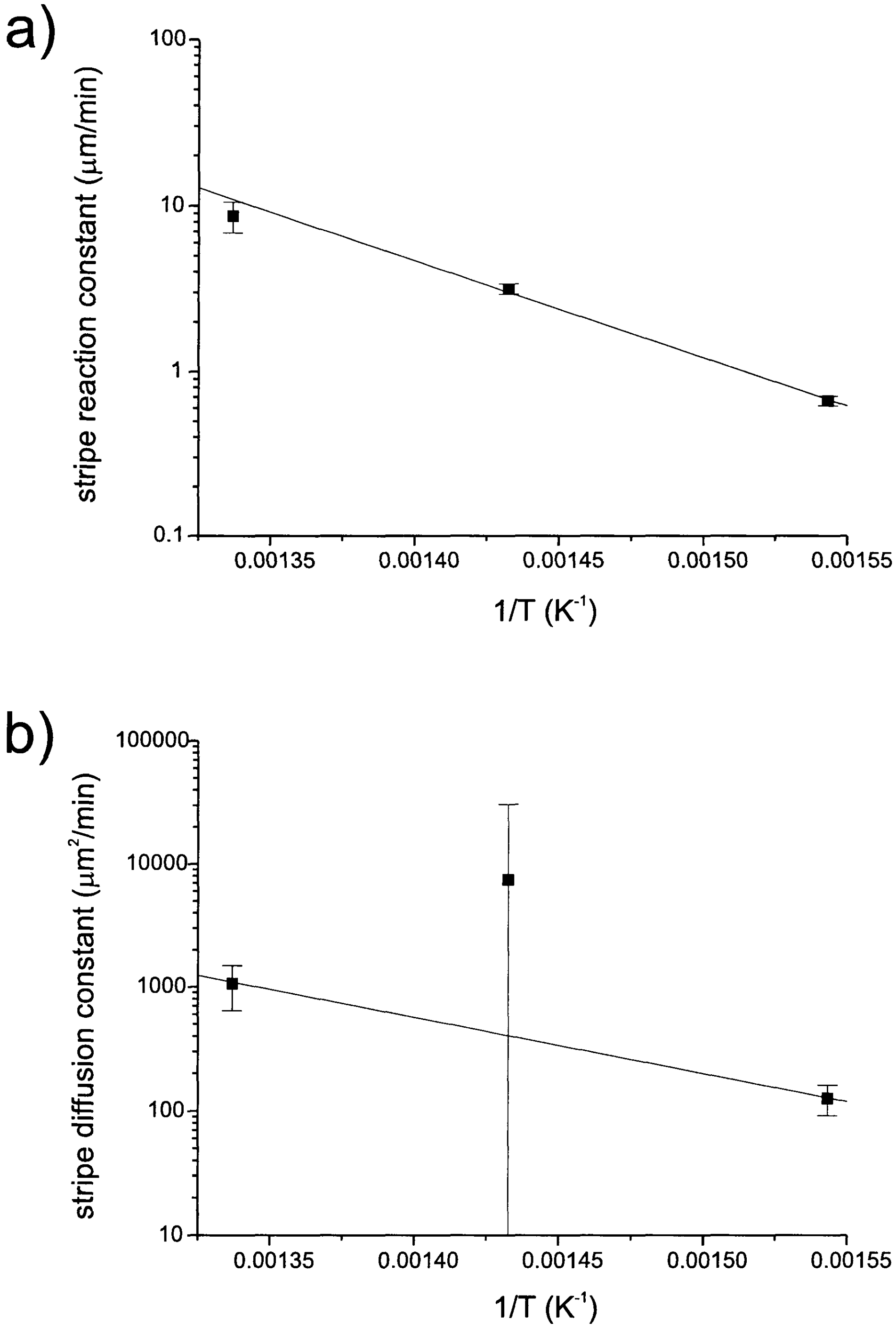

Figure 5.4: (a) This plot shows the temperature-dependence of the reaction constant k_R for the oxidation of stripes. The line represents a fit to the Arrhenius relationship with an activation energy $E_a = 1.16149$ eV. (b) This plot shows the temperature-dependence of the diffusion constant D for the oxidation of stripes. The line represents a fit to the Arrhenius relationship with an activation energy $E_a = 0.89859$ eV.

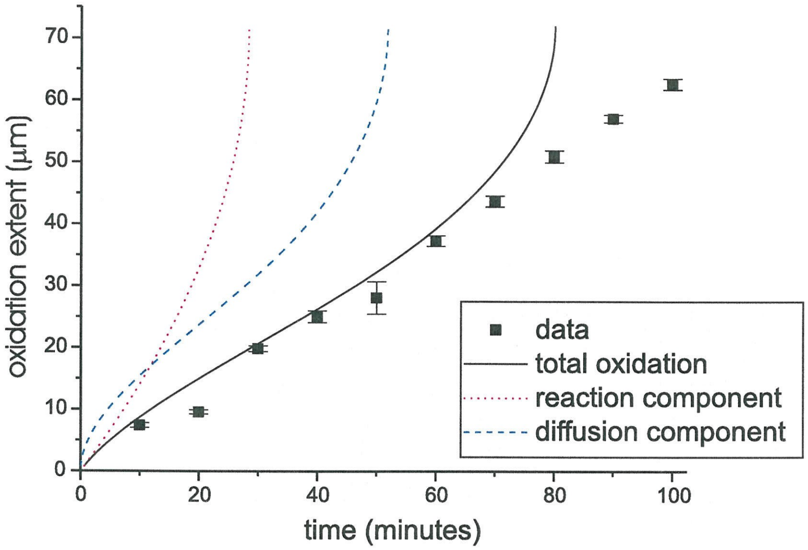

Figure 5.5: This plot shows data obtained for the oxidation of circular mesas at 375°C. The black (solid) curve shows the fit obtained for our model with $k_R = 1.27184\ \mu\text{m/min}$ and $D = 16.4054\ \mu\text{m}^2/\text{min}$. The magenta (dotted) and blue (dashed) curves show the reaction and diffusion components of the oxidation.

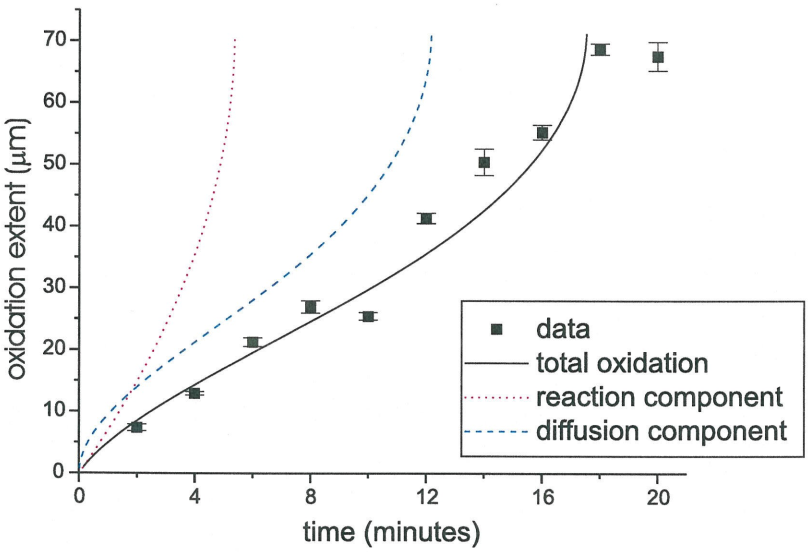

Figure 5.6: This plot shows data obtained for the oxidation of circular mesas at 425°C. The black (solid) curve shows the fit obtained for our model with $k_R = 6.69367\ \mu\text{m/min}$ and $D = 85.0604\ \mu\text{m}^2/\text{min}$. The magenta (dotted) and blue (dashed) curves show the reaction and diffusion components of the oxidation.

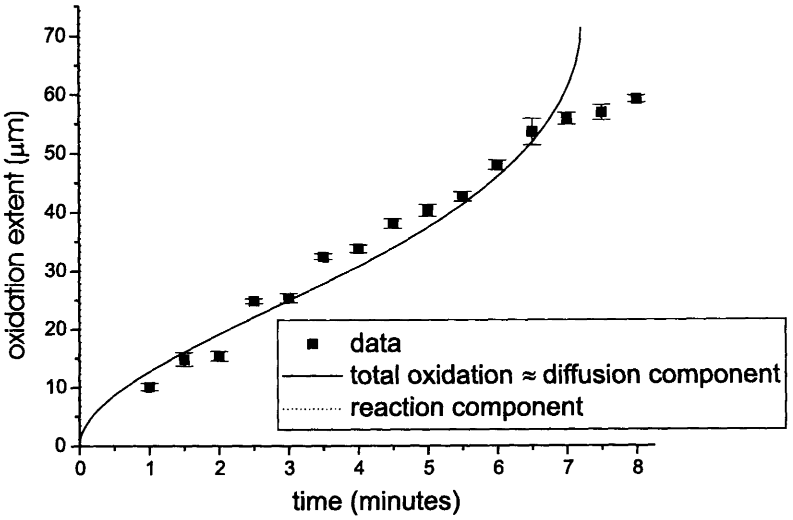

Figure 5.7: This plot shows data obtained for the oxidation of circular mesas at 475°C. The black (solid) curve shows the fit obtained for our model with $k_R = 20477.4$ μm/min and D = 142.914 μm^2/min. The magenta (dotted) curve shows the reaction component of the oxidation. Because of the relatively large value of k_R, the total oxidation curve is approximately equal to the diffusion component.

those mesas which passed our visual inspection. Unfortunately, these results show less agreement with the general form of our model than the results obtained by including all mesas in the calculations. For comparison, Figures 5.9 - 5.11 show the results obtained with data from all mesas. An important feature of our model is the increased oxidation rate as the oxidation nears completion. A major difference between the data shown in Figures 5.9 - 5.11 and that in Figures 5.5 - 5.7 is the agreement of the former with this aspect of our model.

It may be that a disproportionate number of mesas with large oxide extents were discarded. One of the criteria used to discard mesas from further calculations was asymmetry in the aperture or mesa. However, as shown in Section 6.5.3, variations do exist in the oxidation rates in different crystallographic directions. This would lead to asymmetry which would not be noticeable for small oxide extents but which would have an increasing effect on the appearance of the mesa as the oxidation nears completion. Therefore, this procedure may prevent the measurement of large oxidation extents.

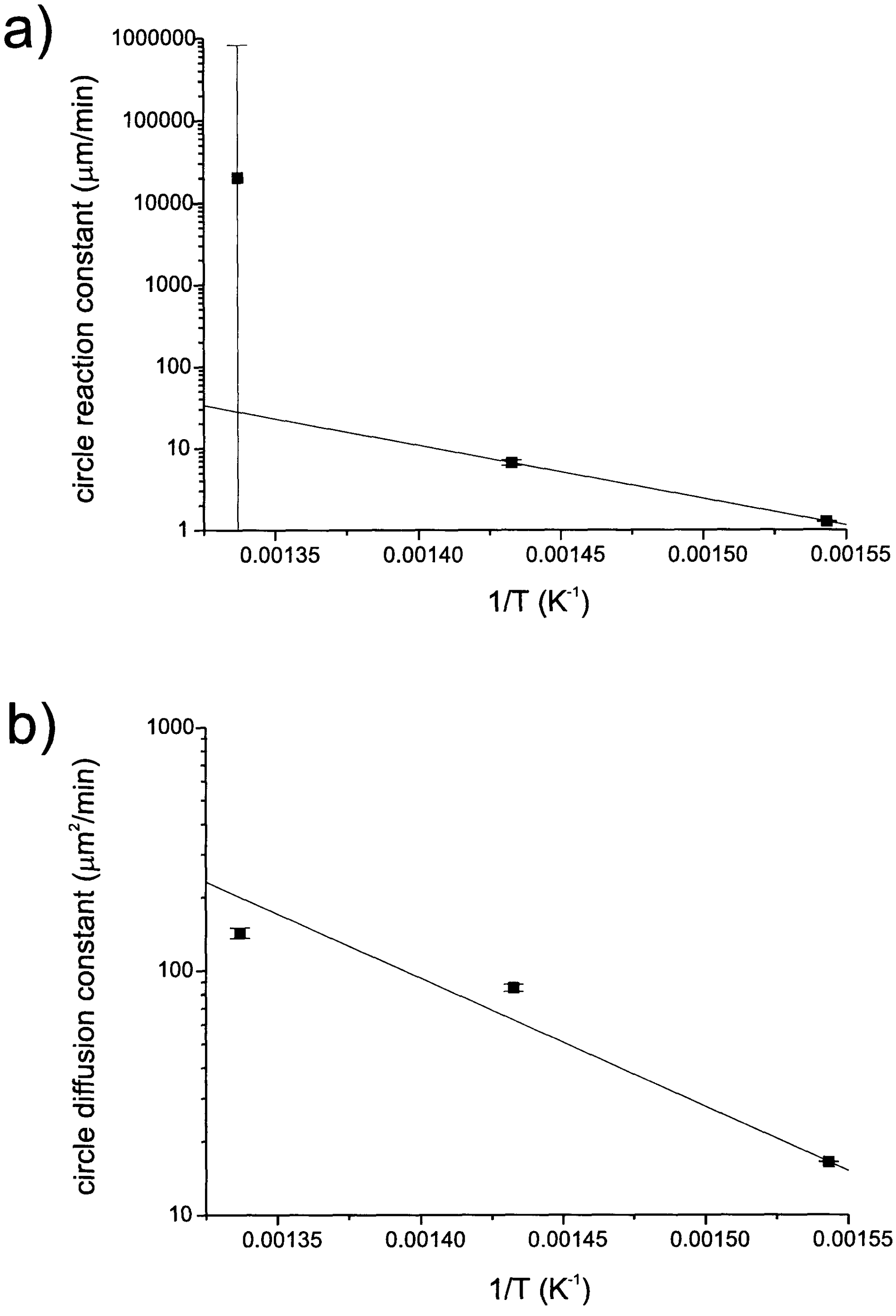

Figure 5.8: (a) This plot shows the temperature-dependence of the reaction constant k_R for the oxidation of circular mesas. The line represents a fit to the Arrhenius relationship with an activation energy $E_a = 1.295$ eV. (b) This plot shows the temperature-dependence of the diffusion constant D for the oxidation of circular mesas. The line represents a fit to the Arrhenius relationship with an activation energy $E_a = 1.04501$ eV.

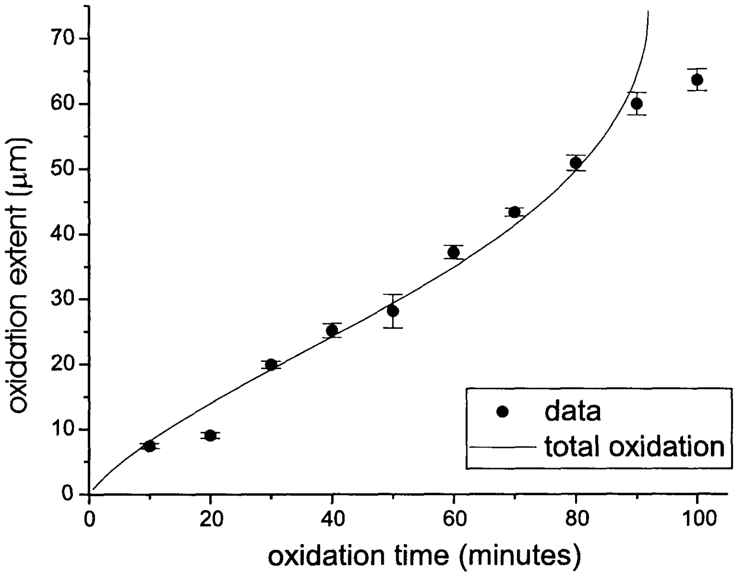

Figure 5.9: This plot shows data obtained for the oxidation of circular mesas at 375°C, including measurements from all mesas. The curve shows the fit obtained for our model with k_R =1.17223 μm/min and D = 17.1125 μm^2/min.

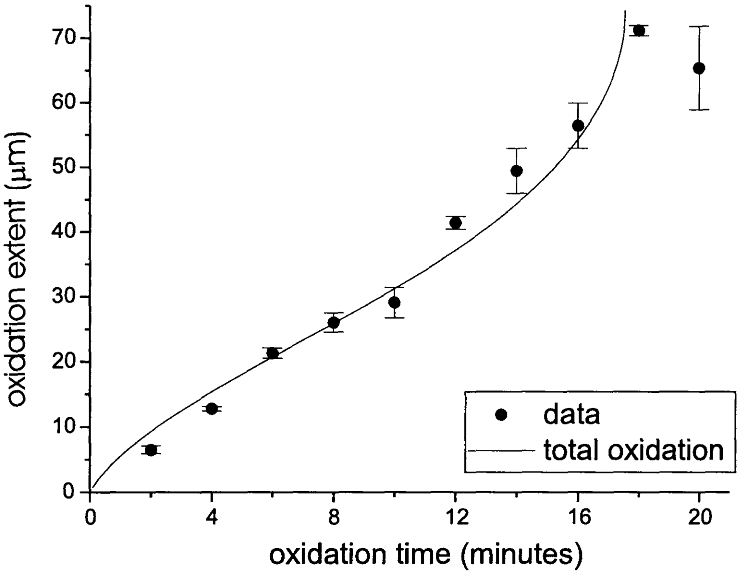

Figure 5.10: This plot shows data obtained for the oxidation of circular mesas at 425°C, including measurements from all mesas. The curve shows the fit obtained for our model with k_R = 8.43386 μm/min and D = 78.071 μm^2/min.

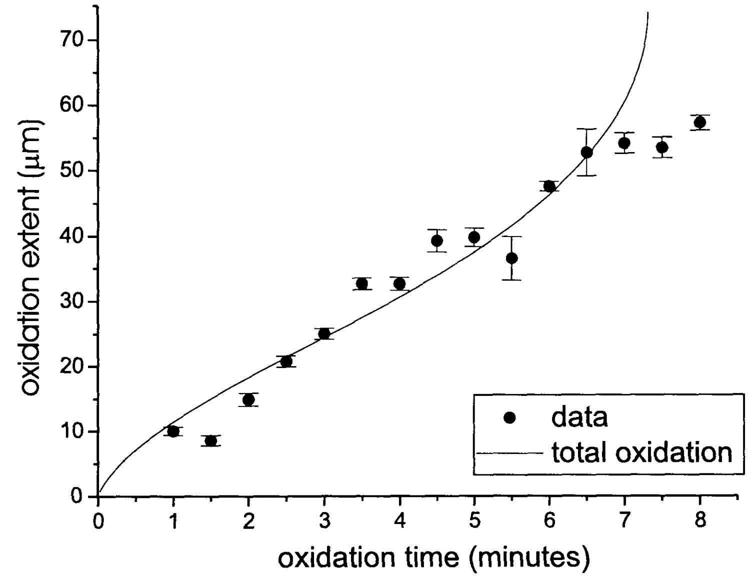

Figure 5.11: This plot shows data obtained for the oxidation of circular mesas at 475°C, including measurements from all mesas. The curve shows the fit obtained for our model with k_R = 29.34596 μm/min and D = 170.528 μm^2/min.

In addition, it is difficult to obtain reliable data for oxide extents close to the radius of the mesa. Because the slope of the oxidation length vs. oxidation time curve is so steep at the end, any small variations in oxidation conditions drastically affect the measured oxidation length. As illustrated in Figure 5.12, the discrepancy between data points obtained from different oxidation runs generally increases with increasing time, leading to more ambiguous results for longer times and thus larger oxidation extents.

5.5 Data for the Oxidation of Square Mesas

Data obtained for the oxidation of square mesas at 375, 425, and 475°C is shown in Figures 5.13 - 5.15. Values for the diffusion constant D and the reaction constant k_R used to obtain the fits to our model are shown in Table 5.3. Figures 5.13 - 5.15 also show the contributions of the reaction and diffusion components to the oxidation of square mesas. There is no apparent correlation between the relative importance of reaction and diffusion components with temperature.

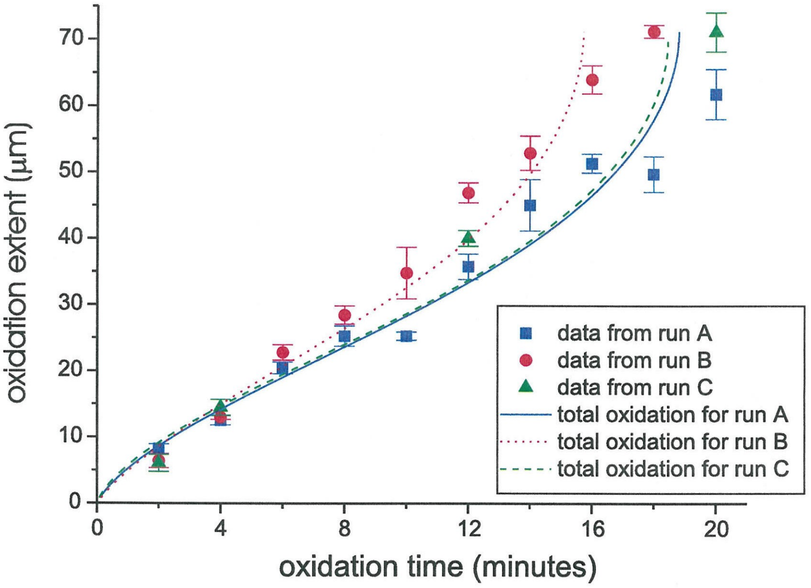

Figure 5.12: This plot shows the data obtained for the oxidation of circular mesas at 425°C in three different runs. It can be seen that the difference between the measurements increases as the oxidation proceeds.

Table 5.3: Fitted values of k_R and D for the oxidation of square mesas.

temperature (°C)	k_R (μm/min)	D (μm^2/min)
375	5.02 ± 0.03	70 ± 2
425	36 ± 1	190 ± 10
475	52 ± 2	3000 ± 2000

Using the values of D and k_R in Table 5.3, we can create an Arrhenius plot for each constant to determine its temperature-dependence. These plots are shown in Figure 5.16. From these plots we obtain activation energies of 1.2 ± 0.3 eV and 0.8 ± 0.1 eV for k_R and D, respectively.

5.6 Conclusions

As shown in the preceding sections, our model fits quite well with the data obtained in our experiments. Some discrepancy was observed between theory and experiment results for circular mesas which were almost completely oxidized. Because of the importance of this regime in differentiating our model from both oxidation in one-

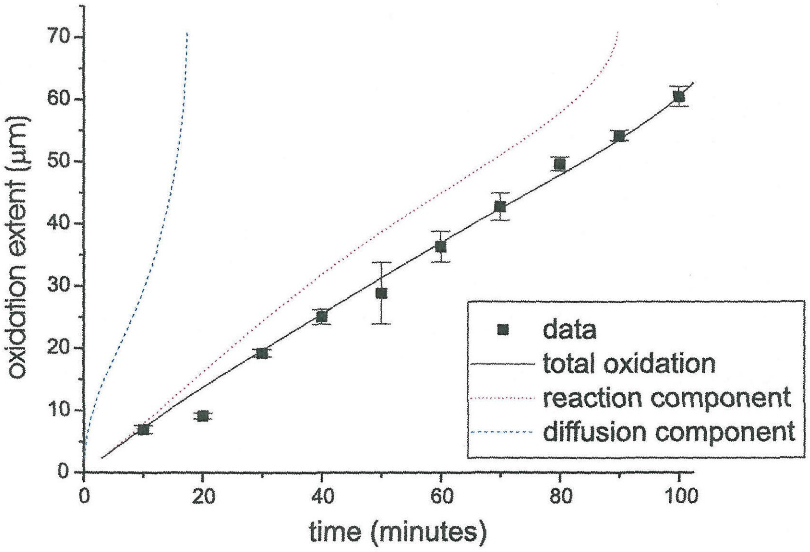

Figure 5.13: This plot shows data obtained for the oxidation of square mesas at 375°C. The black (solid) curve shows the fit obtained for our model with $k_R = 5.02225\ \mu m/min$ and $D = 70.5688\ \mu m^2/min$. The magenta (dotted) and blue (dashed) curves show the reaction and diffusion components of the oxidation.

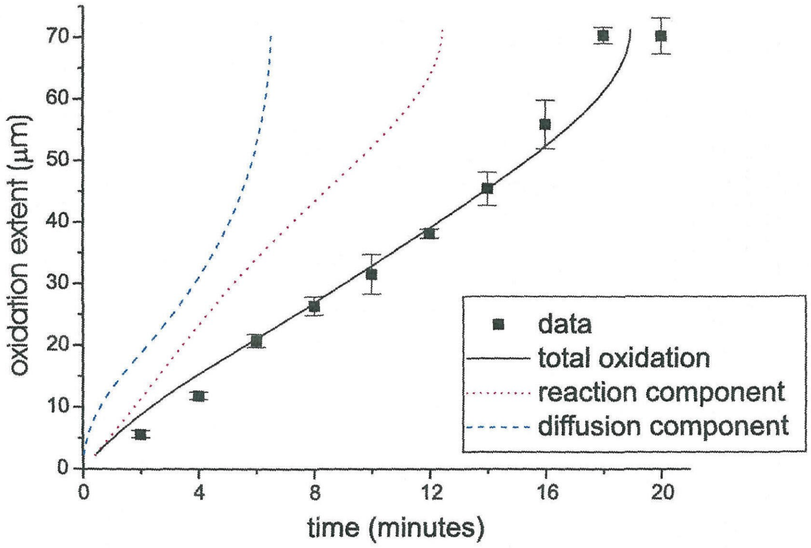

Figure 5.14: This plot shows data obtained for the oxidation of square mesas at 425°C. The black (solid) curve shows the fit obtained for our model with $k_R = 36.2423\ \mu m/min$ and $D = 187.025\ \mu m^2/min$. The magenta (dotted) and blue (dashed) curves show the reaction and diffusion components of the oxidation.

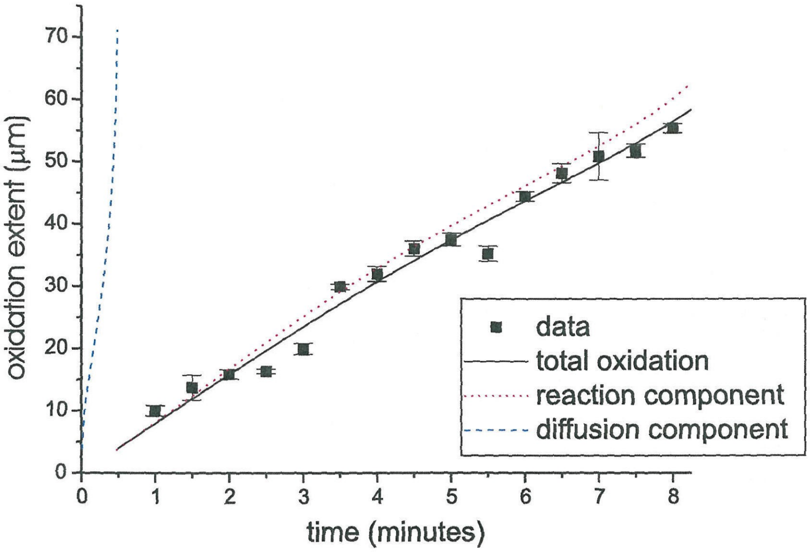

Figure 5.15: This plot shows data obtained for the oxidation of square mesas at 475°C. The black (solid) curve shows the fit obtained for our model with $k_R = 52.1702$ μm/min and D = 2532.93 μm^2/min. The magenta (dotted) and blue (dashed) curves show the reaction and diffusion components of the oxidation.

dimension and other models for the oxidation of circular mesas, some explanations were explored in Section 5.4. We believe that our method for discarding deformed mesas disproportionately removed the most oxidized mesas. In addition, there is greater variation in the measurements as the oxidation proceeds, due to the rapid change in the oxidation rate at the end of the process. Both of these factors may explain the results reported in Section 5.4.

However, as stated in Section 4.6.2, there are also two potential shortcomings of our model: (1) it does not include the gas-phase transfer process and (2) it does not include the out-diffusion of oxidation products. Either of these factors could account for a slightly slower increase in the oxidation rate than our model predicts. It is clear that an infinite oxidation rate, as predicted at the center of the mesa, is not physically possible, so it is reasonable to assume that at some point towards the end of the oxidation, our model predicts a longer oxidation extent than is actually realized experimentally. However, because of the difficulty in measuring the oxidation extent in this region, we cannot determine precisely where this transition occurs.

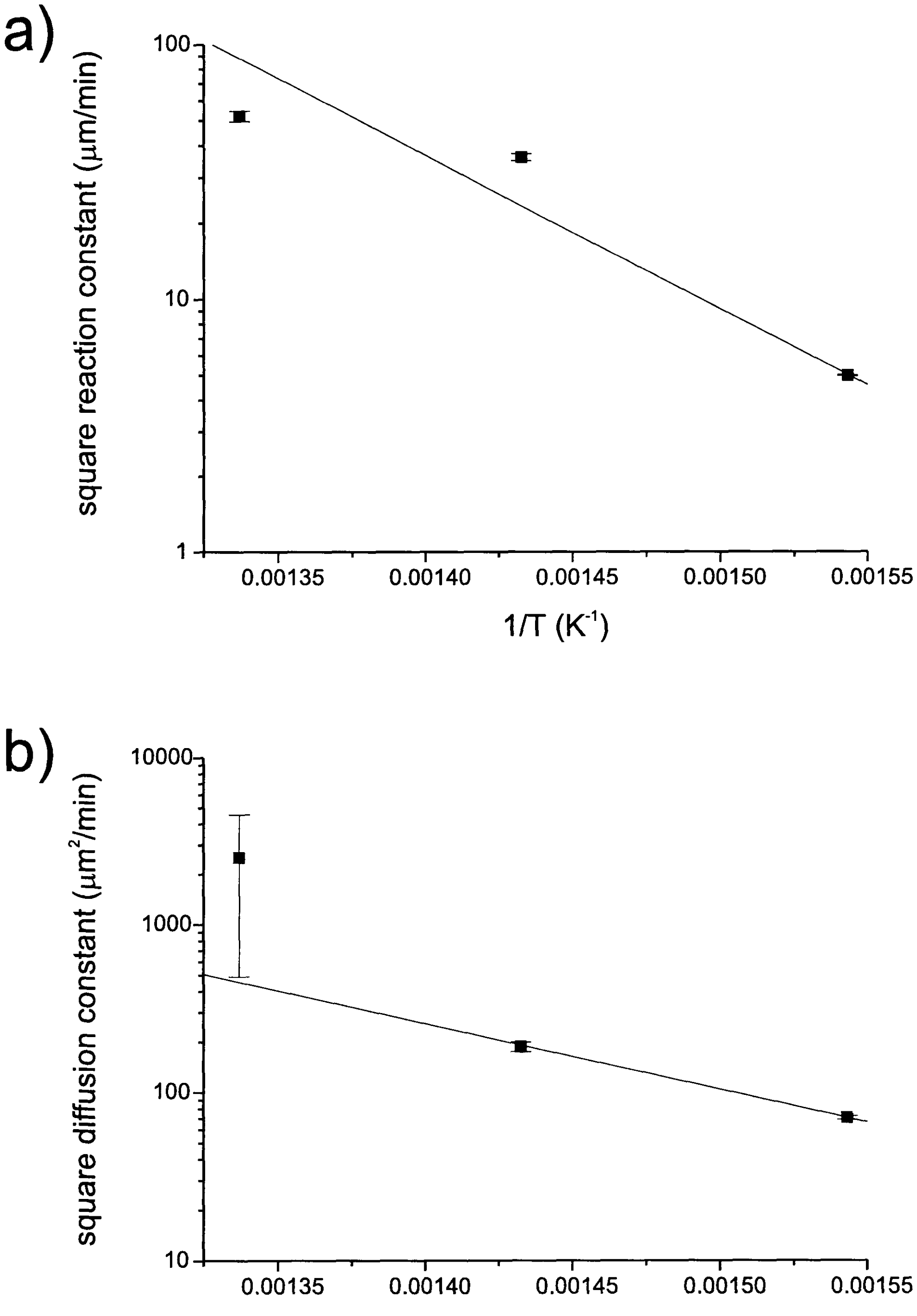

Figure 5.16: (a) This plot shows the temperature-dependence of the reaction constant k_R for the oxidation of circular mesas. The line represents a fit to the Arrhenius relationship with an activation energy $E_a = 1.19522$ eV. (b) This plot shows the temperature-dependence of the diffusion constant D for the oxidation of circular mesas. The line represents a fit to the Arrhenius relationship with an activation energy $E_a = 0.77788$ eV.

Table 5.4: Activation energies for k_R and D.

mesa geometry	E_{k_R} (eV)	E_D (eV)
stripe	1.16 ± 0.09	0.9 ± 0.2
circle	1.30 ± 0.01	1.0 ± 0.2
square	1.2 ± 0.3	0.8 ± 0.1

In addition to the generally good fit between our model and our data, there is, within experimental uncertainty, little difference between the activation energies for different mesa geometries, as shown in Table 5.4. We would expect this result since the temperature-dependence of the processes involved in the oxidation should not be influenced by the shape of the oxidizing mesa. Averaging yields overall activation energies of 1.22 ± 0.07 eV and 0.9 ± 0.1 eV for the reaction and diffusion components, respectively. These values are similar to those obtained by Ochiai et al. for the oxidation of stripes (1.6 and 0.8 eV for reaction and diffusion, respectively) [2]. Since no experimental uncertainty is given for these values, an exact comparison with our results cannot be obtained.

The higher activation energy of the reaction component, as compared to that of the diffusion component, is consistent with our observation that the transition between reaction- and diffusion-limited oxidation occurs at smaller oxide extents as the temperature of oxidation increases. The reaction rate increases faster with temperature than the diffusion rate [2]. Therefore, as the temperature increases, the point at which the reaction process overtakes the diffusion process will occur after less and less oxide has been formed.

Just as we do not expect the temperature-dependence of the reaction and diffusion constants to be a function of geometry, the constants themselves should also be independent of the shape of the oxidizing mesa. However, while similar activation energies are observed for oxidation in stripes, circles, and squares, there is some variation in the constants k_R and D for these different shapes. Tables 5.5 and 5.6 show the values of k_R and D for all three mesa shapes, calculated from the Arrhenius relationship (Equation 2.3) with the activation energies for each mesa type. It appears that the constants for a given shape are related to those of the other shapes

Table 5.5: This table shows the values of the reaction-rate constant for stripe, circles, and squares, calculated from the Arrhenius relationship for each geometry.

temperature (°C)	k_R^{stripe} (μm/min)	k_R^{circle} (μm/min)	k_R^{square} (μm/min)
375	0.71	1.33	5.29
425	3.12	6.97	24.30
475	10.48	26.93	84.65

Table 5.6: This table shows the values of the diffusion constant for stripe, circles, and squares, calculated from the Arrhenius relationship for each geometry.

temperature (°C)	D^{stripe} (μm^2/min)	D^{circle} (μm^2/min)	D^{square} (μm^2/min)
375	131	17	73
425	414	65	196
475	1057	193	441

by relatively constant factors: $k_R^{circle} \approx 2k_R^{stripe}$, $k_R^{square} \approx 8k_R^{stripe}$, $D^{circle} \approx \frac{D^{stripe}}{6.5}$, and $D^{square} \approx \frac{D^{stripe}}{2}$. This, coupled with the consistency of the activation energies, leads us to believe that numerical factors in the definitions of the constants may be responsible for the apparent discrepancy between values of the reaction and diffusion constants for the three shapes. This conclusion is particularly tempting since the factors 2 and 8 appear in both the relationships above and in the expressions for k_R^{circle} and k_R^{square}, respectively. Even though the absolute values obtained for the constants k_R and D do not show agreement between the different geometries as we would expect, it still seems that the functional form of our model is correct and that the discrepancy could arise from numerical factors in the definitions of these constants. However, this prevents us from comparing the values obtained for k_R and D with those obtained by other researchers for the oxidation of stripes.

Bibliography

[1] P. Bevington and D. Robinson, *Data Reduction and Error Analysis for the Physical Sciences*, 2nd ed. (McGraw-Hill, Inc., New York, 1992).

[2] M. Ochiai, G. Giudice, H. Temkin, J. Scott, and T. Cockerill, Appl. Phys. Lett. **68**, 1898 (1996).

Chapter 6 Strain in Square and Circular Mesas

6.1 Introduction and Chapter Outline

This chapter explores an additional effect of geometry on wet thermally oxidized mesas. As in the previous chapters, we have focused upon mesa shapes with direct relevance to VCSEL fabrication. The studies described in this chapter were prompted by the observation of drumhead-like patterns in circular and square mesas with significant oxidation extent. We hypothesize that these patterns are related to strain induced in the semiconductor crystal by the oxidation process and that their orientation is indicative of crystallographic preferences in the oxidation process itself. Because of our interest in the orientation of the drumhead patterns, special sample preparation techiques were required. These are detailed in Section 6.2. The drumhead patterns and their orientation with respect to the crystallographic axes of the semiconductor are documented in Section 6.3. In Section 6.4, micro-Raman spectroscopy results are described which show evidence for a correlation between the drumhead patterns and strain induced in the GaAs cap layer. Section 6.5 contains a proposed explanation for the orientation of the drumhead patterns which is based upon a study of the oxidation rate in various crystallographic directions. Finally, conclusions are presented in Section 6.6.

6.2 Sample Preparation for Direction-Dependent Studies

In addition to the experimental procedures detailed in Chapter 3, an extra step was necessary to preserve knowledge of the crystal orientation once the wafer had been

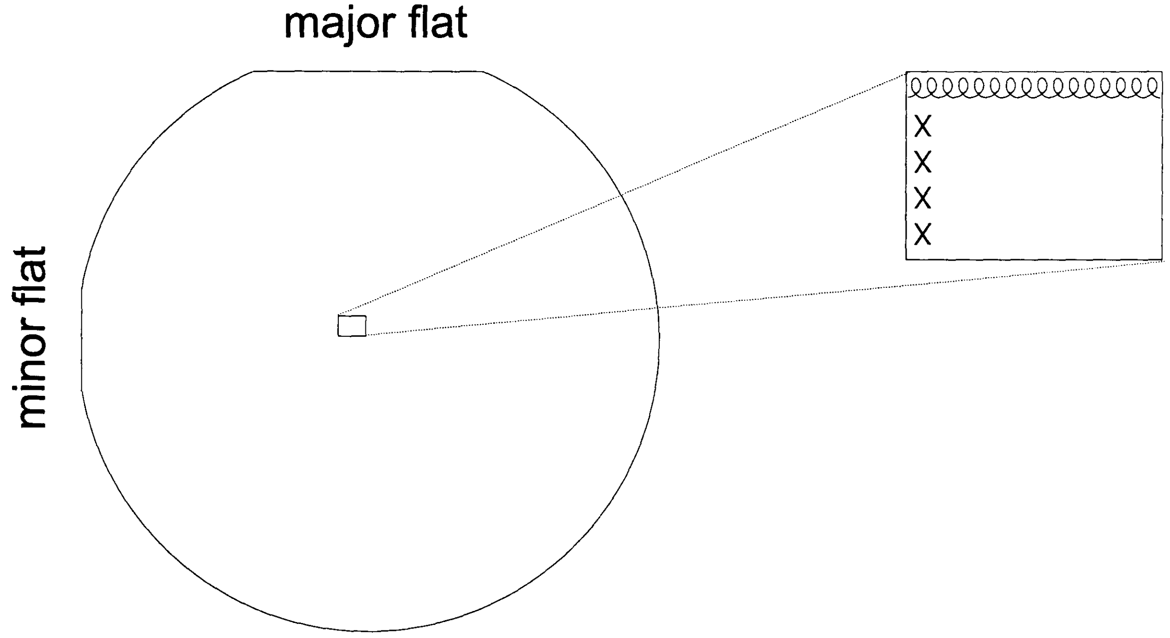

Figure 6.1: Illustration of the technique for marking the directions of major and minor flats on small pieces of a wafer.

cleaved into small pieces for processing and oxidation. Starting with an intact wafer, each cleaved piece was marked with symbols along the edges corresponding to the major and minor flats, as shown in Figure 6.1. This represents a redundancy since either the edge aligned with the major flat or that aligned with the minor flat could be used to determine the other. However, this procedure guaranteed that accidental cleaving would not render a sample unusable due to loss of information about its crystallographic axes.

Four samples were used in this study, each with a different orientation of the mesas with respect to the major and minor flats of the semiconductor. The orientation of each sample is illustrated in Figure 6.2. As shown in Figure 6.3, the major flat corresponds to the (011) plane, while the minor flat corresponds to the $(0\bar{1}1)$ plane of the wafer. The stripes in Samples A, B, C, and D are aligned with the (011), $(0\bar{1}1)$, (001), and (010) planes, respectively. In Samples A and B, the sides of the square mesas are aligned with the $\{011\}$ planes. The sides of square mesas in Samples C and D are aligned with the $\{010\}$ planes.

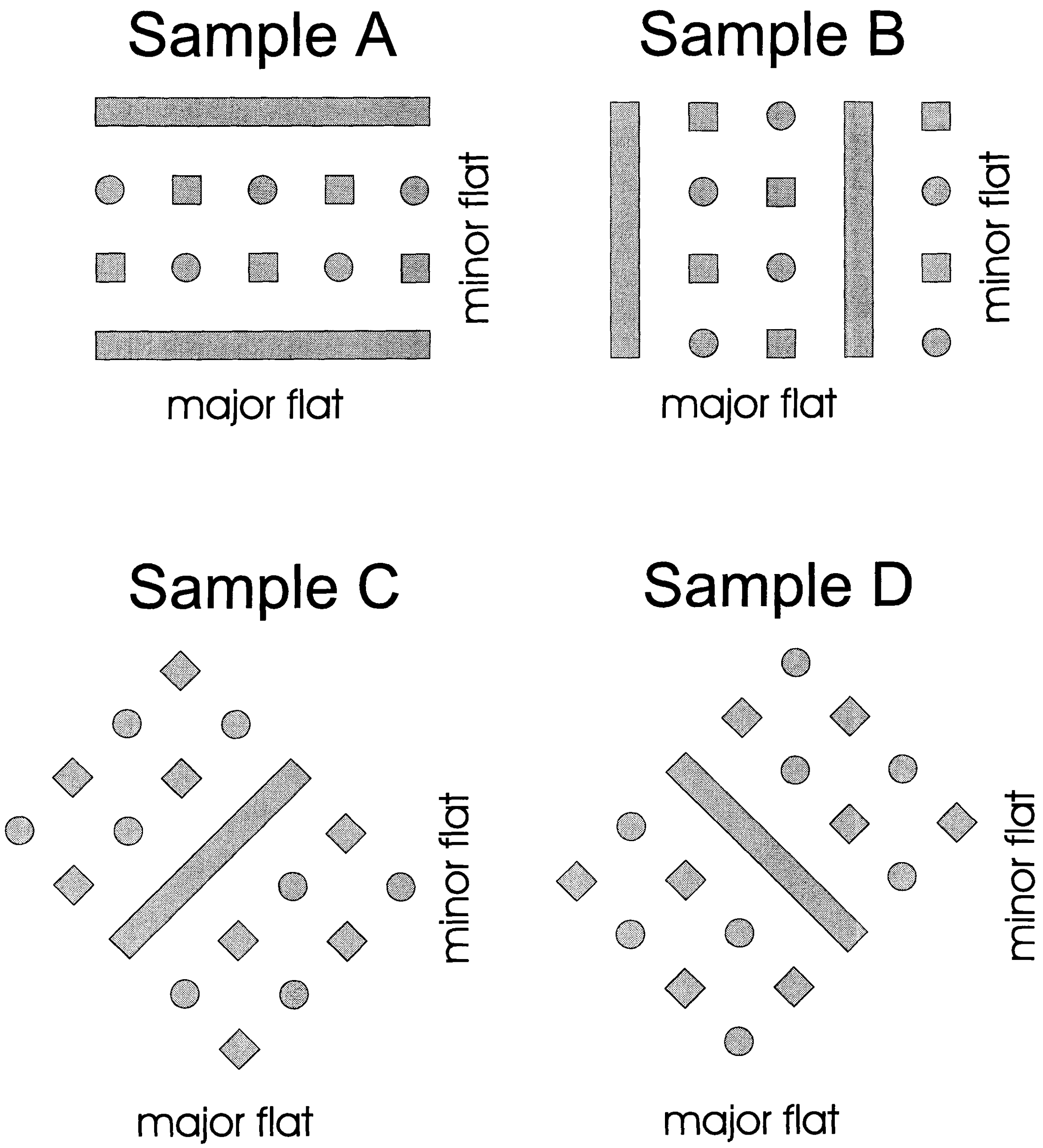

Figure 6.2: This figure shows the orientation of mesas with respect to major and minor flats of the wafer in Samples A - D.

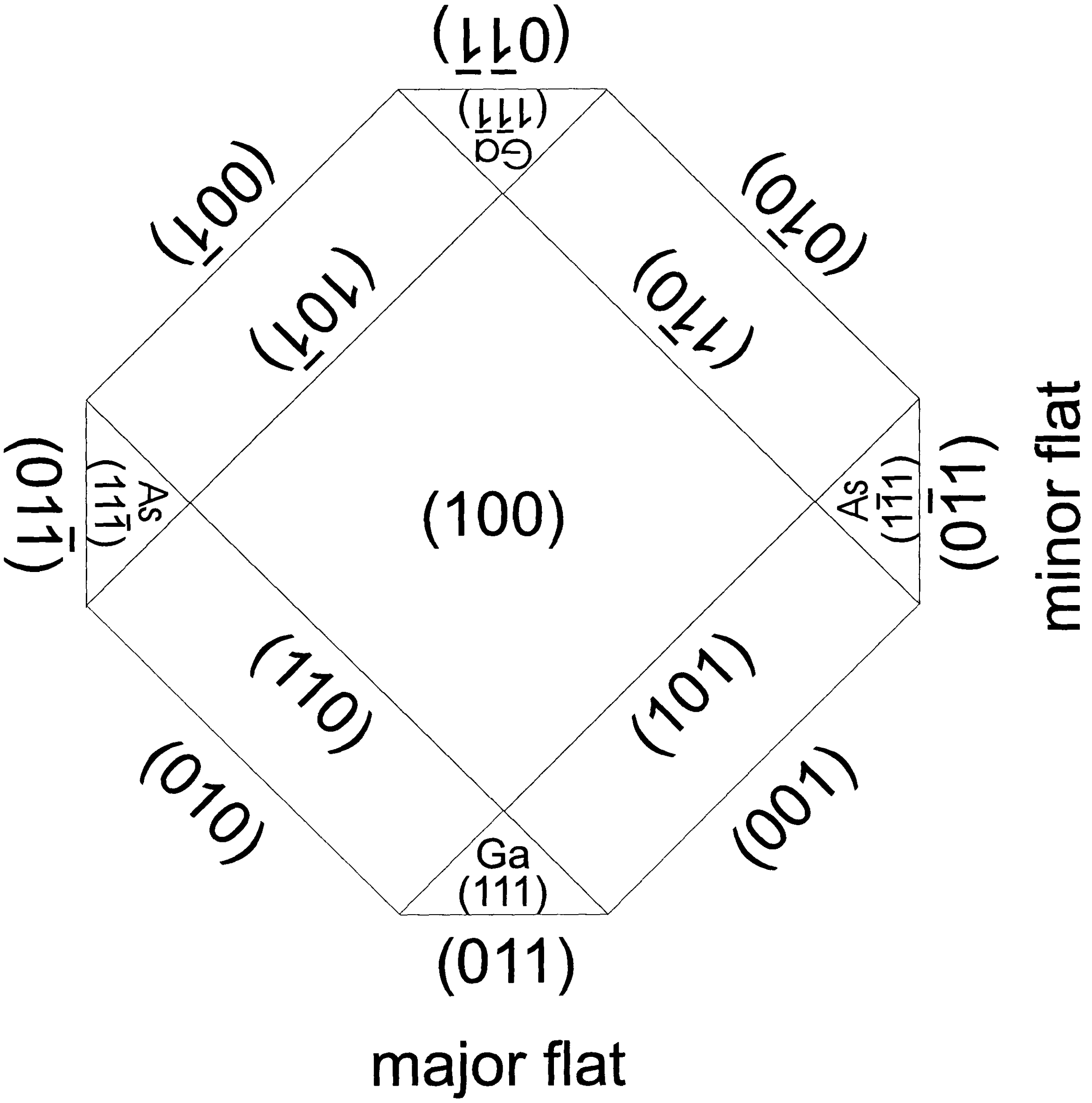

Figure 6.3: Illustration of crystallographic axes in a (100) GaAs wafer.

6.3 Observed Drumhead Patterns

In order to completely oxidize both the square and circular mesas, each sample was oxidized at 425°C for approximately 25 minutes under the conditions described in Chapter 3. Optical microscope pictures reveal drumhead patterns in both circular and square mesas. These appear as a green pattern on a pink background. For mesas which are only partially oxidized, the color that the oxide appears under the optical microscope is generally indicative of the GaAs cap thickness. Samples with 150-nm, 100-nm, and 50-nm GaAs caps have oxide layers which appear green, yellow, and pink, respectively. However, as discussed later in this chapter, another explanation is required for the colors in the drumhead patterns shown in this section.

A typical circular mesa is shown in Figure 6.4. In all four samples, the drumhead patterns are oriented parallel to the minor flat, i.e., along the [011] direction. For square mesas in Samples A and B, such as the one shown in Figure 6.5, the drumhead patterns are also oriented parallel to the minor flat. Figure 6.6 shows a square mesa representative of those in Samples C and D. The pattern observed for these mesas has no specific orientation with respect to the crystallographic axes of the semiconductor.

6.4 Micro-Raman Analysis of Drumhead Patterns in Square Mesas

In this section, micro-Raman spectroscopy results are presented which show evidence for a correlation between the drumhead patterns and strain induced in the GaAs cap layer by the wet thermal oxidation process. Section 6.4.1 contains a brief discussion of the methods used to obtain the micro-Raman data which is presented in Section 6.4.2. These results may be used to indicate the amount of strain induced in the crystal by the oxidation process. An explanation of the relationship between strain and the micro-Raman data is contained in Section 6.4.3. Finally, an interpretation of the micro-Raman results is discussed in Section 6.4.4.

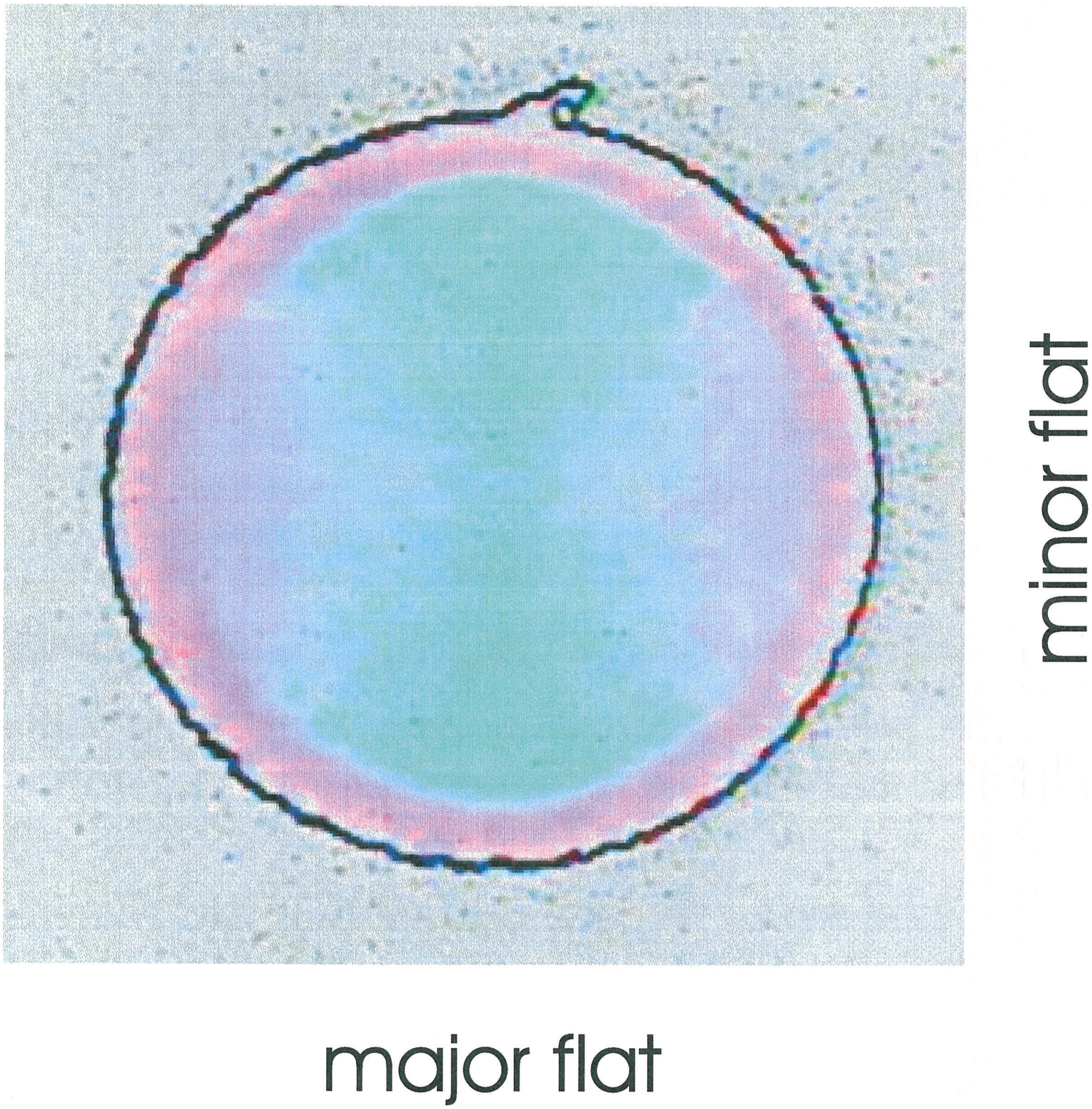

Figure 6.4: Optical microscope picture of a typical circular mesa, showing the drumhead pattern.

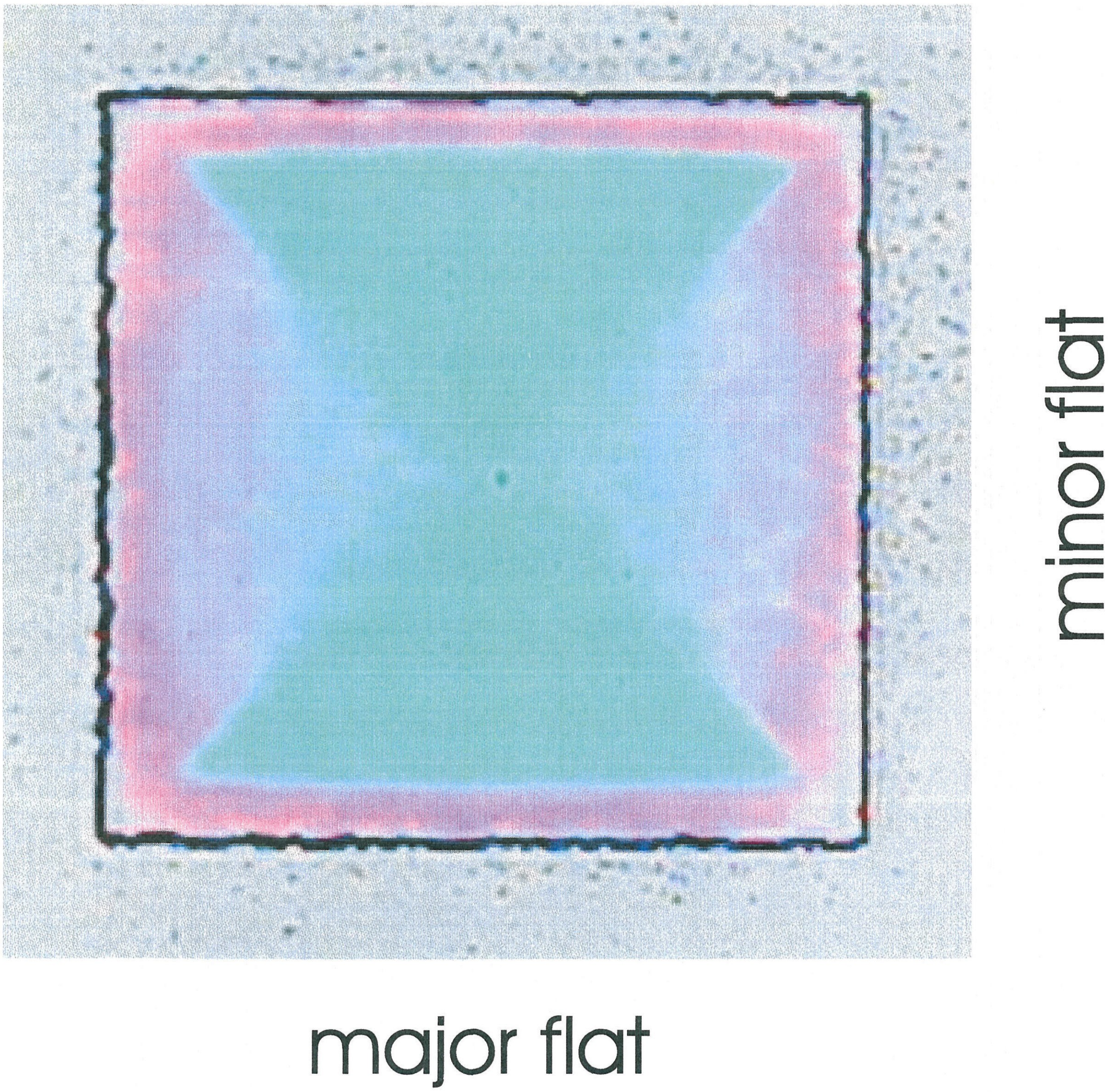

Figure 6.5: Optical microscope picture of a typical square mesa aligned with the {011} planes, showing the drumhead pattern.

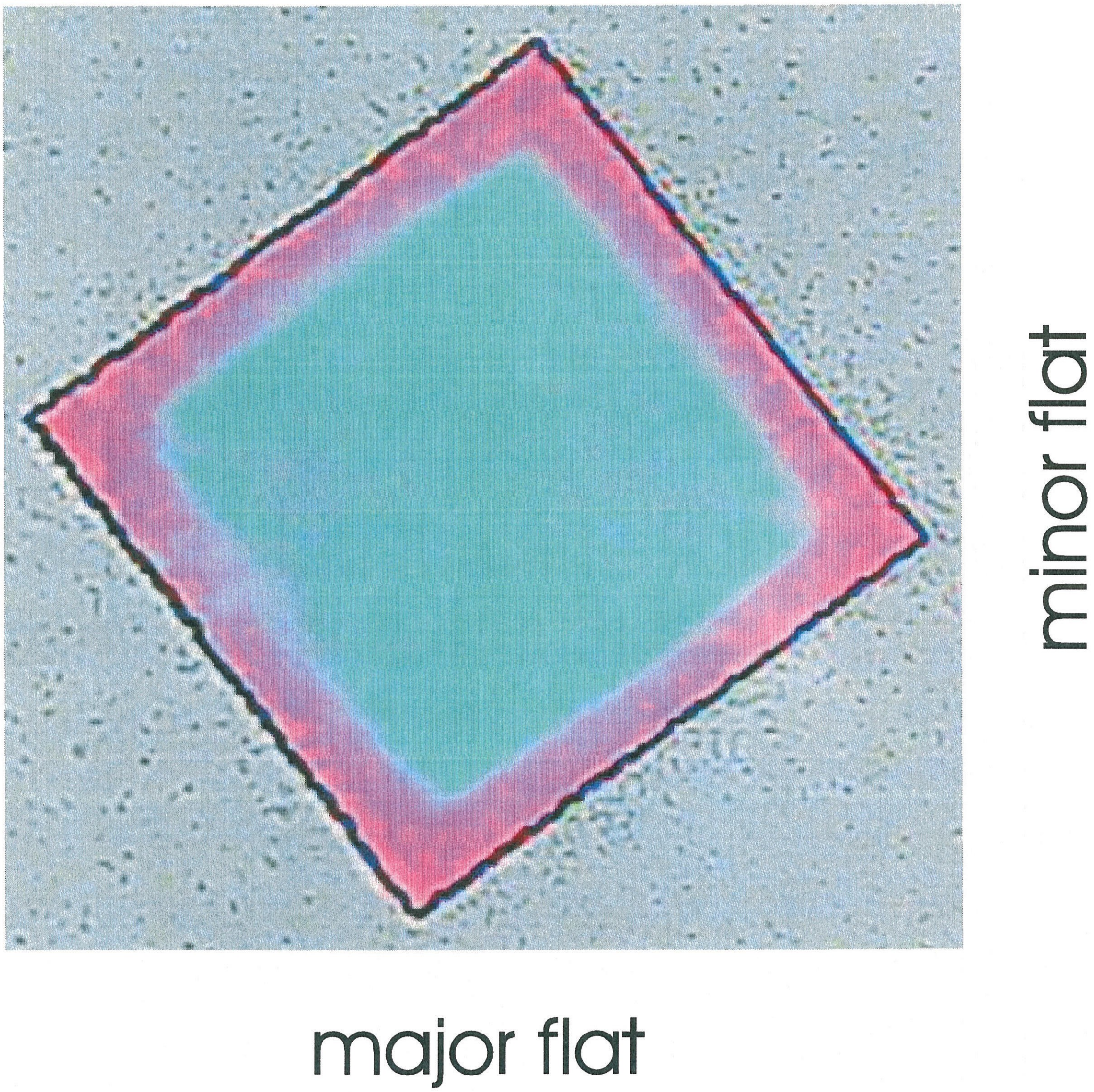

Figure 6.6: Optical microscope picture of a typical square mesa aligned with the $\{010\}$ planes, showing the drumhead pattern.

6.4.1 Micro-Raman Spectroscopy Data Collection

Micro-Raman spectra were collected by Namar Scientific, Inc., using excitation from an argon-ion laser at 514.5 nm with a maximum power of 2 mW, measured at the sample surface. Radiation scattered from the sample was collected in a 180° backscattering geometry and directed into a Renishaw System 1000 Raman spectrometer. Once inside the spectrometer, the radiation was filtered using a series of holographic notch filters and dispersed by a high-resolution grating (1800 grooves/mm) onto a thermo-electrically cooled CCD detector. The combined spectral resolution and reproducibility of the measurements was experimentally determined to be better than 3 cm^{-1} [1].

A Gaussian curve fit was used to precisely determine the location of the GaAs LO phonon. The form of the Gaussian profile was assumed to be

$$f(x) = Hexp\left[-\left(\frac{x - x_\circ}{w}\right)^2 (4ln(2))\right], \tag{6.1}$$

where $x_\circ$ is the position of the peak, H is the height of the peak, and w is its full-width half-maxiumum [1]. Using this technique, an uncertainty of approximately 0.03 cm^{-1} could be obtained for the position of the GaAs LO phonon peak. Landesman et al. used this technique in a micro-Raman study of the strain induced in the GaAs cap layer near the interface between oxidized and unoxidized AlAs and $\text{Al}_{0.98}\text{Ga}_{0.02}\text{As}$. In this case, a spectral resolution of 3.6 cm^{-1} was reported, and a Gaussian fit was used to obtain an uncertainty of 0.1 cm^{-1} in the shift of the GaAs LO phonon [2].

In the study reported by Landesman et al., a correction procedure was used to account for phonon shifts due to local heating. This procedure was especially important in comparing the phonon shift in oxidized and unoxidized regions since these areas exhibited different heating behavior, particularly for the $\text{Al}_{0.98}\text{Ga}_{0.02}\text{As}$ sample [2]. We have not employed this technique in our study and do not believe that our results are adversely affected as a consequence. Since our study was conducted on completely oxidized mesas, the effect of heating on the measurements should be the same for all data points.

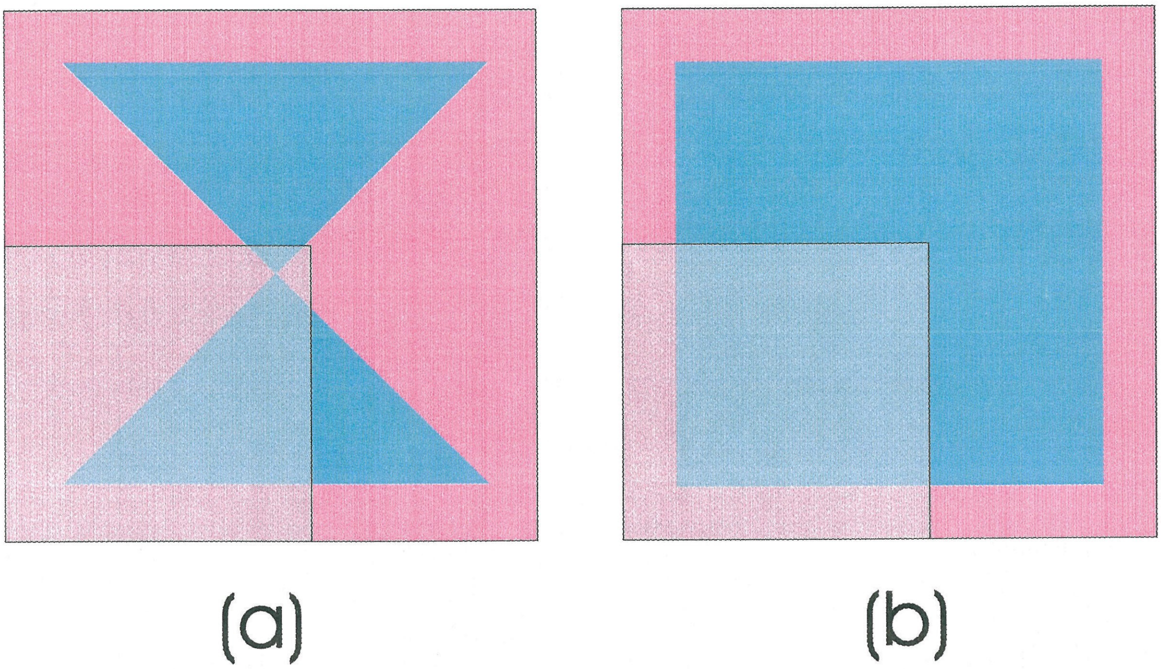

Figure 6.7: Illustration of the regions of square mesas mapped by micro-Raman measurements. (a) Mapped region on a square mesa aligned with the {011} planes. (b) Mapped region on a square mesa aligned with the {010} planes.

6.4.2 Raman Spectra Mapping of Completely Oxidized Square Mesas

Using the technique described in Section 6.4.1, micro-Raman spectra were obtained to map the position of the GaAs LO phonon across one-quarter of each of two completely oxidized square mesas. One of these mesas is from Sample A (sides aligned with the {011} planes) and the other is from Sample C (sides aligned with the {010} planes). The regions in which micro-Raman measurements were made are illustrated in Figure 6.7. The locations at which micro-Raman spectra were obtained from the mesa on Sample A are shown in Figure 6.8; those for the mesa on Sample C are shown in Figure 6.9.

The position of the GaAs LO phonon at each location on the mesa from Sample C is given in Table 6.1. It is clear that the pink area of the pattern corresponds to a lower value for the position of the GaAs LO phonon than does the green area. The average phonon position for locations C1 - C8 (pink area) is 291.70 ± 0.01 cm^{-1}, while the average for locations C9 - C17 (green area) is 292.17 ± 0.03 cm^{-1}. Note

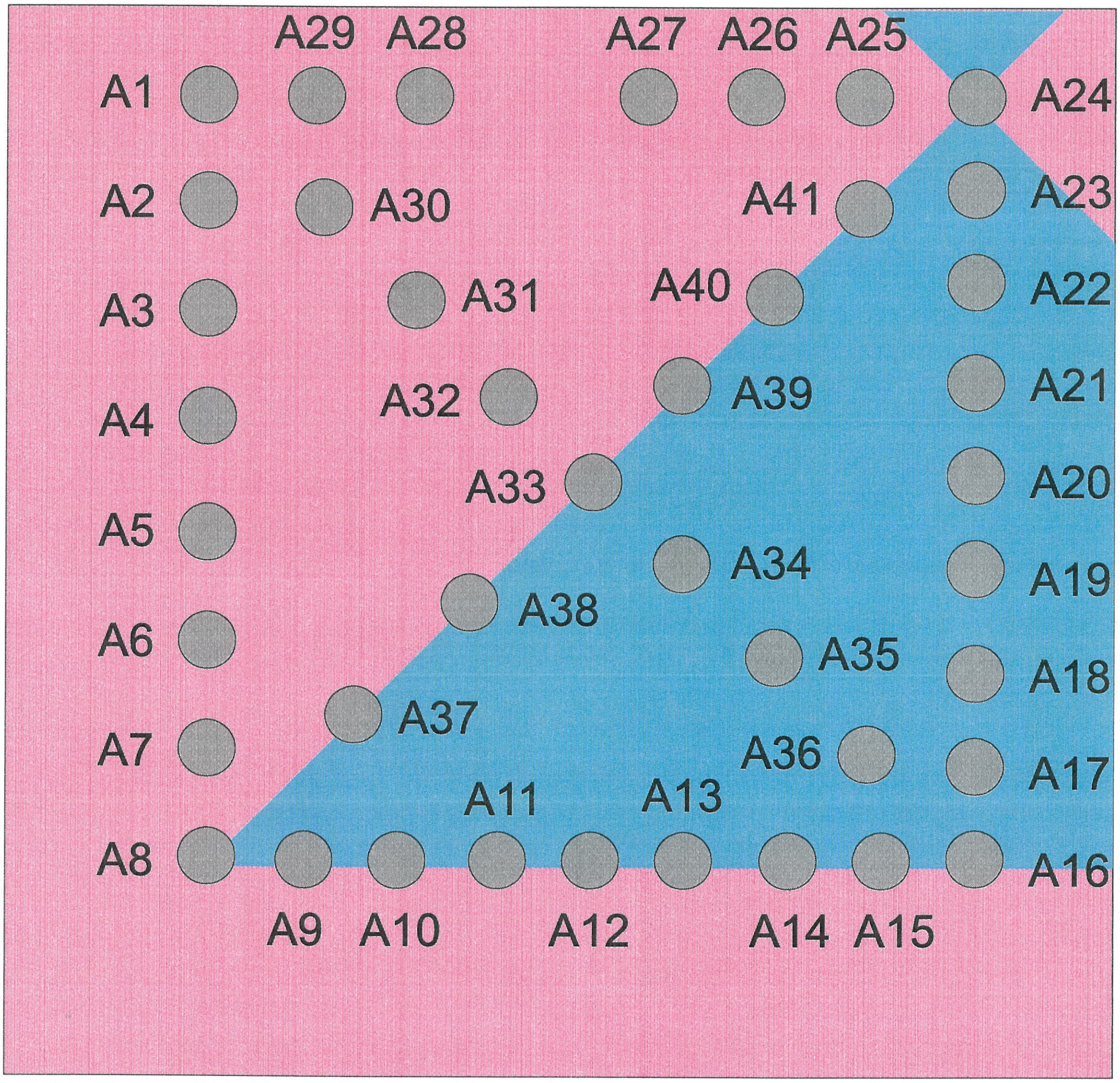

Figure 6.8: Diagram showing the locations of micro-Raman measurements on a square mesa aligned with the {011} planes (Sample A).

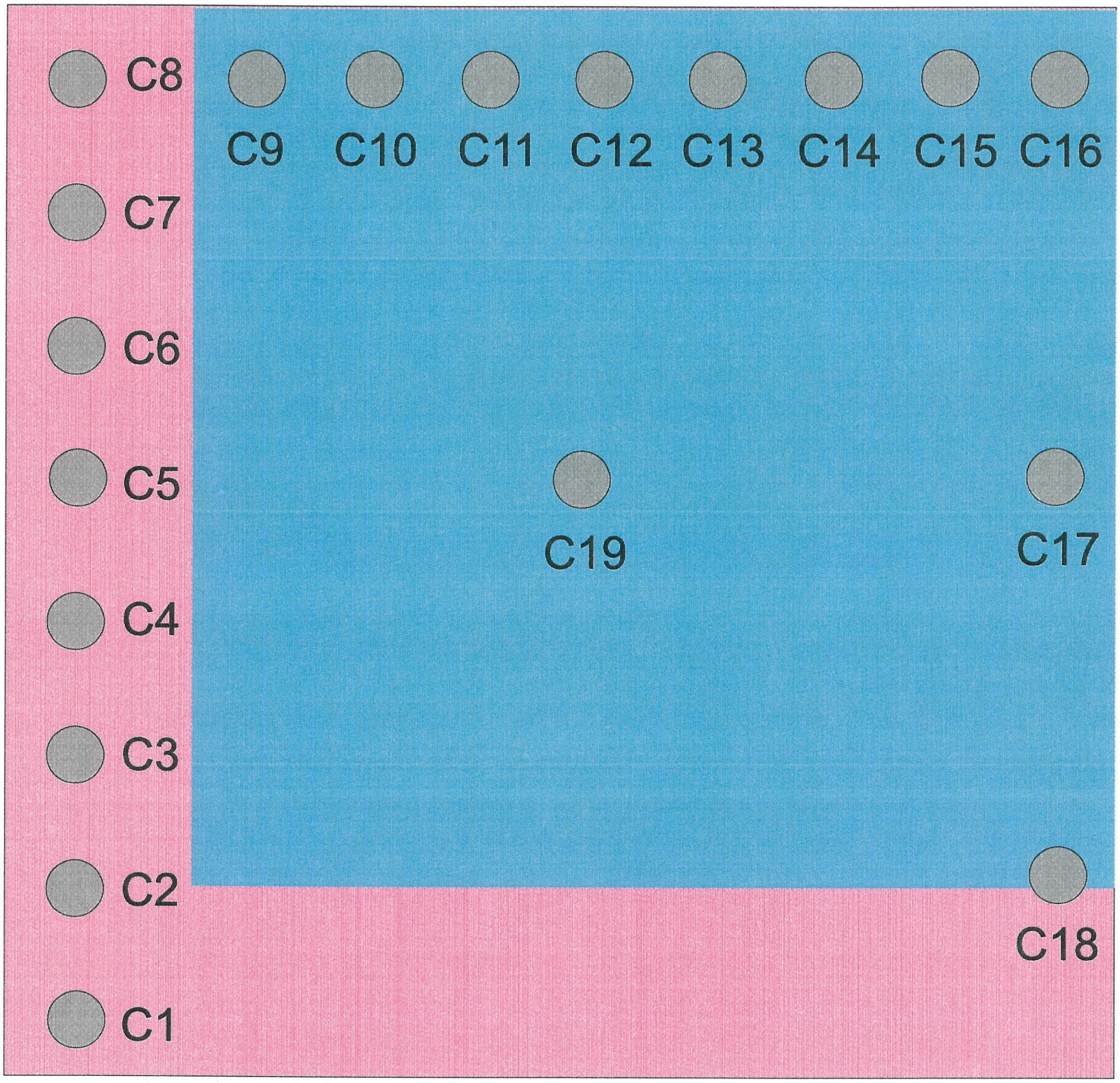

Figure 6.9: Diagram showing the locations of micro-Raman measurements on a square mesa aligned with the {010} planes (Sample C).

Table 6.1: GaAs LO phonon positions in a square mesa aligned with the {010} planes (Sample C).

measurement location	GaAs LO phonon position (cm^{-1})
C1	291.71 ± 0.03
C2	291.68 ± 0.03
C3	291.71 ± 0.03
C4	291.70 ± 0.03
C5	291.70 ± 0.03
C6	291.72 ± 0.03
C7	291.71 ± 0.03
C8	291.71 ± 0.03
C9	292.10 ± 0.03
C10	292.19 ± 0.03
C11	292.21 ± 0.03
C12	292.18 ± 0.03
C13	292.18 ± 0.03
C14	292.17 ± 0.03
C15	292.15 ± 0.03
C16	292.15 ± 0.03
C17	292.19 ± 0.03
C18	292.98 ± 0.03
C19	293.17 ± 0.03

that the latter average excludes C19, the measurement taken at the center of the green area. At 293.17 ± 0.03 cm^{-1}, the position of the GaAs LO phonon at this point is significantly higher than the positions measured at locations C9 - C17. The measurement at location C18 is also excluded from both averages, since it lies on the boundary between the green and pink areas.

Although the drumhead pattern for the mesa on Sample A is more complicated than that for the mesa on Sample C, similar results are obtained. The position of the GaAs LO phonon at each location on the mesa from Sample A is given in Table 6.2. Again, the position of the GaAs LO phonon in the pink region is generally observed at a lower wavenumber than in the green region. Measurements taken in the center of the sampled area have an average GaAs LO phonon position of 289.85 ± 0.06 cm^{-1} in the pink region (A30 - A32) and 290.00 ± 0.06 cm^{-1} in the green region (A34 - A36). Similarly, a comparison can be made between measured phonon positions along the [011] direction: 289.84 ± 0.05 cm^{-1} in the pink region (A2 - A7) and 290.16 ± 0.03 cm^{-1} in the green region (A17 - A23).

Table 6.2: GaAs LO phonon positions in a square mesa aligned with the {011} planes (Sample A).

measurement location	GaAs LO phonon position (cm^{-1})
A1	291.12 ± 0.03
A2	289.91 ± 0.03
A3	289.89 ± 0.03
A4	289.76 ± 0.04
A5	289.86 ± 0.03
A6	289.83 ± 0.03
A7	289.81 ± 0.03
A8	291.12 ± 0.03
A9	290.94 ± 0.03
A10	291.02 ± 0.03
A11	291.09 ± 0.03
A12	291.26 ± 0.03
A13	291.15 ± 0.03
A14	291.42 ± 0.03
A15	291.10 ± 0.03
A16	291.19 ± 0.03
A17	290.14 ± 0.03
A18	290.16 ± 0.03
A19	290.17 ± 0.03
A20	290.14 ± 0.03
A21	290.15 ± 0.04
A22	290.21 ± 0.03
A23	290.14 ± 0.03
A24	290.19 ± 0.03
A25	291.20 ± 0.03
A26	291.13 ± 0.03
A27	291.11 ± 0.03
A28	291.10 ± 0.03
A29	291.17 ± 0.03
A30	289.85 ± 0.03
A31	289.79 ± 0.03
A32	289.92 ± 0.03
A33	291.12 ± 0.03
A34	290.02 ± 0.03
A35	290.05 ± 0.03
A36	289.93 ± 0.03
A37	290.00 ± 0.03
A38	291.08 ± 0.03
A39	291.04 ± 0.03
A40	291.04 ± 0.03
A41	291.10 ± 0.03

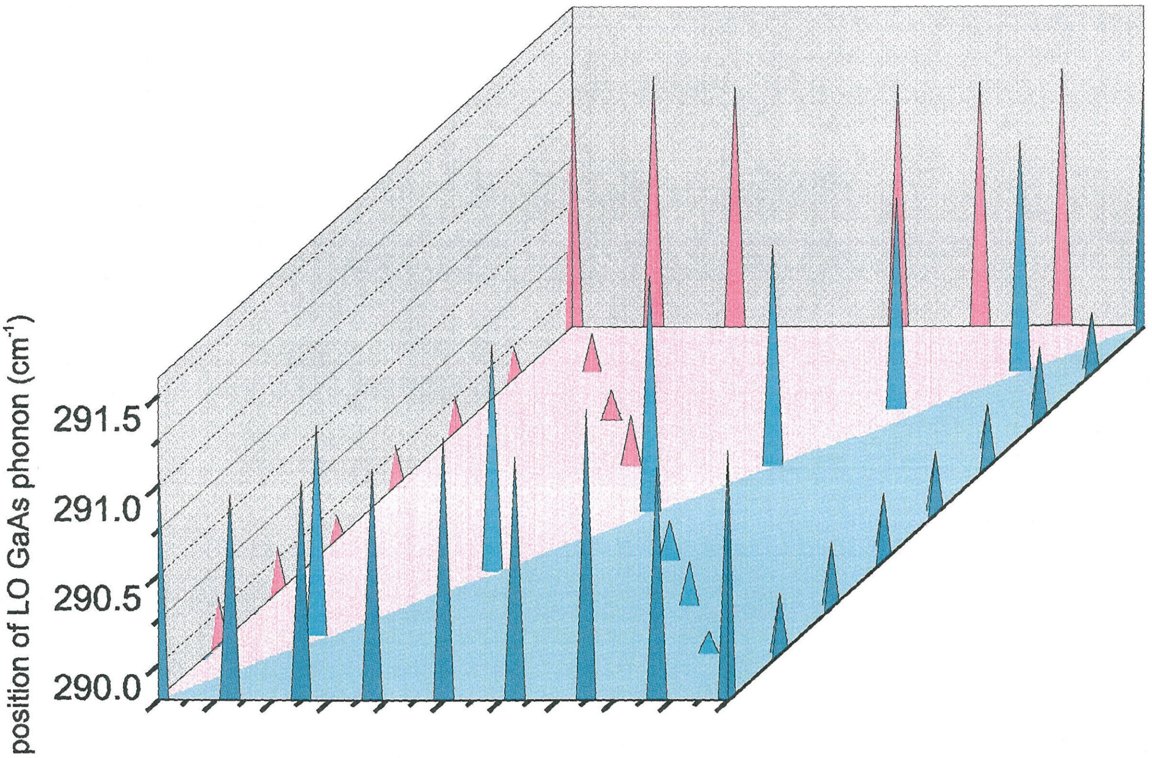

Figure 6.10: Three-dimensional representation of the micro-Raman measurements for a square mesa from Sample A. The x- and y-axes correspond to the spatial dimensions of the mesa, while the z-axis shows the position of the GaAs LO phonon at each spatial location. The pink and green coloring corresponds to the apparent color of the mesa at each location.

In order to obtain a more complete picture of the GaAs LO phonon position in the mesa, Figure 6.10 shows a three-dimensional representation of the micro-Raman data obtained for Sample A. The x- and y-axes correspond to the spatial dimensions of the mesa, while the z-axis shows the position of the GaAs LO phonon at each spatial location. Pink and green colors indicate the region of the mesa from which each measurement was taken. In addition to the observations above, it can be seen that the GaAs LO phonon is at a significantly higher position for measurements taken along the $[01\bar{1}]$ direction, as compared to those taken along the $[011]$ direction.

6.4.3 Relationship Between Micro-Raman Measurements and Strain

In this section, we consider the theoretical background for the relationship between strain and the micro-Raman measurements discussed in Section 6.4.2. In particular, we are interested in relating the positions of GaAs optical phonons to strain induced in the GaAs cap layer by the oxidation process. This strain is believed to be the result of the volume contraction observed as the underlying AlAs layer is converted to oxide (see Section 2.3.3). Because the measurements described in Section 6.4.2 were taken from the (100) face, observation of the TO modes is forbidden [2]. Therefore, we are only concerned with the GaAs LO phonon. In unstrained GaAs, the frequency of this mode is 291.8 cm^{-1} [3].

We start with the dynamical equation for the q $\approx$ 0 triply degenerate optical modes in a diamond-type crystal in the presence of a strain $\eta_{lm} = \eta_{ml}$ [4]:

$$\overline{m}\ddot{u}_i = -\sum_j k_{ij}u_j = -\left[k_{ii}^{(0)}u_i + \sum_{jlm}\frac{\partial k_{ij}}{\partial \eta_{lm}}\eta_{lm}u_j\right]. \tag{6.2}$$

In this equation, $\overline{m}$ is the reduced mass of the two atoms in the unit cell and u_i is the ith component of their relative displacements. In the absence of strain, the frequency of the modes is $\omega_\circ = \sqrt{\frac{k_{ii}^{(0)}}{\overline{m}}}$. Similarly, we can write $\omega_{ij} = \sqrt{\frac{k_{ij}}{\overline{m}}}$ so that Equation 6.2 becomes

$$\overline{m}\ddot{u}_i = -\overline{m}\left[\omega_\circ^2 u_i + \sum_{jlm}\frac{\partial \omega_{ij}^2}{\partial \eta_{lm}}\eta_{lm}u_j\right] = -\overline{m}\left[\omega_\circ^2 u_i + \sum_{jlm}\kappa_{ijlm}\eta_{lm}u_j\right], \tag{6.3}$$

where we have defined a phonon deformation potential [5]

$$\kappa_{ijlm} = \frac{\partial \omega_{ij}^2}{\partial \eta_{lm}}. \tag{6.4}$$

Writing the strained frequency as Ω, where

$$\overline{m}\ddot{u}_i = -\overline{m}\Omega^2 u_i, \tag{6.5}$$

Equation 6.3 can be written as an eigenvalue equation:

$$\sum_{jlm} \kappa_{ijlm} \eta_{lm} u_j - \left(\Omega^2 - \omega_\circ^2\right) u_i = 0. \tag{6.6}$$

With $\lambda = \Omega^2$ - $\omega_\circ^2$ and $\mathrm{P}_{ij} = \sum_{lm} \kappa_{ijlm}\eta_{lm}$, Equation 6.6 becomes

$$|P_{ij} - \lambda \delta_{ij}| = 0. \tag{6.7}$$

For a cubic crystal, there are only three independent components of the phonon deformation potential [4]:

$\mathrm{p} = \kappa_{1111} = \kappa_{2222} = \kappa_{3333}$

$\mathrm{q} = \kappa_{1122} = \kappa_{1133} = \kappa_{2211} = \kappa_{2233} = \kappa_{3311} = \kappa_{3322}$

$\mathrm{r} = \kappa_{1212} = \kappa_{1313} = \kappa_{2121} = \kappa_{2323} = \kappa_{3131} = \kappa_{3232}$

Assuming that the strain is uniform in the GaAs cap layer, we expect a biaxial stress [2, 6]:

$\sigma_{yy} = \sigma_{zz} = \mathrm{X}$

$\sigma_{xx} = \sigma_{xy} = \sigma_{yz} = \sigma_{zx} = 0$

Under this applied (100) coplanar stress, X, the non-zero components of the strain tensor can be written as [6]

$$\eta_{\parallel} = \eta_{yy} = \eta_{zz} = (S_{11} + S_{12})X \tag{6.8}$$

and

$$\eta_{\perp} = \eta_{xx} = 2S_{12}X, \tag{6.9}$$

where the S_{ij} are elastic compliance constants. Therefore, Equation 6.7 can be written as

$$\begin{vmatrix} p\eta_\perp + 2q\eta_\| - \lambda & 0 & 0 \\ 0 & p\eta_\| + q(\eta_\| + \eta_\perp) - \lambda & 0 \\ 0 & 0 & p\eta_\| + q(\eta_\| + \eta_\perp) - \lambda \end{vmatrix} = 0 \qquad (6.10)$$

for the strain induced in the GaAs cap layer by the volume contraction of an underlying oxide layer. The eigenvalues of Equation 6.10 are

$\lambda_{singlet} = \lambda_1 = \mathrm{p}\eta_\perp + 2\mathrm{q}\eta_\|$

$\lambda_{doublet} = \lambda_2 = \lambda_3 = \mathrm{p}\eta_\| + \mathrm{q}(\eta_\| + \eta_\perp)$

Raman selection rules dictate that the singlet mode will be detected [6]. Therefore, we can write the shift in the GaAs LO phonon, $\Delta\Omega = \Omega$ - ω_o, as

$$\Delta\Omega \approx \frac{\lambda}{2\omega_o} = \frac{p\eta_\perp + 2q\eta_\|}{2\omega_o}. \qquad (6.11)$$

With $\eta_\perp = \frac{2S_{12}}{S_{11}+S_{12}}\eta_\|$, Equation 6.11 becomes

$$\Delta\Omega \approx \frac{\eta_\|}{\omega_o}\left[\frac{pS_{12}}{S_{11}+S_{12}} + q\right]. \qquad (6.12)$$

Values for the GaAs elastic compliance constants and phonon deformation potentials have been experimentally determined. For GaAs at 300 K, the elastic compliance constants are $S_{11} = 1.170 \times 10^{-2}$ GPa^{-1} and $S_{12} = 3.64 \times 10^{-3}$ GPa^{-1} [6]. Landa et al. express the phonon deformation potentials in a slightly different form than that defined above. For the LO phonon, values of $\tilde{\kappa}_H$ = -6.6 and $\tilde{\kappa}_S$ = 0.70 are quoted [6], where

$$\tilde{\kappa}_H = \tilde{p} + 2\tilde{q} \qquad (6.13)$$

and

$$\tilde{\kappa}_S = \tilde{p} - \tilde{q}, \qquad (6.14)$$

and the dimensionless phonon deformation potential $\tilde{\kappa}$ is defined as [5]

$$\tilde{\kappa}_{ijlm} = \frac{\partial \ln \omega_{ij}^2}{\partial \eta_{lm}} = \frac{\kappa_{ijlm}}{\omega_o^2}. \qquad (6.15)$$

Therefore,

$$p = \frac{\omega_{\circ}^{2}}{3}\left(\tilde{\kappa}_H + 2\tilde{\kappa}_S\right) \tag{6.16}$$

and

$$q = \frac{\omega_{\circ}^{2}}{3}\left(\tilde{\kappa}_H - \tilde{\kappa}_S\right) \tag{6.17}$$

so that Equation 6.12 becomes

$$\Delta\Omega \approx -484cm^{-1}\eta_{||}. \tag{6.18}$$

For compressive strain, $\Delta\Omega > 0$; for tensile strain, $\Delta\Omega < 0$.

6.4.4 Strain in Completely Oxidized Square Mesas

As mentioned in Section 6.4.1, unequal heating in oxidized and unoxidized samples complicates a direct comparion between measurements before and after oxidation. Therefore, we are unable to make a definitive statement about the shift of the GaAs LO phonon in our samples due to oxidation. However, we can make a comparison between GaAs LO phonon positions in different areas of the drumhead pattern on a single oxidized mesa. In addition, by using the unstrained position of the GaAs LO phonon, we can obtain an estimate of the phonon shift produced by the oxidation. This allows us to obtain rough numbers for the strain induced in the GaAs cap at various locations on the mesa.

As shown in Section 6.4.2, there is a rough correspondence between the pink and green regions of the drumhead patterns and the position of the GaAs LO phonon measured in those regions. In general, the GaAs LO phonon is observed at a lower wavenumber in the pink regions, as compared to its position in the green regions. In addition to variations with the color of the region, measurements taken along the [011] direction seem to have lower phonon wavenumbers than those taken along the $[01\bar{1}]$ direction.

For simplicity, we obtain estimates of the strain induced in the GaAs cap by considering the phonon positions measured in Sample C. Assuming an unstrained

GaAs LO phonon position of 291.8 cm^{-1} [3], the average phonon shift in the pink region is -0.10 ± 0.01 cm^{-1}, while the average phonon shift in the green region is +0.37 ± 0.03 cm^{-1}. This corresponds to a tensile strain of 2.1 ± 0.2 x 10^{-4} in the pink region and a compressive strain of 7.6 ± 0.6 x 10^{-4} in the green region.

6.5 Dependence of Oxidation Rates on Crystallographic Direction

The study described in this section was conducted to explore our hypothesis that the observed orientation of the drumhead patterns is related to a crystallographic-dependence of the oxidation process itself. Section 6.5.1 describes the experimental procedure used in this study. Section 6.5.2 discusses the shapes of apertures observed for square and circular mesas. Numerical results for oxidation extent in different crystallographic directions are contained in Section 6.5.3. Finally, conclusions are presented in Section 6.5.4.

6.5.1 Modified Measurement Procedures

The samples used in this study were processed with mesas oriented as shown in Figure 6.2 and oxidized at 425°C for precisely 12 minutes under the conditions described in Chapter 3. Two optical microscope pictures were taken and measured for each mesa. The images were oriented 90° with respect to each other, in order to ensure that any distortion which might exist in the CCD image would not influence the measurements. This was especially important because of the modified procedure used to measure the apertures of circular and square mesas.

As discussed below, circular mesas in this study oxidized to form diamond-shaped apertures. Before measurement, each image was rotated such that the sides of the aperture were parallel to the x- and y-axes of the drawing program. The lengths and widths of the aperture and original mesa were then measured, as shown in Figure 6.11.

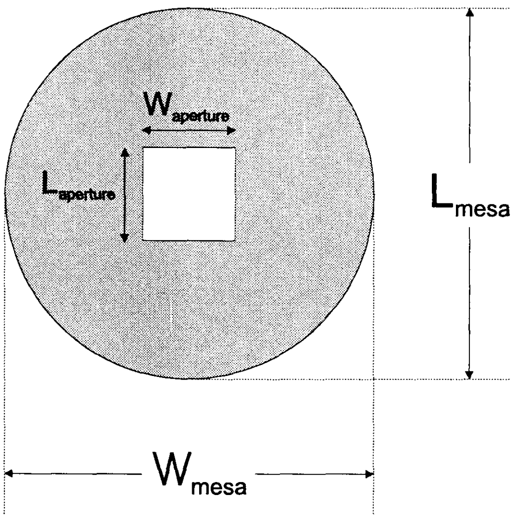

Figure 6.11: Measurements of aperture and mesa dimensions.

The extent of oxidation was obtained in each direction by the following formula:

$$x_D = 0.5(D_{mesa} - D_{aperture}), \tag{6.19}$$

where the D is either the length or the width dimension.

Similarly, the length and width of the approximately square apertures resulting from the oxidation of square mesas were also measured, along with the length and width of the original mesa. For Samples C and D, the images were rotated 45° before measurement. Again, Equation 6.19 was used to obtain the extent of oxidation in each direction.

6.5.2 Aperture Shape for Circular and Square Mesas

All of the circular mesas in this study oxidized to produce diamond-shaped apertures with sides aligned along the <010> crystal axes. Figure 6.12 shows a typical diamond-shaped aperture in a circular mesa. The consistency in the orientation of the apertures seems to indicate some crystallographic preference for the oxidation process. Although this observation supports our hypothesis, it is somewhat puzzling because the same result was not obtained in the study reported in Chapter 5, in which circular mesas produced circular apertures. The samples in both studies were processed and oxidized using the same procedures; however, different wafers were used as the source material in the two studies, which may account for the different shape of the apertures.

The observation of diamond- or square-shaped apertures is supported by several reports by other researchers [7, 8, 9, 10], as is the conclusion that this shape indicates some crystallographic dependence for the oxidation process [7, 11, 12]. Choquette et al. report that the diamond-shaped apertures have sides aligned along the <010> crystal axes [11, 12] and attribute this to slightly faster oxidation along the <010> crystal axes, as compared to that along the <011> axes [11, 12].

Despite the difference in drumhead patterns observed for squares aligned with the $\{011\}$ planes versus those aligned with the $\{010\}$ planes, no difference was observed in the shape of the apertures. Square mesas on all four samples produced square apertures with rounded corners and sides aligned with those of the original mesa.

6.5.3 Oxidation Extent as a Function of Crystallographic Orientation

The remainder of this study involves an investigation of the relative oxidation rates in different crystallographic directions. The partially oxidized stripes on Samples A - D provide the most straightforward comparison of the oxidation rates. Table 6.3 shows the extent of oxide formed in the stripes on each of the four samples. It can be concluded from this data that oxidation along the [011] direction is slightly faster than along the $[01\bar{1}]$ direction. Within the experimental uncertainty, there is no difference in the oxidation rates observed along the <010> directions and between the rates along these directions and the [011] direction. Therefore, only the $[01\bar{1}]$ direction is observed to have a reduced oxidation rate.

The results obtained for circular mesas show that the oxidized apertures are quite symmetric. For a given sample, the aperture dimensions and oxidation extent in the [001] and [010] directions are identical within the experimental uncertainty, as shown in Tables 6.4 and 6.5. In addition, there is very little difference in the oxidation

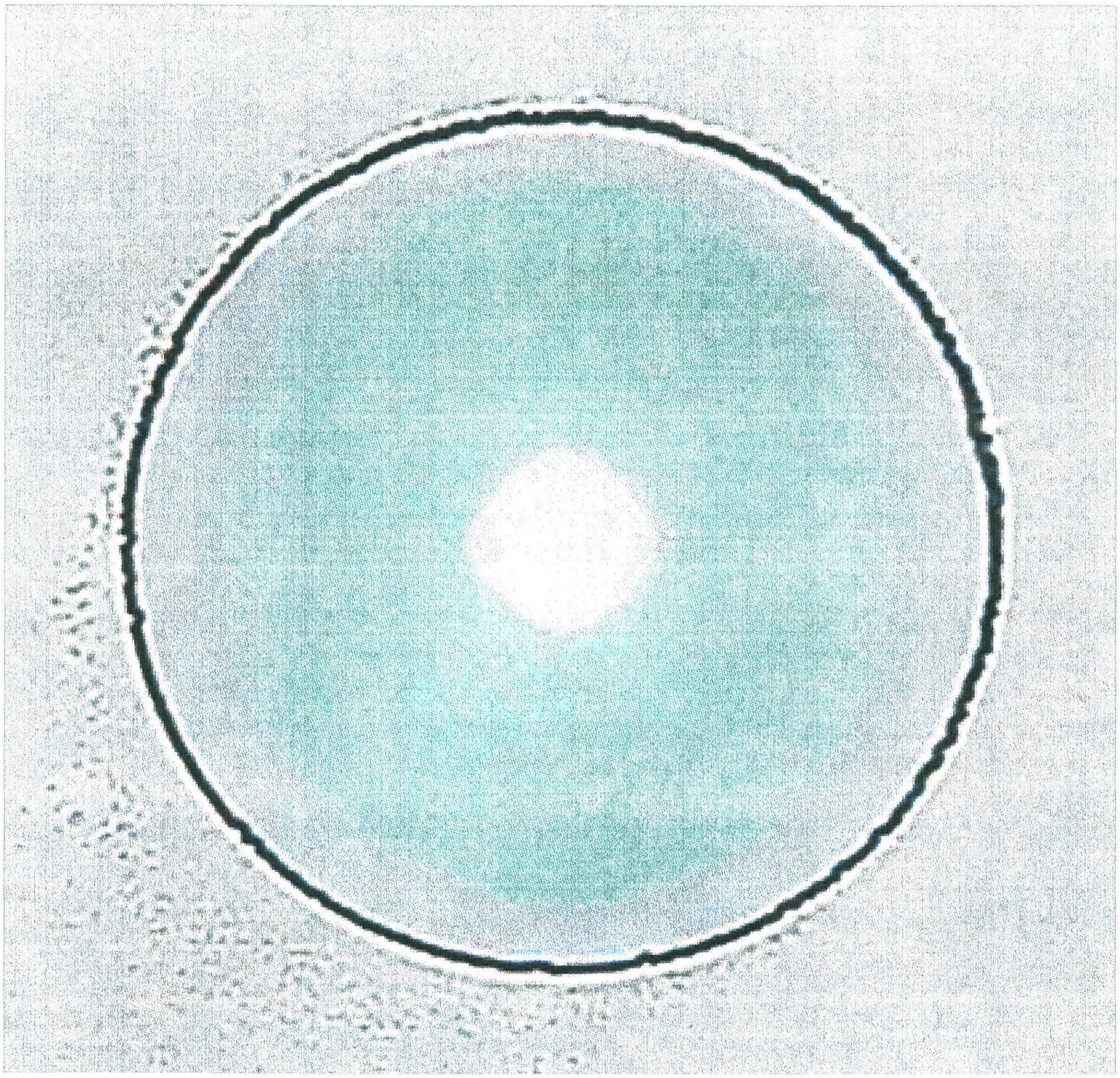

Figure 6.12: Optical microscope picture of a typical circular mesa with a diamond-shaped aperture.

Table 6.3: Extent of oxide formed in stripes after 12-minute wet thermal oxidation at 425°C.

sample	direction of oxidation	oxide extent
A	[011]	$50.7 \pm 0.4\ \mu$m
B	$[01\bar{1}]$	$47 \pm 2\ \mu$m
C	[001]	$50 \pm 1\ \mu$m
D	[010]	$51 \pm 2\ \mu$m

Table 6.4: Dimensions of aperture formed in 150 μm-diameter circular mesas after 12-minute wet thermal oxidation at 425°C.

sample	dimension parallel to [010] direction	dimension parallel to [001] direction
A	30 ± 2 μm	30 ± 2 μm
B	35 ± 5 μm	35 ± 5 μm
C	39 ± 5 μm	39 ± 6 μm
D	38 ± 8 μm	39 ± 8 μm

Table 6.5: Extent of oxide formed in 150 μm-diameter circular mesas after 12-minute wet thermal oxidation at 425°C.

sample	oxide extent in [010] direction	oxide extent in [001] direction
A	65.9 ± 0.5 μm	66.1 ± 0.7 μm
B	64 ± 2 μm	64 ± 2 μm
C	62 ± 2 μm	62 ± 3 μm
D	62 ± 4 μm	62 ± 4 μm

extents measured for the four samples. Therefore, the variation in aperture size from one sample to the next can be attributed to differences in the size of the original mesas. Such a difference could arise as part of the processing of the samples, particularly in developing the photoresist pattern used for etching.

As compared to the circular mesas, there is less variation between the dimensions of the apertures in square mesas on different samples, as shown in Table 6.6. The slightly smaller dimensions measured for Sample A seem to also be a result of smaller original mesas, since all four samples exhibit similar oxidation extents, as shown in Table 6.7. Results from Samples C and D indicate that oxidation along the [010] and [001] directions is virtually identical. Although the results from Sample B show identical oxidation in the [011] and $[01\bar{1}]$ directions, those from Sample A indicate a slight difference between these two directions. In agreement with the results obtained for stripes, oxidation in the [011] direction appears to proceed slightly faster than in the $[01\bar{1}]$ direction.

Table 6.6: Dimensions of aperture formed in 150 μm x 150 μm square mesas after 12-minute wet thermal oxidation at 425°C.

sample	dimension parallel to [011] direction	dimension parallel to $[01\bar{1}]$ direction
A	50 ± 2 μm	52 ± 2 μm
B	54 ± 5 μm	55 ± 6 μm
sample	dimension parallel to [010] direction	dimension parallel to [001] direction
C	55 ± 4 μm	55 ± 4 μm
D	54 ± 8 μm	54 ± 8 μm

Table 6.7: Extent of oxide formed in 150 μm x 150 μm square mesas after 12-minute wet thermal oxidation at 425°C.

sample	oxide extent in [011] direction	oxide extent in $[01\bar{1}]$ direction
A	56.0 ± 0.9 μm	54.4 ± 0.8 μm
B	54 ± 2 μm	54 ± 3 μm
sample	oxide extent in [010] direction	oxide extent in [001] direction
C	54 ± 2 μm	54 ± 2 μm
D	54 ± 4 μm	54 ± 4 μm

6.5.4 Conclusions

As demonstrated in Section 6.5.3, our data shows a slight reduction in oxidation rate for the $[01\bar{1}]$ direction, as compared to the [011] and <010> directions. Within the experimental uncertainty of our measurements, there is no difference in oxidation rates for the [011] and <010> directions. Based on the shape and orientation of the apertures in circular mesas, Choquette et al. predict a slightly faster oxidation along the <010> crystal axes, as compared to that along the <011> axes [11, 12]. Although our data supports a faster oxidation in the <010> directions than in the $[01\bar{1}]$ direction, the results obtained in this study do not follow the more generalized prediction of slower oxidation in the <011> directions. However, Li et al. predict a different oxidation profile along the [011] and $[01\bar{1}]$ directions because of the excellent polarization selection and control observed in oxide-confined VCSELs [8]. Our results support both this prediction and, as will be discussed in Section 6.6, the observations and measurements reported earlier in this chapter.

6.6 Conclusions

In the previous sections of this chapter, observations and measurements from several studies have been presented. This section attempts to bring these results together to form a conclusion about strain induced in two-dimensional mesas due to the wet thermal oxidation process. The results which will be synthesized to form the conclusion are as follows:

1. Drumhead patterns are observed in circular and square mesas which have been oxidized almost to completion. For circular mesas and square mesas aligned with the {011} planes, the drumhead pattern is consistently oriented parallel to the [011] direction. The drumhead pattern for square mesas aligned with the {010} planes has no clear directional preference.
2. Micro-Raman measurements show some correspondence between the drumhead patterns and strain in the mesas.
3. Apertures in circular mesas have a diamond shape, with sides aligned along the <010> directions.
4. Oxidation proceeds slightly slower in the $[01\bar{1}]$ direction, as compared to the [011] and <010> directions.

The results for circular mesas – diamond-shaped apertures and drumhead patterns with a specific crystallographic orientation – can be understood by consideration of the crystallographic-dependence of the oxidation. If the oxidation proceeded at equal rates in all directions, we would expect the oxidation of circular mesas to produce circular apertures. However, a crystallographic-dependence will force the aperture to have a specific orientation with respect to the direction with the anomalous oxidation rate. As shown in Figure 6.13, orienting a diamond-shaped aperture along the <010> directions allows for a slower oxidation rate in the $[01\bar{1}]$ direction. Likewise, if the oxidation rate had no variation with respect to crystallographic orientation, we would not expect the drumhead pattern to have a specific crystallographic orientation.

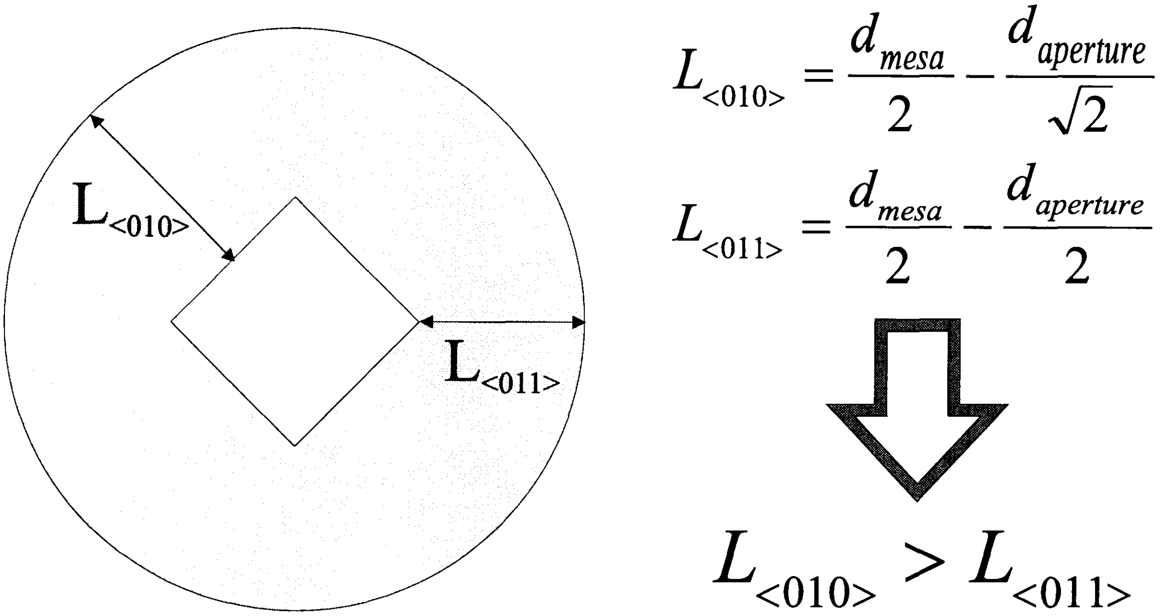

$$L_{<010>} = \frac{d_{mesa}}{2} - \frac{d_{aperture}}{\sqrt{2}}$$

$$L_{<011>} = \frac{d_{mesa}}{2} - \frac{d_{aperture}}{2}$$

$$L_{<010>} > L_{<011>}$$

Figure 6.13: This figure illustrates oxide extents in the <010> and <011> directions required to form a diamond aperture of length and width $d_{aperture}$ in a circular mesa of diameter d_{mesa}.

However, because the $[01\bar{1}]$ direction has a different oxidation rate, this deviation insures that the drumhead pattern will have a specific orientation with respect to this direction.

Without any crystallographic preference for oxidation in directions perpendicular to the four sides of a square mesa, we would expect the drumhead patterns to have no crystallographic preference either. This is in fact the case for Samples C and D. Since the sides of the squares on these samples are oriented along the <010> directions, which have equal oxidation rates, the symmetry of the original mesa is preserved. However, for the squares on Samples A and B, the symmetry is broken by the reduced oxidation rate in the $[01\bar{1}]$ direction. Again, this deviation insures that the drumhead pattern has a specific orientation with respect to the $[01\bar{1}]$ direction.

The volume contraction of the AlAs layer upon oxidation is well known and is discussed in Section 2.3.1. This effect is believed to be responsible for strain induced in the surrounding semiconductor crystal by the oxidation process. As demonstrated by Landesman et al., the oxidation process induces local strain in the GaAs cap layer at the oxide-AlAs interface [2]. Because of the reduced oxidation rate in the $[01\bar{1}]$

direction, the volume contraction of the oxide will not be symmetric with respect to the center of the mesa. This effect should be greatest as the oxidation nears completion and may explain the drumhead patterns observed in mesas which are almost completely oxidized. However, the exact mechanisms involved in the formation of the drumhead patterns are not completely understood at the present time.

Bibliography

[1] F. Hardcastle, Technical Report No. 98-11005, Namar Scientific, Inc. (unpublished).

[2] J. Landesman, A. Fiore, J. Nagle, V. Berger, E. Rosencher, and P. Puech, Appl. Phys. Lett. **71**, 2520 (1997).

[3] A. Sood, E. Anastassakis, and M. Cardona, Phys. Status Solidi B **129**, 505 (1985).

[4] E. Anastassakis, A. Pinczuk, E. Burstein, F. Pollack, and M. Cardona, Solid State Commun. **8**, 133 (1970).

[5] A. Papadopoulos, Y. Raptis, and E. Anastassakis, Solid State Commun. **58**, 645 (1986).

[6] G. Landa, R. Carles, C. Fontaine, E. Bedel, and A. Muñoz-Yagüe, J. Appl. Phys. **66**, 196 (1989).

[7] D. Huffaker, D. Deppe, and K. Kumar, Appl. Phys. Lett. **65**, 97 (1994).

[8] G. Li, S. Lim, W. Yuen, and C. Chang-Hasnain, Electron. Lett. **31**, 2014 (1995).

[9] P. Floyd, B. Thibeault, L. Coldren, and J. Merz, Electron. Lett. **32**, 114 (1996).

[10] H.-E. Shin, Y.-G. Ju, J.-H. Shin, J.-H. Ser, T. Kim, E.-K. Kee, I. Kim, and Y.-H. Lee, Electron. Lett. **32**, 1287 (1996).

[11] K. Choquette, K. Geib, H. Chui, B. Hammons, H. Hou, T. Drummond, and R. Hull, Appl. Phys. Lett. **69**, 1385 (1996).

[12] K. Choquette, K. Geib, C. Ashby, R. Twesten, O. Blum, H. Hou, D. Follstaedt, B. Hammons, D. Mathes, and R. Hull, IEEE J. Select. Topics Quantum Electron. **3**, 916 (1997).

Appendix A Mathematica Programs

A.1 Mathematica Code to Calculate Weighted Averages

```
n = number of data points to be averaged;
Array[value,n];
Array[error,n];

value[1] = first data point;
error[1] = uncertainty in first data point;

⋮

value[n] = last data point;
error[n] = uncertainty in last data point;

denominator = 0;
sum = 0;
i = 1;
While [i < n+1, Do[
   denominator = denominator + (1/(error[i]^2));
   sum = sum + (value[i]/(error[i]^2));
   i = i + 1]];
mean = sum/denominator
sigma = Sqrt[1/denominator]
```

A.2 Mathematica Code to Calculate $t_{diffusion}$ for the Oxidation of Circular Mesas

```
n  = number of experimental oxidation length data points;
Array[ox,n];
ox[1] = first experimental oxidation length;

⋮

ox[n] = last experimental oxidation length;
a = average radius of mesas on the sample;
c = 0.5;
```

This section calculates the zeroes of the J_0 Bessel function.

```
m = 1000;
Array[k,m];
start = 0;
i= 1;
While [i < (m+1), Do[
   list = FindRoot[BesselJ[0,x] == 0, {x, start + Pi}];
   k[i] = x /.list;
   start = k[i];
   i = i+1]]

d = diffusion constant;
```

```
j = 1;
While[j < (n+1), Do[
   x = ox[j];
   list = FindRoot[1 - (2/a)*
             Sum[(Exp[-d*((k[i]/a)^2)*t]*
             BesselJ[0, (1 - (x/a))*k[i]])/((k[i]/a)*
             BesselJ[1, k[i]]), {i, 1, m}] == c, {t,(x^2)/d}];
   t = t /.list;
   Print[t];
   j = j + 1]]
```

A.3 Mathematica Code to Calculate Uncertainty in Fitted Values of D and k_R for Circular Mesas

```
n = number of experimental oxidation length data points;
Array[time,n];
Array[oxide,n];
Array[td,n];
Array[tr,n];
Array[d,3];
Array[r,3];
Array[chi,3];
```

This section calculates the zeroes of the J_0 *Bessel function.*

```
m = 1000;
Array[k,m];
start = 0;
i= 1;
While [i < (m+1), Do[
   list = FindRoot[BesselJ[0,x] == 0, {x, start + Pi}];
   k[i] = x /.list;
   start = k[i];
   i = i+1]]

oxide[1] = first experimental oxidation length;

⋮

oxide[n] = last experimental oxidation length;
```

```
time[1] = oxidation time for first experimental oxidation length;

⋮

time[n] = oxidation time last experimental oxidation length;
a = average radius of mesas on the sample
c = 0.5;

reaction = calculated value of $k_R$;
i = 1;
While[i < (n+1), Do[
  tr[i] = (2*a*oxide[i] - (oxide[i]^2))/reaction;
  i = i + 1]]

delta = 5;
diffusion = calculated value of D - (delta*1.5);
i = 1;
While[i < 4, Do[
   d[i] = diffusion;
   diffusion = d[i] + delta;
   i = i+1]]

l = 1;
While[l < 4, Do[
   j = 1;
   While[j < (n+1), Do[
      x = oxide[j];
      list = FindRoot[1 - (2/a)*Sum[(Exp[-d[l]*((k[i]/a)^2)*t]*
                BesselJ[0, (1 - (x/a))*k[i]])/((k[i]/a)*
                BesselJ[1, k[i]]), {i, 1, m}] == c, {t,(x^2)/d[l]}];
      td[j] = t /.list;
      j = j + 1]]
```

```
   chi[l] = 0;
   j = 1;
   While[j < (n+1), Do[
      chi[l] = chi[l] + ((time[j] - (td[j] + tr[j]))^2);
      j = j+1]]
   l = l+1]]
```

This section returns the diffusion constant D and
its uncertainty.

```
denom = chi[1] - (2*chi[2]) + chi[3];
diffusion = d[3] - delta*(((chi[3] - chi[2])/denom)+0.5)
sigma = delta*Sqrt[2/denom]
```

diffusion = *calculated value of D*;

```
j = 1;
While[j < (n+1), Do[
   x = oxide[j];
   list = FindRoot[1 -(2/a)*Sum[(Exp[-diffusion*((k[i]/a)^2)*t]*
             BesselJ[0, (1 - (x/a))*k[i]])/((k[i]/a)*
             BesselJ[1, k[i]]), {i, 1, n}]== c, {t,(x^2)/diffusion}];
   td[j] = t /.list;
   j = j + 1]]

delta = 20;
```

reaction = *calculated value of* k_R - (delta*1.5);

```
i = 1;
While[i < 4, Do[
   r[i] = reaction;
   reaction = r[i] + delta;
   i = i+1]]
```

```
l = 1;
While[l < 4, Do[
   j = 1;
   While[j < (n+1), Do[
      tr[j] = (2*a*oxide[j] - (oxide[j]^2))/r[l];
      j = j+1]]
   chi[l] = 0;
   j = 1;
   While[j < (n+1), Do[
      chi[l] = chi[l] + ((time[j] - (td[j] + tr[j]))^2);
      j = j+1]]
   l = l+1]]
```

This section returns the reaction constant k_R
and its uncertainty.

```
denom = chi[1] - (2*chi[2]) + chi[3];
reaction = r[3] - delta*(((chi[3] - chi[2])/denom)+0.5)
sigma = delta*Sqrt[2/denom]
```

A.4 Mathematica Code to Calculate $t_{reaction}$ for the Oxidation of Square Mesas

```
c[a_] := 0.55202 + 0.52647*Tanh[(a/16.90952) - 2.90555]
q[a_,theta_] := c[a]*(Cos[theta]^2)*(Sin[theta]^2)
r[a_,theta_] := a*Sqrt[(0.5/q[a,theta])*
                    (1 + Sqrt[1 - (4*q[a,theta])])]


n = number of experimental oxidation length data points;
Array[ox,n];
Array[x,n];
ox[1] = first experimental oxidation length;

⋮

ox[n] = last experimental oxidation length;
ao = one-half the average length of sides of mesas on the sample;

j = 1;
While[j < (n+1), Do[
   x[j] = ao - ox[j];
   l = Re[NIntegrate[Integrate[r[a,theta],
          {theta, 0, (2*Pi)}], {a, x[j], ao}]]
   Print[l];
   j = j + 1]]
```

A.5 Mathematica Code to Calculate $t_{diffusion}$ for the Oxidation of Square Mesas

```
n = number of experimental oxidation length data points;
Array[ox,n];
ox[1] = first experimental oxidation length;

⋮

ox[n] = last experimental oxidation length;
a = one-half the average length of sides of mesas on the sample;
c = 0.5;

oddl := (2*l) + 1;
oddm := (2*m) + 1;
alpha := oddl*Pi/(2*a);
beta := oddm*Pi/(2*a);
f[d_,x_,y_]:= 1 - (16/(Pi^2))* Sum[(((-1)^(l+m))/(oddl*oddm))*
        Cos[alpha*x]*Cos[beta*y]* Exp[-d*t*((alpha^2)+(beta^2))],
        {l, 0, sumtotal}, {m, 0, sumtotal}]
x:= a - L;

d = diffusion constant;
sumtotal = 10;
y = 0;
start = 0.1;
j = 1;
```

```
While[j < (n+1), Do[

   L = ox[j]

   list = FindRoot[f[d,x,y] == c, {t,start}];

   t = t /.list;

   Print[t];

   start = t;

   j = j + 1]]
```

A.6 Mathematica Code to Calculate Uncertainty in Fitted Values of D and k_R for Square Mesas

```
n = number of experimental oxidation length data points;

Array[time,n];

Array[oxide,n];

Array[td,n];

Array[tr,n];

Array[ro,n];

Array[d,3];

Array[r,3];

Array[chi,3];

oddl := (2*l) + 1;

oddm := (2*m) + 1;

alpha := oddl*Pi/(2*a);

beta := oddm*Pi/(2*a);

f[d_,x_,y_]:= 1 - (16/(Pi^2))* Sum[(((-1)^(l+m))/(oddl*oddm))*

       Cos[alpha*x]*Cos[beta*y]* Exp[-d*t*((alpha^2)+(beta^2))],

       {l, 0, sumtotal}, {m, 0, sumtotal}]

x:= a - L;

oxide[1] = first experimental oxidation length;

⋮

oxide[n] = last experimental oxidation length;

ro[1] = value of function l(x_o) for first experimental

           oxidation length(calculated in Appendix A.4);

⋮

ro[n] = value of function l(x_o) for last experimental

           oxidation length (calculated in Appendix A.4);
```

```
time[1] = oxidation time for first experimental oxidation length;

⋮

time[n] = oxidation time last experimental oxidation length;
a = one-half the average length of sides of mesas on the sample;
c = 0.5;

reaction = calculated value of $k_R$;
i = 1;
While[i < (n+1), Do[
  tr[i] = ro[i]/(8*a*reaction);
  i = i + 1]]

delta = 5;
diffusion = calculated value of D - (delta*1.5);
i = 1;
While[i < 4, Do[
   d[i] = diffusion;
   diffusion = d[i] + delta;
   i = i+1]]

sumtotal = 10;
y = 0;
start = 0.1;
i = 1;
```

```
While[i < 4, Do[
   j = 1;
   While[j < (n+1), Do[
      L = oxide[j];
      list = FindRoot[f[d[i],x,y] == c, {t,start}];
      td[j] = t /.list;
      j = j + 1]]
   chi[i] = 0;
   j = 1;
   While[j < (n+1), Do[
      chi[i] = chi[i] + ((time[j] - (td[j] + tr[j]))^2);
      j = j+1]]
   i = i+1]]
```

This section returns the diffusion constant D and
its uncertainty.

```
denom = chi[1] - (2*chi[2]) + chi[3];
diffusion = d[3] - delta*(((chi[3] - chi[2])/denom)+0.5)
sigma = delta*Sqrt[2/denom]
```

`diffusion =` *calculated value of D*;

```
sumtotal = 10;
y = 0;
start = 0.1;
j = 1;
While[j < (n+1), Do[
   L = oxide[j];
   list = FindRoot[f[diffusion,x,y] == c, {t,start}];
   td[j] = t /.list;
   start = td[j];
   j = j + 1]]
```

```
delta = 20;
reaction = calculated value of k_R - (delta*1.5);
i = 1;
While[i < 4, Do[
   r[i] = reaction;
   reaction = r[i] + delta;
   i = i+1]]


i = 1;
While[i < 4, Do[
   j = 1;
   While[j < (n+1), Do[
      tr[j] = ro[j]/(8*a*r[i]);
      j = j+1]]
   chi[i] = 0;
   j = 1;
   While[j < (n+1), Do[
      chi[i] = chi[i] + ((time[j] - (td[j] + tr[j]))^2);
      j = j+1]]
   i = i+1]]
```

This section returns the reaction constant k_R
and its uncertainty.

```
denom = chi[1] - (2*chi[2]) + chi[3];
reaction = r[3] - delta*(((chi[3] - chi[2])/denom)+0.5)
sigma = delta*Sqrt[2/denom]
```